Università degli Studi di Napoli Federico II
Ph.D. Program in
Product and Industrial Processes Engineering
XXXV Cycle

Dissertation for the Degree of Doctor of Philosophy

Foam-enhanced polymer devolatilization

From single bubble analysis to high-efficiency devolatilizer

by
Lorenzo Lombardi

Advisor: Prof. Pier Luca Maffettone

Co-advisor: Prof. Daniele Tammaro

Scuola Politecnica e delle Scienze di Base
Dipartimento di Ingegneria Chimica, dei Materiali e della Produzione Industriale

Foam-enhanced polymer devolatilization

From single bubble analysis to high-efficiency devolatilizer

Ph.D. Dissertation presented
for the fulfillment of the Degree of Doctor of Philosophy
in Product and Industrial Processes Engineering
by

Lorenzo Lombardi

February 2023

Approved as to style and content by

_____

Prof. Pier Luca Maffettone, Advisor

_____

Prof. Daniele Tammaro, Co-advisor

Università degli Studi di Napoli Federico II
Ph.D. Program in Product and Industrial Processes Engineering
XXXV cycle - Chairman: Prof. Andrea D'Anna

Candidate's declaration

I hereby declare that this dissertation submitted to obtain the academic degree of Philosophiæ Doctor (Ph.D.) in Product and Industrial Processes Engineeringis my own unaided work, that I have not used other than the sources indicated, and that all direct and indirect sources are acknowledged as references.
Parts of this dissertation have been published in international journals and/or conference articles (see list of the author's publications at the end of the dissertation).

Napoli, March 10, 2023

_____

Lorenzo Lombardi

Abstract

Most polymerization products must undergo a devolatilization process designed to remove solvents and residual monomers to comply with environmental regulations. Under very stringent process conditions such as high temperature and vacuum, a multiphase gas-liquid system occurs, such as a foam. Although nonaqueous foams have recently received attention, the influence of volatile components lacks the fundamental understanding to control foam properties.

In this dissertation, the process of static devolatilization of polymers is treated in its design aspects. A new tabletop static devolatilizer is presented to measure separation efficiency under various operating conditions. The measurement capabilities of the equipment are demonstrated by varying the initial concentration of volatiles, the degree of vacuum, and the design of the equipment.

Work was also done to improve the current understanding of the thermodynamics and kinetics of gas sorption in commercial elastomers commonly found in devolatilization processes. Experimental sorption isotherms were interpreted using the non-random lattice fluid equation of state. Absorption kinetics were also studied and interpreted using a Fick's model that determines values of mutual diffusivity as a function of temperature and mixture composition.

Another study was performed as part of this dissertation to investigate the physical mechanism leading to foam stabilization and liquid film drainage in binary mixtures with volatile compounds. Using an improved interferometry apparatus, we show that the foamability of polymer-volatile mixtures can be assessed by single bubble experiments. Two different solvents with different degrees of volatility were investigated, shedding light on surface bubble stabilization mechanisms.

Keywords: devolatilization, separation, polymers, foams, bubbles.

Sintesi in lingua italiana

La maggior parte dei prodotti di polimerizzazione deve essere sottoposta a un processo di devolatilizzazione volto a rimuovere i solventi e i monomeri residui per rispettare le normative ambientali. In condizioni di processo severe, come alta temperatura e vuoto, si può presentare un sistema multifase gas-liquido, come una schiuma. Sebbene le schiume non acquose sono attualmente oggetto di attenzione, non è stato pienamente compreso l'effetto di composti volatili sulle proprietà della schiuma.

In questa tesi, il processo di devolatilizzazione statica dei polimeri viene trattato nei suoi aspetti progettuali. Viene presentato un nuovo devolatilizzatore statico su scala di laboratorio per misurare l'efficienza di separazione in varie condizioni operative. Le capacità di misurazione dell'apparecchiatura sono dimostrate variando diverse condizioni operative e il design dell'apparecchiatura.

È stato anche svolto un lavoro sperimentale per migliorare l'attuale comprensione della termodinamica e della cinetica di assorbimento di gas in elastomeri utilizzati nei processi di devolatilizzazione. Le isoterme di adsorbimento sono state interpretate utilizzando il modello "non-random lattice fluid". La cinetica di assorbimento è stata interpretata utilizzando un modello Fickiano, determinando i valori di mutua diffusività in funzione della temperatura e della composizione della miscela.

È stato studiato sperimentalmente il meccanismo fisico, che porta alla stabilizzazione di una schiuma e al drenaggio di un film di liquido in miscele binarie con composti volatili. Utilizzando una nuova apparecchiatura interferometrica, abbiamo dimostrato che la schiumabilità delle miscele polimero-volatili può essere valutata mediante esperimenti con bolle singole. Sono stati analizzati due solventi con diversi gradi di volatilità, facendo luce sui meccanismi di stabilizzazione delle bolle in superficie.

Parole chiave: devolatilizzazione, separazione, polimeri, schiume, bolle.

Contents

Acknowledgements

At the end of such a long journey called a Ph.D., I would like to thank the people who have accompanied me during these years and whose presence has been essential. First, I would like to thank my supervisor Pier Luca for his invaluable advice and for continuing to believe in me. I would like to thank Daniele, an endless source of ideas who inspired me in the worst of times. I would like to thank my colleagues, Massimiliano, Massimiliano, Maurizio, Marco, Davide, Claudio, Stefano, Davide, and Nikos, for their daily company, support, and fun. I would like to reserve special thanks to John, who treated me as a member of his research group from the very beginning, and has been fundamental for me to become an independent researcher. I would like to thank my UBC colleagues: Alireza, Yun-Han, Sole, Ethyn, Roxy, Amar, Coralie, Lanxin, Max, Cody, and Anika for warmly welcoming and supporting me in an extraordinary experience. I would like to thank my dearest friends: Giulio, Filippo, Carmine, Dario, Jebbo, Oci, Pierpaolo, Pietro, Guara, Checco, Enrico, Lorenzo, Antonio, Luca, Massimo, Giovanni, Mattia. The countless experiences we have shared, and those yet to come, are and will be one of the things I value most. I would like to reserve a special thanks to Laura. Her determination, passion, and empathy have been a guiding light in this journey. I would like to thank my family for their unconditional love.

List of Acronyms

The following acronyms and abbreviations are used within the thesis.

DFI	Dynamic Film Interferometry
DV	Devolatilizer
EoS	Equation of State
EPDM	Ethylene Propylene Diene Monomer
FS	Falling Strand
LED	Light Emitting Diode
LF	Lattice Fluid
MSO	Melt Spreading Obstacle
NRHB	Non Random Hydrogen Bonding
NRLF	Non Random Lattice Fluid
PC-SAFT	Perturbed-Chain Statistical Associating Fluid Theory
PDMS	Polydimethylsiloxane
PET	Polyethylene terephthalate

PLA	Polylactic acid
PO	Perforated Obstacle
POE	Polyethylene oxide
PP	Polypropylene
PVT	Pressure-Volume-Temperature
SH	Superheat
SL	Sanchez-Lacombe
TPE	Thermoplastic Elastomer
UNIFAC	Universal quasichemical Functional group Activity Coefficients
VOC	Volatile Organic Compound

List of Figures

List of Tables

List of Symbols

The following symbols are used within the thesis

Roman letters

A	interfacial surface, m^2
b	number of lattice cells occupied by one molecule
Bo	Bond number
C	molar concentration, mol/m^3
D	diffusion coefficient, m^2/s
D_{00}	pre-exponential constant, m^2/s
D_{01}	pre-exponential constant, m^2/s
D_{02}	pre-exponential constant, m^2/s
E	devolatilization efficiency
$\bar{E}$	activation energy, J
E_C	intra-diffusion coefficient model parameter
E_D	intra-diffusion coefficient model parameter, K

F	VOCs mass flux, kg/(m$^2 \cdot s$)
G	NRLF model multiplicative correcting factor
g	acceleration due to gravity, m/s^2
$\bar{H}$	Henry's constant, Pa
$\hat{H}$	non-dimensional foam height
H_0	height of non-foamed polymer, m
h_0	initial film thickness at the bubble apex, m
h_c	film thickness at the bubble apex, m
h_{mean}	average film thickness, m
h_m	minimum film thickness, m
k	free-volume parameter for the Vrentas-Duda formalism
l	NRLF model parameter
$\hat{L}$	non-dimensional nucleation length
L_c	length of the capillary, m
L_n	nucleation length, m
$\dot{m}$	mass flow rate, kg/s
M_w	molecular weight, g/mol
M_∞	asymptotic diffusing substance amount, kg
M_t	diffusing substance amount after a time t, kg
N	total number of molecules in a mixture

n_1	air refractive index
n_2	liquid film refractive index
N_{AV}	Avogadro number, 1/mol
P	pressure, Pa
$\hat{P}$	non-dimensional DV pressure
$\widetilde{P}$	reduced pressure
P^*	pressure normalizing factor, Pa
P^0	vapor pressure at saturated conditions, Pa
P_b	bubble pressure, Pa
P_e	vapor pressure, Pa
P_s	liquid pressure at the bubble surface, Pa
P_v	vacuum pressure, Pa
q	number of lattice external contacts per molecule
R	bubble radius, m
r	radial coordinate, m
$\bar{R}$	universal gas constant, J/(K $\cdot$ mol)
R_0	initial bubble radius, m
R_1	Fresnel reflectivity coefficient (air-liquid)
R_2	Fresnel reflectivity coefficient (liquid-air)
R_c	bubble nucleii critical radius, m

R_f	liquid film radius, m
s	molecular shape factor
T	Temperature, K
t	time, s
$\widetilde{T}$	reduced temperature
T^*	temperature normalizing factor, K
t_c	viscocapillary time, s
t_d	bubble coalescence time, s
T_g	glass transition temperature, K
$\hat{V}$	specific volume, m^3/kg
$\hat{V}^*$	specific occupied volume at 0 K, m^3/kg
$\hat{V}_{FH}$	specific hole free volume, m^3/kg
$\hat{V}_{FI}$	specific interstitial free volume, m^3/kg
$\hat{V}_{FV}$	specific free volume, m^3/kg
$\hat{V}_S$	volume occupied by polymer skeleton, m^3/kg
$\widetilde{v}^*$	reduced volume occupied by a cell of a molecule
v^*	volume occupied by a cell of a molecule, m^3
$v^*_{sp,0'}$	closed packed specific volume scaling parameter, m^3/kg
$v^*_{sp,0}$	closed packed specific volume scaling parameter, m^3/kg
$v^*_{sp,1}$	homologous series of compounds constant, $m^3/(kg \cdot K)$

v_{sp}^* closed packed specific volume, m^3/kg

v_r velocity radial component, m/s

x molar fraction

z lattice coordination number

Greek letters

α light incident angle, rad

Γ_{00} free volume non-random distribution parameter

γ surface tension, N/m

ε^* average mean field interaction energy per mole, J/mol

ε_h^* enthalpic energy parameter, J/mol

ε_s^* entropic energy parameter, J/mol

η viscosity, $Pa \cdot s$

Θ refraction angle in the film, rad

θ surface contact fraction

λ light wavelength, m

μ^P penetrant molar chemical potential in the polymer-penetrant mixture, J/mol

μ^V penetrant molar chemical potential in the pure vapor/liquid phase, J/mol

ξ overlap factor for free volume

ρ density, kg/m^3

$\widetilde{\rho}$ reduced density, kg/m^3

ρ^* density normalizing factor, kg/m^3

ρ_g gas density, kg/m^3

ρ_l liquid density, kg/m^3

Σ non-dimensional superheat

σ_{rr} Radial component of tensile stress, Pa

ς molecule segment diameter, m

τ_{rr} viscous stress normal radial component, Pa

Φ light interference phase difference, rad

ϕ volume fraction

φ "close-packed" volumetric fraction

χ Flory-Huggins interaction parameter

ψ light interference phase shift, rad

ω weight fraction

Subscripts

O_2 oxygen

i mixture component i

in inlet

j mixture component j

out outlet

v	volatile
1	solvent
2	polymer

Chapter 1

Introduction

This introduction is divided into two parts. The first is a brief description of devolatilization fundamentals. Including the concepts needed to understand the process and its criticalities. The second part is aimed at establishing the objectives of the research. As of the date of submission of this manuscript, the main contents of Chapter 2 and Chapter 3 are intended for publication in peer-reviewed journals, and Chapter 4 has already been published.

1.1 An Overview of Polymer Devolatilization

Polymer devolatilization is a unit operation in which low-molecular-weight components, such as unreacted monomers, solvents, water, and various substances, are removed from the polymer after the polymerization stage [1, 2]. These components, often referred to as *volatiles* or VOCs if they are organic, must be removed to comply with various regulations [3–9], to improve the polymer's properties or for a variety of other reasons. It is well known that these substances, used for polymerization, are highly toxic and harmful to human health [10, 11]. Hence, removing them as much as possible from the processed polymers is crucial.

Devolatilization of a polymer is a complex process involving the transport of volatiles to a polymer-vapor interface. The volatiles can leave the polymer only if their vapor pressure is bigger than their partial pressure in the surrounding space. The difference between these two pressures is the

process's driving force which is generally referred to as *superheat* (SH), and it sets the maximum obtainable degree of separation. Its maximization is one of the main aspects of designing such a device, and the most common way to achieve it is to apply a strong vacuum on the apparatus. Given these conditions, the volatiles evaporate at the gas-liquid interface and are subsequently removed by the vacuum system.

On the other hand, it is necessary not just to look at thermodynamics. The time needed to achieve the maximum degree of separation depends on the rate at which the volatiles migrate through the polymer. The diffusion of the volatiles in the polymer regulates this mechanism, and it is relatively slow for concentrated polymer solutions ($10^{-8}-10^{-12}\ m^2/s$). The diffusion coefficient strongly depends on the system's temperature and the volatiles' concentration, as initially detailed by Vrentas and Duda.

Knowing thermodynamic and kinetic parameters is essential for an optimal process design. Although it is theoretically possible to predict these parameters, this procedure is highly precarious and can lead to incorrect estimates by several orders of magnitude. For example, the models in the literature are more accurate at low temperatures, whereas the devolatilization process is conducted at high temperatures. Hence, it is always advisable to measure these parameters. Gravimetric or barometric sorption techniques produced the most diffusivity and equilibrium data under devolatilization conditions [12, 13].

The mechanism regulating the diffusion of the volatiles through the liquid-vapor interface is complex and may vary among systems and applications. For example, foam formation is prevalent in apparatuses where a relatively high superheat is applied. Hence, many bubbles containing the volatiles nucleate within the solution, generating a multiphase system. These bubbles may then grow, coalesce, and eventually rupture at the polymer-vapor interface, where they release their volatile contents to the vapor phase. In systems of this type, the volatiles migrate to the liquid surface, to bubble nucleation sites, and to bubbles growing within the polymer, further confirming the complexity of such a system.

Foaming activity has been proven critical for foam devolatilization through vacuum or gas entrainment because it dramatically increases the surface area for mass transfer. It has been found that the separation performance is directly related to the number of bubbles present at the

steady state [14–17]. Therefore, quantifying the system's foamability and the stability and lifetime of bubbles is critical for process optimization. A fundamental study of this problem can be applied to process design. It can be helpful for optimal equipment selection and operation by correlating engineering parameters with fundamental material properties.

In light of these considerations, designing a devolatilization unit presents several technical challenges. More difficulties arise from the very viscous nature of the processed materials and the severe heat and mass transfer limitations accompanying the process. Often the process requirements are further complicated by simultaneous chemical reactions that affect the nature of the material being processed. Given these limitations, the separation equipment must be specially designed to induce flow patterns conducive to efficient separation.

1.2 Scope and Organization

The main motivation of the research presented in this dissertation lies in the necessity to investigate innovative devolatilization unit designs. Most of the currently available configurations were conceived more than three decades ago [18]. Therefore, there is an opportunity to take advantage of new experimental instruments and techniques and the knowledge gained over this time-lapse to gain a deeper understanding of process fundamentals and align it with today's requirements. One of the central focuses of this work is to improve the separation capabilities of a static devolatilizer and to provide a rationale design optimization with the aid of a novel small-scale apparatus.

In general, multiphase systems are always encountered in separation processes, such as polymer foams which are the main focus of this dissertation. Bubble coalescence is required to release devolatilized VOCs into the surrounding gas and can significantly affect the interfacial surface area for mass transfer. Hence, the foamability of these fluids and the stability of the resulting foams are of critical importance for polymer devolatilization. Shedding light on the foam stabilization mechanism is crucial to the devolatilization process optimization since foam stability is strongly correlated with removal efficiency. To this end, an extensive experimental campaign was conducted to thoroughly understand the drainage of

gas-liquid interfaces and stabilization mechanisms in binary mixtures with volatile compounds, typically encountered in industrial applications.

The present dissertation is structured as follows.

Chapter 2 presents a new experimental apparatus that consists of a table-top static devolatilizer. The removal efficiency of O_2 from silicone oil is measured by varying inlet O_2 content, degree of vacuum, and position in the devolatilizer. Finally, the impact of apparatus design on devolatilization performance is explored by designing two different 3D-printed obstacles. This chapter also addresses process optimization issues, proposing scaling relations that could be of practical importance.

Chapter 3 focuses on the absorption behavior of n-hexane vapor in a commercial propylene-ethylene elastomer, typically processed in industrial devolatilizers, by experimentally determining absorption isotherms and examining absorption kinetics.

Chapter 4 addresses from a fundamental perspective the mechanisms of foam stabilization in binary mixtures with volatile compounds, similar to those encountered in the apparatus presented in Chapter 2. Experimental measurements of liquid film drainage and bulk foam formation are presented therein.

Chapter 5 summarizes the results provided in this thesis and proposes possible stimulating paths for future research.

Chapter 2

Model lab-scale devolatilizer for high efficiency polymer-volatile separation

2.1 Introduction

Most polymerization products have higher or lower percentages of unreacted monomers, solvents, water and other additives [1]. All of these chemical species are recognized as volatile organic compounds (VOCs), which are generally toxic substances that must be devolatilized from the polymer to fulfill health and environmental regulations [3–9]. In the last years, regulations regarding VOCs have increased and become more restrictive, together with greater general attention to environmental protection and recycling of products. This explains the considerable interest in this area of research in recent years, indeed researchers have increased their scrutiny of novel geometrical configurations of devolatilizers [19],[20], [21] with the aim of increasing the efficiency of the process.

Devolatilizers may be broadly subdivided into rotating and nonrotating equipment, the main ones being flash evaporators, falling-film, falling-strand, wiped-film and single or multi-screw extruder [18]. Falling-strand devolatilizer is mainly used for low viscosity polymers, polymer strands are extruded and conveyed in a melt pool into a vacuum vessel and VOCs are removed from the polymer through concurrent diffusion and foaming.

This kind of equipment is extremely advantageous since there are essentially no moving parts, therefore key functions such as melt forwarding, mixing, and surface generation are supported by the combination of gravity, bubble nucleation, growth and disengagement [22].

Albalak et al. [23], [24] assessed the effect of vacuum exposure time on bubbles nucleation and growth within a polymer falling strand, their experiments show a styrene removal efficiency of about 80% within the first 18 seconds of exposure of the strand to vacuum. It seems that the falling time is not sufficient to obtain a complete removal of the solvent. The aforementioned experiments were executed in batch conditions, measuring the residual volatile concentration off-line, with gas chromatography.

Although this technique made the setup more flexible in terms of processable volatiles, there was no information about the efficiency immediately after the devolatilization zone and the operation was very time-consuming. Furthermore, the batch conditions may have increased the gap between laboratory scale and what could have been a continuous industrial process. Other previous studies in this area of research reported the importance of bubbles lifetime within the melt pool [22],[25] and consequently of polymer melt residence time within the vessel. Little information is understood about how the design of a falling strand devolatilizer can improve process performances. Some constructive solutions, such as "Chinese hats" or melt spreading surfaces are reported in [1], but these are not supported by sufficient experimental data, and their principle of operation is still unclear.

This chapter presents a novel design solution for improving removal efficiency in a falling strand devolatilizer, supported by experimental results at different operating conditions. In particular, the bottom part of the vessel, a melt spreading surface, has been properly 3D printed to obtain geometries leading to different results. The mixture of silicon oil and oxygen is used as polymer solution like most experimental studies in the field which report silicon oil as viscous fluid [16], [19], [26] to simulate the behavior of industrial polymers. The focus is the trend of removal efficiency varying several parameters, such as vacuum degree, volatile concentration, and polymer solution residence time.

First, a comprehensive theoretical overview of polymer devolatilization is provided. The fundamentals of the process are analyzed in detail and

the most common industrial equipment is depicted. Second, the experimental procedure to study the effect of DV falling design design on removal efficiency is presented.

2.2 Theoretical Background

Removing volatile components from the concentrated polymer melt is a vital separation step in plastics processing, to name a few examples: unreacted reactants in reactive extrusion, moisture in post-costumer recycling extrusion, and unreacted monomer or solvent in polymerization. This process is known as devolatilization (DV). Since it is a separation process operated by diffusion, increasing the diffusion area is a logical way to improve the separation. The rate of diffusion and the rate of generation of the effective surface area becomes the primary mechanism of DV.

It is common practice to form foams to achieve separation. Foam formation in the molten polymer by pressure reduction or purging with inert gases allows a substantial increase in interfacial mass transfer area to maximize separation efficiency. In this case, foam growth and breakup are also necessary steps for DV. Thermodynamic instability of polymer solutions, also known as supersaturation, causes bubble nucleation. Increasing temperature or reducing pressure are standard methods to produce such supersaturated systems.

DV is recognized as a unit operation of polymer processing and is performed in the industry with a wide variety of equipment. Various physical and chemical techniques with varying VOC removal performances are currently used. The most common and reported devolatilization procedure is first examined in depth, focusing on the physical mechanisms, the parameters governing the process, and a description of the equipment.

In the devolatilization process, the removal of VOCs relies on their diffusion from the polymer to the gas phase to transport them out of the DV plant. Therefore, the diffusion coefficient, the thermodynamic equilibrium, and the interfacial area are critical parameters that can be tuned to enforce the technique and achieve appropriate purification results [1, 2, 25, 27]. In the purification of a molten polymer by devolatilization, there are two dominant mass transfer mechanisms: diffusion and bubble nucleation-foam formation (Figure 2.1). Additionally, the devolatilization

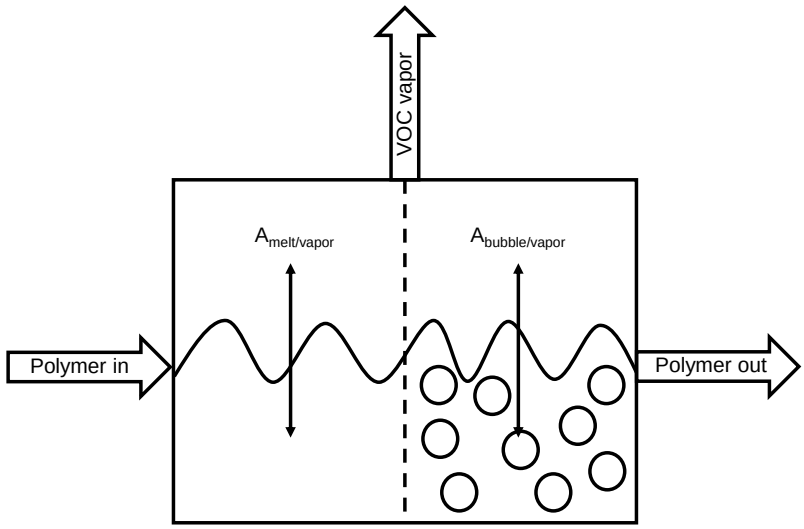

Figure 2.1: Schematic representation of the devolatilization process. Diffusion from polymer melt (left) and foaming (right) mechanisms with A representing the interfacial area between phases. Adapted with permission from [18]. Copyright 2019 American Chemical Society.

rate can be improved by introducing a stripping agent in the system.

2.2.1 Thermodynamic equilibrium

Polymer melts consisting of a homogeneous mixture of polymer and VOC (or solute) are not ideal solutions from a thermodynamic point of view. Therefore, the constraints generated by the macromolecules and the polymer-VOC interactions have to be taken into account. For this, the Flory-Huggins equation may be used:

$$\ln\left(\frac{P_{e,1}}{P_{e,1}^{0}}\right) = \ln(1-\phi_2) + \phi_2 + \chi\phi_2^2 \tag{2.1}$$

where ϕ_2 is the volume fraction occupied by the polymer, $P_{e,1}$ is the vapor pressure of the volatile component in equilibrium with the polymer solution, $P^0_{e,1}$ is the vapor pressure of the pure volatile component, and χ is the Flory-Huggins interaction parameter representing the interdispersion energy of the polymer and solute molecules. The Flory-Huggins interaction parameter can be determined from equilibrium solubility data in which the volume fraction of solvent, ϕ_1, is known as a function of the solvent activity. Alternatively, ϕ can be estimated, assuming that the polymer-solvent compatibility can be appraised through comparisons of solubility parameters [28, 29].

Where the volatile concentration is low, $\phi_2 \rightarrow 1$ and Equation 2.1 simplifies to:

$$\ln\left(\frac{P_{e,1}}{P^0_{e,1}}\right) = \ln(1-\phi_2) + 1 + \chi \tag{2.2}$$

rearranging Equation 2.2 and shifting to a weight fraction basis, we obtain:

$$P_{e,1} = \frac{\rho_2}{\rho_1} P^0_{e,1} \omega_1 \exp(1+\chi) \tag{2.3}$$

where ω_1 is the weight fraction of the volatile in the melt, while ρ_1 and ρ_2 are the densities of the pure volatile and polymer, respectively. Equation 2.3 shows how a reduction of the vapor pressure minimizes the mass of volatile present in the polymer matrix. Additionally, an increase in temperature reduces the volatile weight fraction, affecting thermodynamic equilibrium, as shown in Figure 2.2.

2.2.2 Mass Transfer Mechanism

Polymer devolatilization is a process based on mass transfer. The volatiles in the liquid phase diffuse to the polymer/vapor interface, where they leave the melt and are eventually conveyed out of the vessel. The mass balance of the volatile component under steady state conditions is:

$$\omega_{in}\dot{m}_{in} = \omega_{out}\dot{m}_{out} + \omega_v \dot{m}_v \tag{2.4}$$

where ω_{in} and ω_{out} are the inlet and outlet mass fractions of volatile in the polymer, respectively, and the same subscript is adopted for the inlet

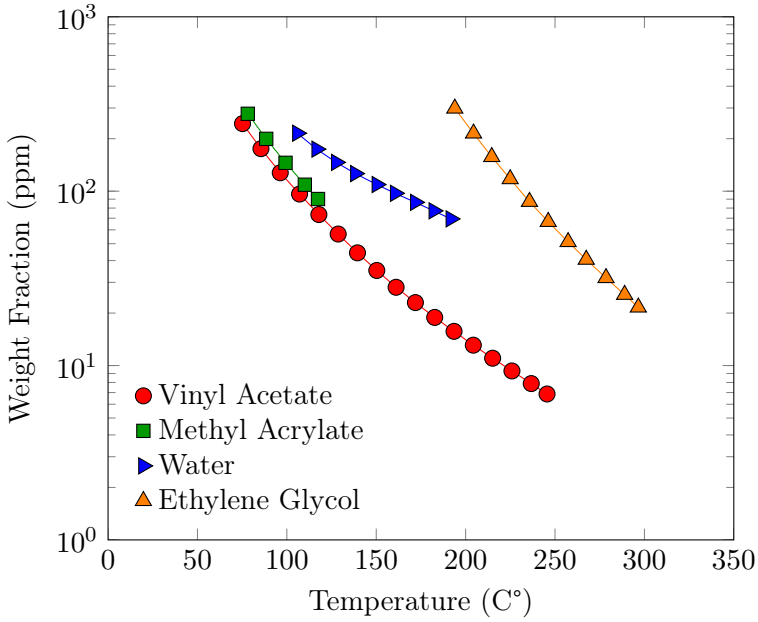

Figure 2.2: Theoretical calculation of the weight fraction of different solutes in polymer solutions as a function of the temperature under a pressure of 100 Pa and $\chi = 0.3$. Adapted with permission from [18]. Copyright 2019 American Chemical Society.

and outlet liquid mass flow rates $\dot{m}_{in}$ and $\dot{m}_{out}$. While $\dot{m}_v$ is the gas mass flow rate leaving the vessel and ω_v is the mass fraction of VOC exiting the vessel in the gas phase. VOCs removal rate ($\omega_v \dot{m}_v$) can be expressed in terms of interfacial area A as follows:

$$\omega_v \dot{m}_v = FA \tag{2.5}$$

where F is the flux of VOCs through the interface.

The total interfacial area is the sum of the molten polymer surface's interfacial area and each bubble's interfacial area. In the case of a diffusion mechanism, the interfacial area of each bubble is zero. Therefore, the only term that affects the VOC removal rate is the interfacial area of the polymer fused with the VOC vapor. In the case of a bubble foam

devolatilization mechanism, the interfacial area between the bubbles and the polymer mass and between the bubbles and the VOC vapor must be considered to calculate the removal rate.

In conclusion, the interfacial area is a crucial parameter in the devolatilization process, as it directly influences the removal rate of VOCs present in a polymer melt, regardless of the mechanism in place. The interfacial area may be maximized by renewing the surface of the polymer melt, which can be achieved by mechanical agitation and generating bubbles and foam in the melt, generating bubbles and foam in the polymer melt. This will be explained in more detail in the following sections.

2.2.3 Diffusion Mechanism

Diffusion of volatiles through the polymer for their removal occurs due to a concentration gradient. An overview of the process is illustrated in Figure 2.3. The VOC-containing polymer enters the devolatilization device, and then the VOCs diffuse through the polymer melt to the vapor phase. Volatiles are reduced to a concentration that depends on the efficiency of the equipment. The molten polymer then exits the DV to be processed in subsequent stages.

The diffusion of volatiles in polymer melts is a complex phenomenon depending on teperature and voatile concentration. This dependence is extreme near the polymer's glass transition temperature, and Duda, Vrentas, and coworkers have developed one of the most widely used models to predict the diffusion coefficient [30–32]. They studied different polymer-solute systems in a wide range of temperatures and concentrations. Their model uses the concept of free volume, introduced by Cohen and Turnbull [33], which is the volume not occupied by the polymeric chains ($\hat{V}_{FV}$).

$$\hat{V} = \hat{V}_{FV} + \hat{V}_S \tag{2.6}$$

here $\hat{V}$ is the total volume and $\hat{V}_S$ is the volume occupied by the polymer skeleton. Free volume increases at high temperatures and high volatile concentrations because of the increased mobility of volatile molecules under these conditions.

Vrentas and Duda adopted the theory of Berry and Fox, who divided the total free volume into two components: the home free volume ($\hat{V}_{FH}$)

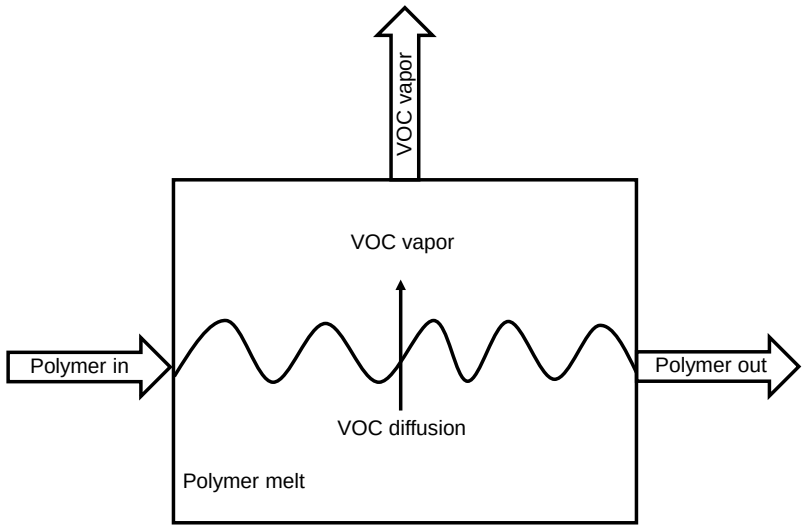

Figure 2.3: Schematic representation of the process of VOC diffusion from a polymer melt. Adapted with permission from [18]. Copyright 2019 American Chemical Society.

which is available for molecular transport, and the interstitial free volume ($\hat{V}_{FI}$) which is unavailable for molecular transport [34]. The diffusion coefficient of a solute diffusing in a polymer matrix is expressed as follows:

$$D = D_0 \exp\left(-\frac{\bar{E}}{\bar{R}T}\right) \exp\left[-\frac{\xi(\omega_1 \hat{V}_1^* + \omega_2 \xi \hat{V}_2^*)}{\hat{V}_{FH}}\right] \tag{2.7}$$

where ω_1 and ω_2 are the volatile and polymer weight fractions, respectively. D_0 is the pre-exponential constant, $\bar{E}$ is the activation energy of a molecule to overcome the attractive forces between neighbors, and ξ is the ratio of the molar volumes of the solvent and polymer units involved in discrete diffusive jumps. The specific volumes $\hat{V}_1^*$ and $\hat{V}_2^*$ are the smallest holes that need to form before a solvent, and a polymer molecule can take diffusive steps. They are estimated as the specific volumes of the solvent

and polymer at absolute zero temperature. Finally, ξ is the overlap factor for free volume, introduced because the same free volume is available to more than one molecule, and $\bar{R}$ is the universal gas constant.

The total free volume available for diffusion, $\hat{V}_{FH}/\xi$, is computed as a weight fraction average of pure components:

$$\frac{\hat{V}_{FH}}{\xi} = \omega_1 \left(\frac{K_{11}}{\xi}\right)(K_{21} - T_{g1} + T) + \omega_2 \left(\frac{K_{12}}{\xi}\right)(K_{22} - T_{g2} + T) \quad (2.8)$$

where subscripts 1 and 2 refer to the solvent and polymer, respectively, and the K_{ij} parameters represent the amount of hole free volume within the pure components. More recent reports have demonstrated that devolatilization cannot be explained exclusively by the diffusion mechanism [2, 24, 35]. Even at low concentrations of volatiles, other mechanisms, such as bubble nucleation and growth, take place. Those mechanisms are explained in the next section.

2.2.4 Foaming Mechanism

Although foam formation is the other driving mechanism of devolatilization, it was not considered in early attempts to develop a model that could describe the process. Latinen proposed a bubble-free mass transfer model for DV in a single screw extruder, taking into account the axial diffusion effect in extruders and discovering how it could be detrimental to the process [36]. Subsequent experiments showed that the diffusion coefficient derived from Latinen's model was wrong by several orders of magnitude, undermining the accuracy of his results. The back-mixing problem has been more rigorously addressed by Roberts, who developed a model including the renewal of the mixture surface as an effect of mixing [37].

Various modifications to Latinen's theory have been suggested from the late 1960s onward [37–39], but the reason for the discrepancy between the results predicted by the model and the experimental data was identified by Collins et al. [40]. Using experimental data for diffusivity, Collins et al. compared their experimental results with those of Latinen. Their predictions turned out to be in fair agreement with the experimental data, although they systematically overestimated them. This discrepancy was attributed to an incorrect estimation of the surfaces through which matter

transport occurs. Based on these considerations, Collins et al. concluded that Latinen's model was accurate if no bubble formed.

One of the first authors to consider bubble formation in a DV process was Denson [41]. The same problem has been widely addressed by Biesenberger et al. [14–17]. Biesenberger measured devolatilization efficiency by varying experimental conditions, such as polymer flow rate, vacuum degree, and polymer viscosity, providing valuable results for developing theoretical models, including foam formation.

In many industrial processes, the volatile components are continually removed from molten polymer through foam formation, growth, and rupture into a contiguous gas phase. Figure 2.4 shows a schematic representation of the process. Bubbles are nucleated and grow due to the diffusion of VOCs through the polymer mass to the gas phase. These bubbles aggregate to form a foam at the polymer-melt-gas interface. This foam may remain longer or shorter depending on the sample's viscosity and surface tension, among other parameters. Finally, VOCs are removed from the molten polymer pool by applying a vacuum.

The liquid must be supersaturated by the volatile for bubbles to form and nucleation to begin. This occurs when the temperature exceeds values where the equilibrium vapor pressure equals the pressure around the polymer melt. The superheat conditions are also achieved, decreasing the pressure of the system below the equilibrium pressure of the volatile [14, 35, 42, 43].

The bubbles are nucleated by so-called embryos i.e. bubbles of extremely small radius [44]. The driving force for bubble growth is the difference between the vapor pressure of the volatile at the local temperature and concentration, $P_{e,1}$, and the pressure in the bubble P_b. The latter is not necessarily equal to the absolute pressure in the surrounding liquid, P. One reason why P and P_b may be different is due to the surface tension σ. In fact, the following relationship applies:

$$P - P_b = \frac{2\sigma}{R} \tag{2.9}$$

where R is the bubble radius.

An embryo can only grow if $P_{e,1} > P_b$, hence the minimum radius R_c

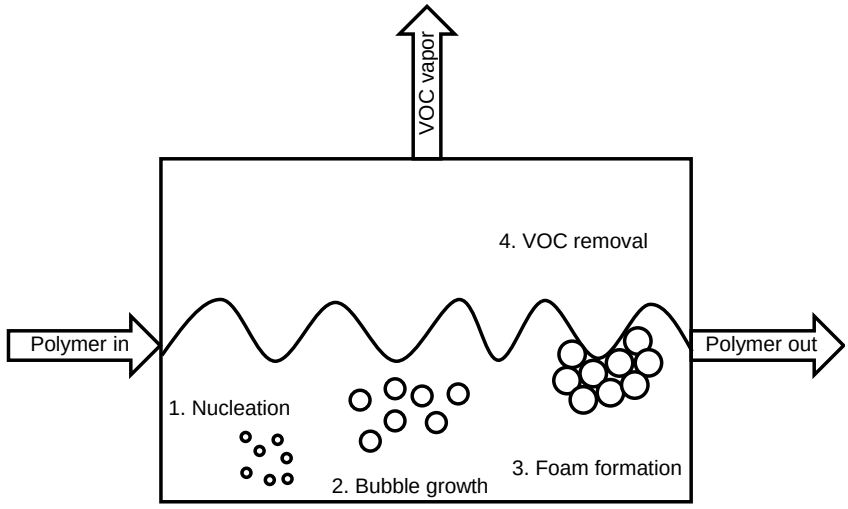

Figure 2.4: Schematic representation of a foam enhanced devolatilization process. Adapted with permission from [18]. Copyright 2019 American Chemical Society.

required for an embryo to become a bubble is determined:

$$R_c = \frac{2\sigma}{P_{e,1} - P_b} \tag{2.10}$$

When an embryo has a radius significantly greater than R_c, surface tension no longer affects it, but this does not imply that the pressure in the bubble under such conditions is equal to the pressure in the surrounding liquid since hydrodynamic effects may be significant. For example, the generation of a bubble within a viscous fluid induces an extensional flow in the surrounding fluid and, thus, a stress τ that compresses the bubble. Equation 2.9 is readily modified:

$$P_b - P_s + \tau_{rr} = \frac{2\sigma}{R} \tag{2.11}$$

where P_s is the pressure of the liquid at the bubble surface and τ_{rr} is the normal radial component of the viscous stress which is given by:

$$\tau_{rr} = 2\eta \frac{\partial v_r}{\partial r} \tag{2.12}$$

v_r representing the radial component of the velocity in the liquid and η the liquid viscosity.

The radial component of the stress tensor inside the bubble was neglected since the gas viscosity is negligible compared to the liquid. Neglecting hydrostatic pressure we have:

$$P - P_s = 0 \tag{2.13}$$

Substituting Equation 2.12 and Equation 2.13 into Equation 2.11 we obtain:

$$P_b - P - \frac{2\sigma}{R} = \frac{4\eta}{R}\left(\frac{dR}{dt}\right) \tag{2.14}$$

Equation 2.14 is a particular case of the well-known extended Rayleigh equation presented by Scriven et al. in which the inertial terms have been omitted [45].

For a bubble containing only solvent the pressure in the bubble, P_b is equal to $P_{e,1}$. Although P_b is time-dependent, the literature suggests that during the initial stages of growth, the pressure within the bubble does not vary significantly with time [46]. Under these assumptions, for constant ambient pressure, Equation 2.14 may be integrated with the initial condition $R = R_0$ at $t = 0$ leading to:

$$R(t) = R_c + (R_0 - R_c)\exp\frac{(P_b - P)t}{4\eta} \tag{2.15}$$

2.2.5 Addition of Stripping Agent

The devolatilization temperature is a significant factor in the VOC removal process. An excessive increase in temperature can lead to the abrupt degradation of the polymer. Conversely, a very low temperature may slow the diffusion of volatiles in the polymer, with obvious repercussions on separation efficiency. Additionally, the diffusion rate decreases when low

VOCs concentrations are achieved as observed in Table 2.1.

Table 2.1: Diffusion coefficients at different temperatures for different weight fractions of toluene in polystyrene [47].

Diffusivity (m^2/s) $\times 10^{-6}$				
T (°C)	**Toluene Weight Fraction**			
	0.05	0.1	0.4	0.6
110	0.03	0.2	1	0.7
140	0.4	0.9	3.7	1.0
160	0.8	2.5	5.6	1.8
170	1	4.4	6.8	2.5
178	1.6	5.3	7.5	3.1

The substantial decrease in diffusivity as the concentration of the volatile component approaches zero or as the temperature decreases may be partially overcome by adding an inert substance (usually water) that reduces the weight fraction of the polymer in the system [48]. A scheme of a stripping operation is shown in Figure 2.5. Other advantages of adding an inert substance were noted by Biesenberger and Sebastian [49]:

1. Adding an inert substance to the system reduces the partial pressure of the volatile component, reducing its weight fraction at equilibrium.

2. The combined vapor pressures of both the inert substance and the volatile component reduce the temperature and volatile concentration needed to bring about the boiling of the polymer solution.

3. The boiling of the inert substance creates bubbles that increase the area available for mass transfer from the polymer to the vapor phase.

Without polymer expansion by foaming, VOCs are removed from the polymers by diffusion. In this case, the improvement in devolatilization efficiency due to the presence of a stripping agent is related to the increase in the free volume of the polymer. An increase in free volume leads to an increase in the diffusion coefficient of VOC.

Vrentas and Duda reformulated the free volume theory for a ternary system in a polymer film to include the stripping agent's effect [50]. The

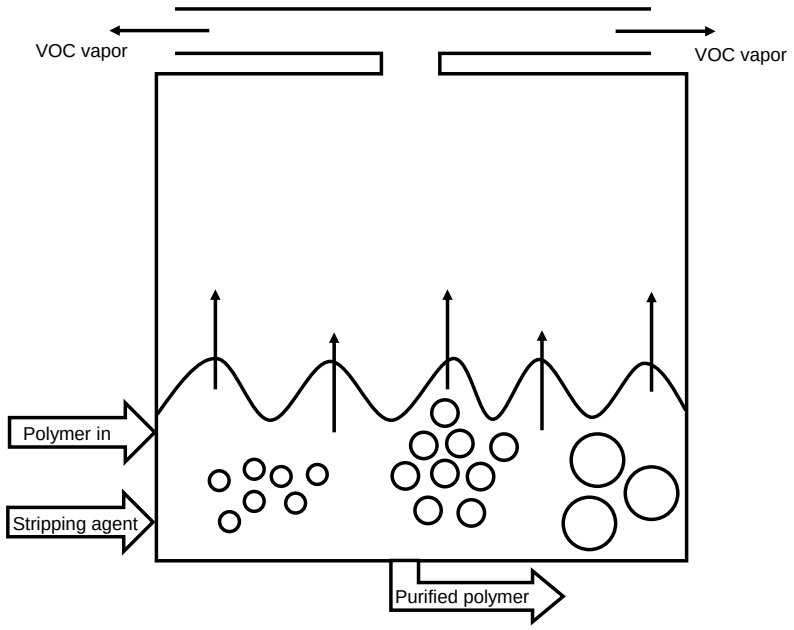

Figure 2.5: Scheme of a stripping operation. Adapted with permission from [18]. Copyright 2019 American Chemical Society.

diffusion coefficients of volatile D_1 and of stripping agent D_3 read as follow:

$$D_1 = D_{01} \exp\left(-\frac{E}{RT}\right) \exp\left[-\frac{\xi\left(\omega_1 \hat{V}_1^* + \omega_2 \xi_{12} \hat{V}_2^* + \frac{\omega_3 \hat{V}_3^* \xi_{12}}{\xi_{23}}\right)}{\hat{V}_{FH}}\right] \quad (2.16)$$

$$D_2 = D_{02} \exp\left(-\frac{E}{RT}\right) \exp\left[-\frac{\xi\left(\frac{\omega_1 \hat{V}_1^* \xi_{23}}{\xi_{12}} + \omega_2 \hat{V}_2^* + \omega_3 \hat{V}_3^* \xi_{23}\right)}{\hat{V}_{FH}}\right] \quad (2.17)$$

where ω_3 is the stripping agent weight fraction. D_{01} and D_{02} are the pre-exponential constants, ξ_{12} is the ratio of the molar volumes of the solvent and polymer units involved in discrete diffusive jumps, and ξ_{23} is the same but for stripping agent and polymer. $\hat{V}_3^*$ is the smallest hole that need to form before a stripping agent, and a polymer molecule can take

diffusive steps. They are estimated as the specific volumes of the solvent and polymer at absolute zero temperature.

The total free volume available for diffusion, $\hat{V}_{FH}/\xi$, is computed as a weight fraction average of pure components:

$$\frac{\hat{V}_{FH}}{\xi} = \omega_1 \left(\frac{K_{11}}{\xi}\right)(K_{21} - T_{g1} + T) + \omega_2 \left(\frac{K_{12}}{\xi}\right)(K_{22} - T_{g2} + T) + \omega_3 \left(\frac{K_{13}}{\xi}\right)(K_{23} - T_{g3} + T) \tag{2.18}$$

where subscripts 1,2 and 3 refer to the solvent and polymer, and stripping agent, respectively, and the K_{ij} parameters represent the amount of hole free volume within the pure components.

2.3 Devolatilization Equipment

This section describes the different types of equipment employed for developing polymers. These types of equipment are commonly divided into non-rotating (or stationary) and rotating devolatilizers, as summarized in Table 2.2. Nonrotating equipment relies on gravitational forces to transport the polymer through the devolatilization zone. While in rotating equipment, the melt is carried by contact with moving elements. As a result, the viscosities handled by nonrotating devolatilizers are much lower than those handled by rotating ones.

Table 2.2: Most common devolatilization equipment in each category.

Nonrotating devolatilizers	**Rotating devolatilizers**
Flash devolatilizer	Wiped-film evaporator
Falling-film devolatilizer	Screw extruder
Falling-strand devolatilizer	Disk processor

2.3.1 Flash Devolatilizer

This equipment is used for shear-sensitive, non-heat-sensitive, low-viscous polymers ($\eta \ll 1$ Pa $\cdot$ s). First, The polymer to be devolatilized is first heated in a long tube (sometimes spiral) using an external heat transfer medium. Then, the polymer enters the flashing chamber, where the pressure and temperature are adjusted according to the VOCs to be extracted. VOC removal occurs in a continuous vacuum, and the purified polymer is collected at the chamber's exit and may be discharged using a gear pump. In addition to vacuum, stripping agents such as nitrogen or steam improve extraction efficiency.

Thermoplastics, low-density polyethylene, polypropylene, polystyrene, and related copolymers or diorganopolysiloxanes are examples of polymers that can be purified by flash evaporation. For example, the purification of polystyrene at 133 Pa and 260°C reduced the styrene content from more than 1.8×10^3 ppm to about 26 ppm [51]. For diorganopolysiloxanes, with a viscosity range of 10^4 cps to about 2×10^5 cps at 25°C, purification using steam as a stripping agent was reported. A partial vacuum and a temperature below the evaporation temperature of the cyclic polysiloxanes were applied to samples containing between 9 and 18 wt% of cyclic polysiloxanes, achieving a final concentration of 2% by weight [52].

When considering vapor flashing from a melt, there are basically three regimes, each with distinct rate-limiting mechanisms, and each largely dependent on SH [53], the degree of "superheat" a term often used in industrial practice and defined here as

$$SH = P_{e,1} - P_v \tag{2.19}$$

where $P_{e,1}$ is the saturation pressure of the volatile in the melt and P_v is the vacuum pressure in the chamber.

The first of these regimes, termed "free boiling," occurs when SH is large, and the viscosity of the liquid is often relatively low. This usually occurs with high volatile content. Vapor bubbles form rapidly and expand by mass transfer from the liquid phase and coalescence. The resulting convective mixing reduces the depletion of volatiles at fusion-vapor interfaces and further promotes mass transfer to the vapor phase.

Devolatilization rates in the free-boiling regime are ultimately limited

by operational problems caused by excessive melt-vapor foam expansion and entrainment in the vapor line. These problems are related to the mechanisms of bubble coalescence and steam disengagement. With free boiling, the melt temperature can drop rapidly without external energy input since the latent heat of vaporization is provided mainly by sensible heat. For example, under adiabatic conditions, a styrene-polystyrene melt at about 250°C decreases by about 12°C for every 10 wt % melt vaporizing.

As the melt temperature decreases, P decreases, and superheat decreases. The viscosity of the melt will increase due to both the decrease in temperature and the removal of volatiles. These effects cause the growth and movement of bubbles to slow down and the free-boiling regime to disappear gradually.

The second regime is termed "bubble growth." It characterizes devolatilization conditions where superheat has decreased, and viscosity has increased to the point that bubble initiation and growth now become the controlling mechanisms for velocity. The process is no longer limited by foam expansion and gas entrainment. Because volatile removal is slower in this regime, cooling is reduced (even without external energy inputs). The viscosity of the melt will increase due to the further depletion of volatiles, even under isothermal conditions.

With the third regime, "diffusion control," superheating is now at a low value due to volatile depletion and temperature drop due to volatile depletion and temperature drop. As a result, there is little or no new bubble formation, existing bubbles grow very slowly, and their coalescence and disjunction practically cease. The rate of volatile loss is now relatively slow, being controlled mainly by molecular diffusion at the fusion-vapor interface in the devolatilization chamber. In this case, the process will be quasi-isothermal, with no thermal or mechanical heating. Surface regeneration can accelerate devolatilization in this regime, but an FSD inherently has limited capacity. Therefore, in cases of devolatilization dominated by this regime, such as where very low levels of residual volatiles are desired, equipment designs involving mechanical means of surface generation are likely to be preferred.

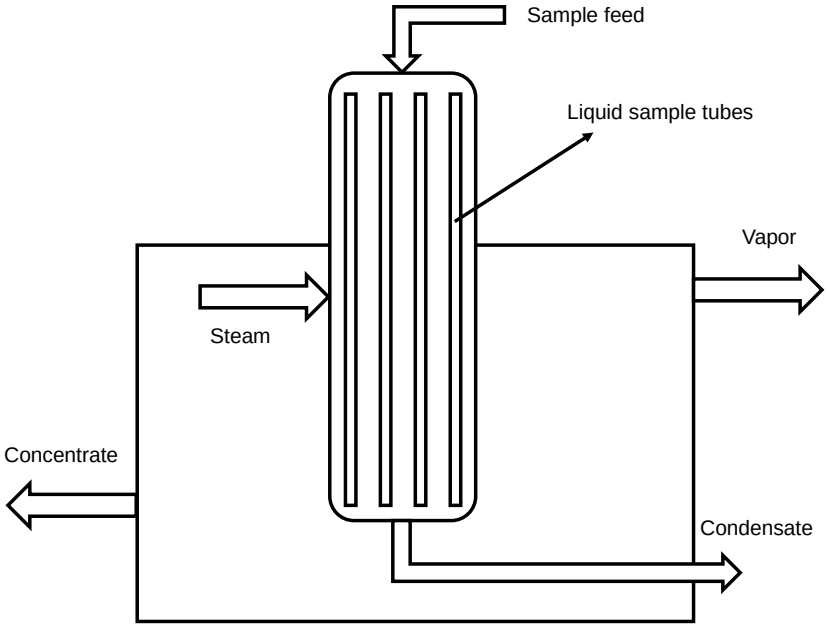

Figure 2.6: Schematic of a falling-film devolatilizer. Adapted with permission from [18]. Copyright 2019 American Chemical Society.

2.3.2 Falling-Film Devolatilizer

This technique is mainly applied in the case of heat-sensitive and low-viscous polymers. The feed introduced into the top of the reservoir forms continuous thin films along the walls, taking advantage of gravity. The volatiles are extracted from the sample by applying vacuum, and the purified polymer is recovered at the bottom of the reservoir, as shown in Figure 2.6.

In falling film devolatilizers, the liquid surface per unit volume is greater than in flash devolatilizers, leading to greater mass and heat transfer. An enhanced heat transfer reduces the overall cost of the process. While a greater active surface for mass transfer increases VOCs removal efficiency. This technique can purify polysiloxanes, polyvinyls, and polyesters [54].

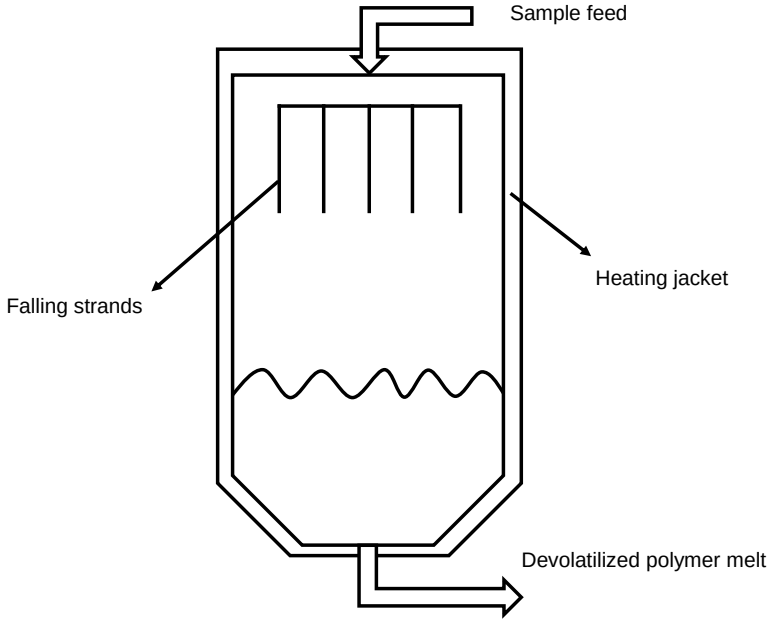

Figure 2.7: Schematic of a falling-strand devolatilizer. Adapted with permission from [18]. Copyright 2019 American Chemical Society.

2.3.3 Falling-Strand Devolatilizer

Viscous polymers ($\eta \approx$1–10 Pa · s) containing a lower VOC concentration than in the prior cases can be successfully purified with this method due to the maximization of the surface area exposed to the vacuum resulting in greater heat and mass transfer. In this configuration, the material enters the vacuum chamber as many filaments fall by gravity into the accumulated melt pool below (Figure 2.7). The free fall of the threads allows easy disengagement of already nucleated bubbles. During the free fall of the liquid, the configuration allows new bubbles to nucleate and grow without the influence of shear or external pressure gradients.

Unlike the falling-film devolatilizer, in the falling-strand configuration, volatiles not only exits the strand by diffusion but also form volatile bubbles in the core of the melt. Albalak et al. [23, 24] studied the devolatilization of a falling polyethylene strand under vacuum. They found that the

devolatilization proceeds through the formation of micro-blisters (1–15 μm diameter) on the surface of the strand and on the surface of the volatile bubbles formed in the core of the polymer strands.

Polystyrene, polyethylene, and polysiloxanes are polymers purified with a falling-wire devolatilizer. A patent reports that polystyrene containing 10-40 wt % styrene was treated at 200-280 °C under pressure between 6.7 $\times$ 10^3 and 26.7 $\times$ 10^3 Pa in the first tank and from 400 to 2.7 $\times$ 10^3 Pa in the second tank [55]. The final VOC content was less than 0.1 wt % and, in most cases, less than 0.5 wt %. A VOC content of less than 0.05-0.01 wt % was achieved in most cases.

2.3.4 Wiped-Film Evaporator

This rotating devolatilizer is used to process heat-sensitive, viscous polymers ($\eta < 10^3$ Pa $\cdot$ s). It solves polymer degradation due to long residence times in non-rotating equipment, fouling of heat transfer surfaces, and the limitations of mass and heat transfer. The movement of the rotor allows the surface to be constantly renewed, improving heat and mass transfer. However, it is more expensive and, compared with other rotary equipment, has a low rotational speed.

The polymer is fed from the top of the equipment, and the purified product is recovered from the bottom. The purified product is recovered from the bottom. The volatiles can exit the tank either from the top (countercurrent) for more volatile compounds or from the bottom (concurrent) for less volatile compounds. The rotor is equipped with paddles to transport the polymer films forming on the tank's walls (Figure 2.8).

The wiped film evaporator can be used for the purification of polysiloxanes, nylon-6 and polystyrene. For example, the purification of polystyrene containing 1.8 $\times$ 10^4 ppm styrene at a temperature of 250 °C and a pressure of 666 Pa, with a polymer melt flow rate of 4 $\times 10^3$ kg $\times$ h^{-1}, yielded a final styrene concentration of 400 ppm. final styrene concentration of 400 ppm [56].

2.3.5 Screw Extruder

Screw extruders mainly purify high-viscosity polymers ($\eta > 4\times$ 10^4 Pa $\cdot$ s) containing a very low VOC concentration. There are single- screw

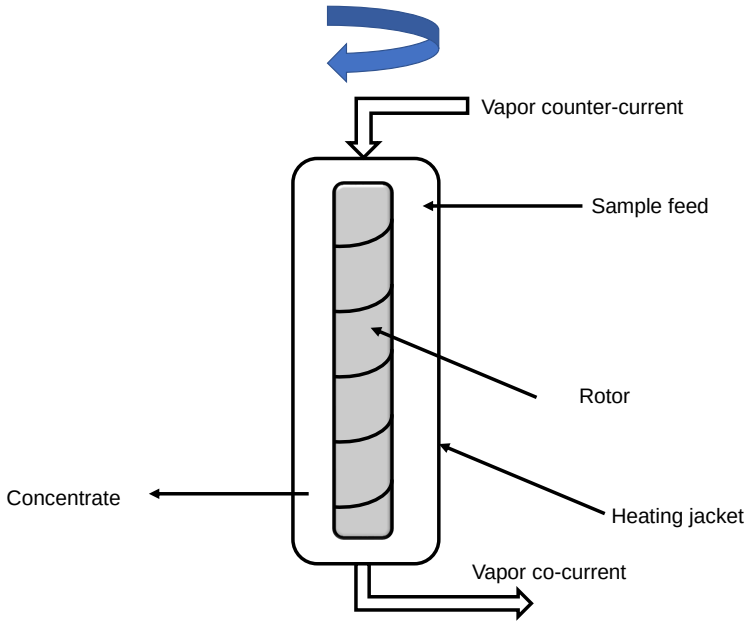

Figure 2.8: Schematic of a wiped-film evaporator. Adapted with permission from [18]. Copyright 2019 American Chemical Society.

extruders or twin-screw extruders. Both consist of a feed hopper with two dosing zones, one after the feed zone and one at the end of the screw, and a dosing zone where the polymer is devolatilized under vacuum (Figure 2.9).

Screw extruders can be used for the purification of, for example, polypropylene, polyethylene, polystyrene, polydimethylsiloxanes, and related copolymers. Biesenberger and Kessidis [57] reported removing styrene from polystyrene using a single screw extruder. They studied the most suitable conditions in terms of length of vent zones, screw speed, pressure, and measuring styrene content with gas chromatography. Under the optimized conditions, complete styrene from a polystyrene sample containing 5.4×10^3 ppm styrene was obtained under vacuum at 204°C.

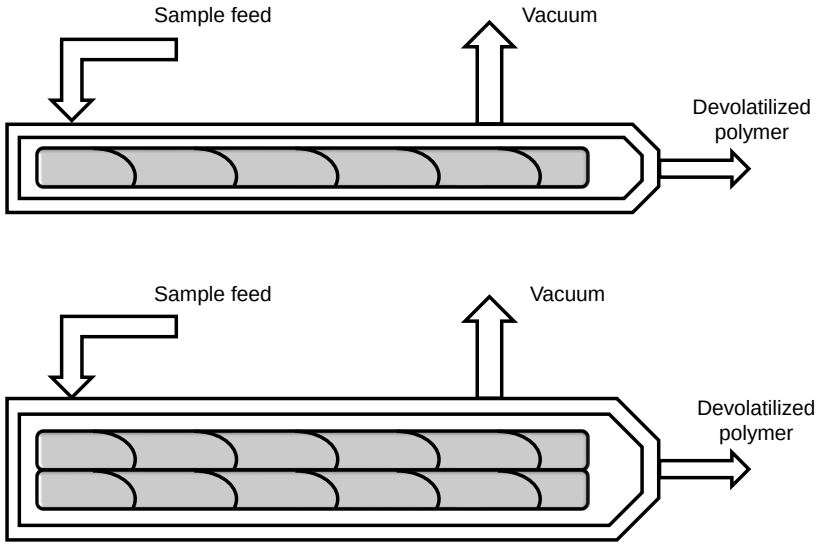

Figure 2.9: Schematic of screw-extruder devolatilizer. Single-screw extruder (top) and twin-screw extruder (bottom). Adapted with permission from [18]. Copyright 2019 American Chemical Society.

2.3.6 Disk Processor

In this device, the sample enters from above into a processing chamber formed by two disks attached to a shaft processing chamber formed by two disks attached to a shaft surrounded by a barrel [58–61]. The outlet is positioned at the same height as the inlet but separated by a channel block (Figure 2.10). Depending on the desired function, devolatilization, mixing, melting, or pumping, many modifications are available.

In the case of devolatilization, the molten polymer is distributed on the walls forming a film, the thickness of which can be controlled by the operating parameters and sample feed. A rotating melt pool is created, which increases the circulation speed and surface renewal. The main advantage of this equipment is that it can be easily adapted to needs. In addition, as the molten polymer molten polymer settles on the walls, venting problems are eliminated.

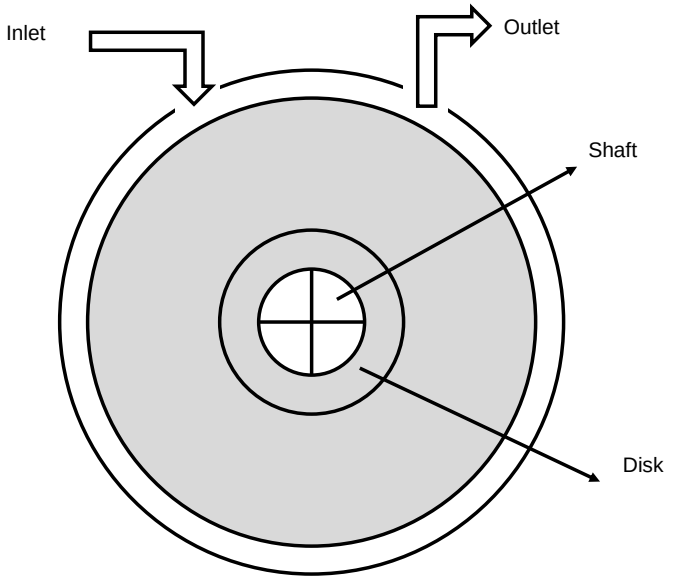

Figure 2.10: Schematic of a rotating disk devolatilizer. Adapted with permission from [18]. Copyright 2019 American Chemical Society.

A wide range of polymers, such as polycarbonates, polyesters, polyamides, or thermoplastics, can be purified with this technology. Wenzel et al. [62] described the purification of oxymethylene-based polymers using the following conditions: 160-220°C in the first and stabilization stage and 160-190°C in the second stage. The pressure ranged from 1.33×10^{-5} to 0.04 MPa in the first stage, from 0.08 to 0.13 MPa during the stabilization stage, and from 1.3×10^{-5} to 0.013 MPa in the second stage. The purification process lasted between 10 and 120 s to achieve a final VOC concentration of less than 150 ppm.

2.4 Materials and Methods

2.4.1 Materials Data

All experiments were performed with silicone oil and oxygen to obtain a volatile-polymer solution. The silicon oil (PSF-10,000cSt, Clearco Products Co., Inc.) has a viscosity of 10 Pa · s. Thermodynamics and kinetic data of oxygen in silicon oil are available in literature [13], [63], the reported solubility of oxygen in silicon oil at 25°C is 0.22 $cm^3(STP)/cm^3 \cdot atm$, whereas the diffusivity of oxygen in silicon oil at 25°C is about 2×10^{-5} cm^2/s, this is exactly the same order of magnitude as the diffusivity of solvents in commercial polymers, within the typical industrial temperature range of 200 to 250°C [64].

2.4.2 Experimental Setup

Figure 2.11 shows a schematic of the devolatilization setup, which operates at 25°C. The volatile-free silicon oil is pumped from a pressurized tank towards the devolatilizer, by a gear pump (mzr-7245, HNP Mikrosysteme GmbH). Oxygen is then injected directly into the polymer, gas flow rate is controlled with a mass flow controller (F-201CV, Bronkhorst GmbH). In order to enhance oxygen dissolution, a 20 elements static mixer (SMX, Sulzer Chemtech) [65] has been placed right after the gas injection. At first, dissolution is checked through a sight window, being certain that there are no bubbles left in the liquid.

The polymeric solution enters vacuum vessel through a capillary, specifically designed to obtain a certain pressure in the line. The vessel is made of transparent polycarbonate, to allow detailed observation of the separation process, and it is kept under vacuum by a vacuum pump (VP18 PLUS, LabTech). Gas liquid separation starts at the capillary exit from which the solution is free to fall inside the low-pressure vessel.

The devolatilized polymer is then conveyed in a tank under the vessel, where there is still vacuum. The vessel was designed to allow the insertion of an obstacle at the bottom, with the aim of slowing down the fluid fall and, so, tuning the residence time inside the vessel. The polymer accumulates on the obstacle until a certain height is reached, depending on obstacle design Figure 2.12. The fluid accumulates in this section, until

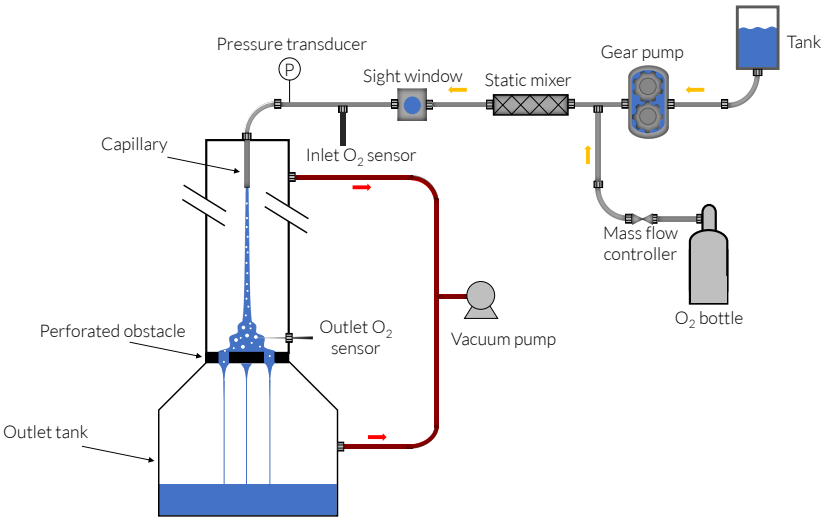

Figure 2.11: Schematic representation of experimental setup

a certain height is reached, depending on obstacle design. The devolatilized polymer is then conveyed in a tank under the vessel, where there is still vacuum.

Oxygen concentration in the silicone oil is measured with amperometric sensors before the inlet and at the end of the vessel, in a position exactly above the perforated obstacle, whether the obstacle is present or not. These Clark-type probes [66] (OX-NP 200 μ, Unisense A/S, Denmark) are very accurate and thin, and they show insignificant oxygen consumption over time, assuring precise and consistent measurements. This kind of sensors are capable of measuring O_2 partial pressure and concentration, if they are exposed to the gas or liquid phase respectively. The detection limit of these sensors is in the order of 0.1 ppm, far beyond the measurement requirements for these experiments. The calibration procedure of these sensors consists of measuring the signal at two known O_2 concentration (e.g. 0 ppm and O_2 equilibrium concentration at room conditions), since the signal is linearly dependent on the O_2 concentration.

Figure 2.12: Typical experiment with perforated obstacle configuration (2.12a), and without obstacle (2.12b). In both cases the sensor is inserted from the right.

2.4.3 Melt Spreading Surface Design

In this work, two 3D printed structures, showed in Figure 2.13, have been adopted to improve the separation efficiency. Both structures have a circular outer edge of 44 mm diameter, that fits the vessel column where devolatilization occurs. These obstacles are positioned at the bottom of the vessel column, at a distance of 320 mm from the end of the capillary.

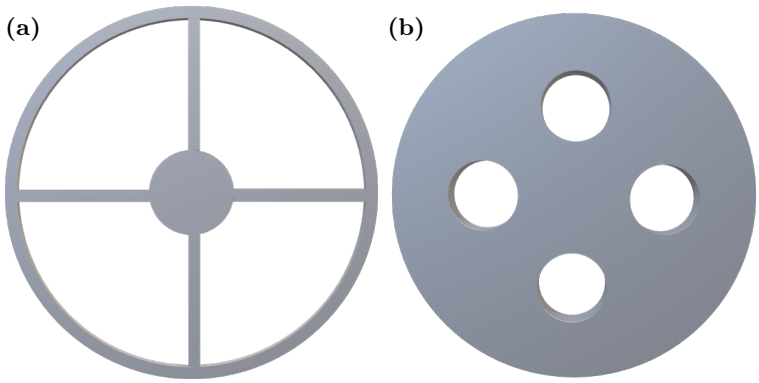

Figure 2.13: Schematic of 3D printed structures: (2.13a) Melt spreading obstacle. (2.13b) Perforated obstacle.

The melt spreading obstacle showed in Figure 2.13a is a obstacle of 1 mm thickness, with a small centered obstacle of 10 mm diameter, held by four arms, thus the resulting open fraction of 0.76, the perforated obstacle shown in Figure 2.13b is of 4 mm thickness, has four equally spaced holes of 7.5 mm diameter, resulting in an open fraction of 0.12.

2.4.4 Experimental Procedure

The silicone oil at equilibrium with atmospheric pressure and at room temperature is loaded in the tank. The gear pump and the vacuum pump are started, then the pressure, P, increases until a steady state value. Once this state is reached, the gas is injected. When the inlet oxygen concentration $C_{O_2,in}$ reaches a steady value, the data acquisition begins. The first acquisition is made to measure the partial pressure of oxygen P_{O_2}, and therefore its concentration, in the vessel gas phase, with the sensor in contact with the gas phase. P_{O_2} could be slightly different from the total pressure P because of a small percentage of nitrogen. The corresponding O_2 concentration is the equilibrium concentration fraction $C_{O_2,e}$ for a single experiment. After that, the outlet oxygen concentration $C_{O_2,out}$ is measured, by inserting the sensor in the liquid phase. The relationship between oxygen concentration C_{O_2} and its mass fraction ω_{O_2} is the following:

$$\omega_{O_2} = \frac{M_w C_{O_2}}{\rho_l} \tag{2.20}$$

where M_w is the molecular weight of oxygen and ρ_l (from material datasheet) is the liquid density.

2.4.5 Analyses and Calculations

The O_2 mass fraction is measured with the amperometric sensor, as explained in Section 2.4.2. The separation efficiency E is calculated by Equation 2.21.

$$E = \frac{\omega_{O_2,in} - \omega_{O_2,out}}{\omega_{O_2,in} - \omega_{e,O_2}} \tag{2.21}$$

here ω_{in} and ω_{out} are the inlet and outlet volatile weight fractions, respectively. The equilibrium partial pressure P_{e,O_2} is related to equilibrium mass fraction ω_{e,O_2} by Henry's law:

$$P_{e,O_2} = \bar{H}\omega_{e,O_2} \tag{2.22}$$

where $\bar{H}$ is the Henry's constant. The same correlation holds for the equilibrium pressure P_{in} corresponding to the inlet oxygen mass fraction ω_{in}.

2.4.6 Dimensionless Parameters

Bubble nucleation is a very complex phenomenon, that consists of a phase separation, whereby bubbles are generated in a homogeneous mixture. The previously defined quantities allow us to quantify the tendency of a system to generate bubbles, with the non-dimensional superheat Σ, defined as follows [67]:

$$\Sigma = \frac{P_{in}}{P_{e,O_2}} - 1 \tag{2.23}$$

Supersaturation is achieved when the temperature of the system is in-

creased or its pressure is decreased, resulting in $\Sigma > 0$. Apart from the supersaturation, there are other parameters which can influence bubble nucleation, such as the shear rate and shear stress. As reported in previous works [68–70] the nucleation rate depends logarithmically on the shear rate. Hence, this is certainly an aspect to take into account for the analysis of the results.

Another crucial stage in the devolatilization process is the bubble growth in the polymer. This topic is widely addressed in literature [46, 71]. Essentially the growth of a bubble within a polymer is controlled by mass transfer and viscous forces. Given this, it is worth mentioning some studies that have focused on the effect of shear rate and pipe confinement on the development of a bubble [72, 73].

It was found that the growth rate of a slender bubble increases as the shear rate increases. This is due to a deformation of the bubble increasing the specific area for mass transfer. Furthermore, it turns out that the growth rate of a bubble increases due to the confinement experienced by the bubble. In the experimental setup used for the present work, bubble nucleation is designed to start in the capillary, where the fluid reaches a saturated condition. Figure 2.14a shows a qualitative pressure drop profile in the capillary, the position at which the solution reaches saturated condition is defined as L_n, while the capillary length is L_c, and it moves towards the end of the capillary as P_{in} increases, as shown in Figure 2.14b.

The previous considerations about the effect of shear and confinement on bubble nucleation and growth, lead us to consider the residence time of the fluid in the capillary as a parameter that affects the foam development. In fact, if L_n is close to L_c, nucleation and growth will occur primarily outside the capillary, with no influence of shear and confinement. In order to consider this effect, let us define a non-dimensional "nucleation length" $\hat{L}$ which is the portion of the capillary involved in the foam formation and development. The influence of superheat and nucleation length will be discussed in Section 2.5.3.

$$\hat{L} = \frac{L_c - L_n}{L_c} \tag{2.24}$$

A further consideration can be done about the foam height with the perforated obstacle configuration. Defining the height of non-foamed polymer

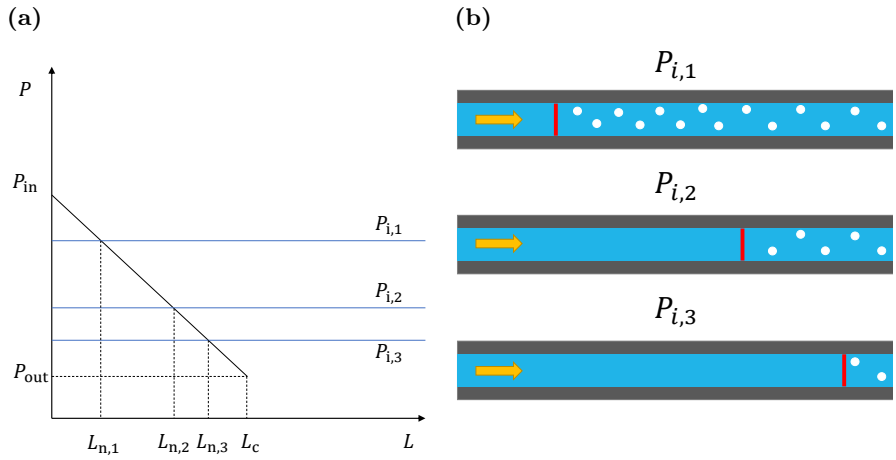

Figure 2.14: (2.14a) Qualitative representation of different nucleation points at different inlet concentrations. Blue lines represent the pressure in equilibrium with the inlet oxygen concentration and the vertical dashed lines are in correspondence of the nucleation position along the capillary, (2.14b) Schematic of the advancement of nucleation point for decreasing inlet oxygen vapor pressure.

on the perforated obstacle for a fixed flow rate as H_0, it is possible to obtain a good estimate of it with the Darcy-Weisbach equation [74]. The effective height over the obstacle is usually higher than the predicted one, because of the lower density of the foam, in order to compare the predicted height H_0 and the measured one H, one could define a non-dimensional height $\hat{H}$ as follows.

$$\hat{H} = \frac{H}{H_0} \tag{2.25}$$

Similarly, the vacuum pressure in the vessel can be scaled by the atmospheric pressure P_0 as follows:

$$\hat{P} = \frac{P}{P_0} \tag{2.26}$$

2.5 Results and Discussion

2.5.1 Effect of Fall Height

The need to improve the devolatilization process derives from the low removal efficiency of simple falling strand (FS), under certain conditions. Figure 2.15 shows the dependence of the devolatilization efficiency with respect to the initial O_2 content, for two different fall heights at four different vacuum pressures P_v. There is ample room of improvement at the lowest ω_{in}, for which the efficiency does not exceed 0.86. On the other hand, for the vacuum pressures of 2, 5 and 10 kPa, the downstream fluid is almost at equilibrium with the gas phase, whereas the efficiency slightly decreases at 40 kPa.

The falling length effect was measured without changing the capillary and by moving the O_2 sensor vertically. As shown in Figure 2.15, reducing the fall height, to about one third of its initial value, has a negative effect on the efficiency, since oxygen has less time to diffuse out of the polymer. The increase of ω_{in} has a positive effect on the efficiency, regardless of the fall height and of the vacuum pressure, as also confirmed by [16]. The reason for this behavior is that bubble nucleation increases as a function superheat [67], causing a significant increase in the surface area.

2.5.2 Effect of Obstacles

As mentioned above, the simple falling of the polymer strand is insufficient to remove the volatile completely. A 3D-printed surface is positioned at the bottom of the vessel at 330 mm from the capillary to enhance the removal efficiency. The accumulation of polymer on this surface increases polymer residence time under vacuum conditions and enhances gas entrainment in the polymer, further increasing the active surface for mass transfer[75],[76].

As shown in Figure 2.16, both obstacles enhance the volatile removal. Considering the melt spreading obstacle (MSO) (Figure 2.13a), the polymer falls on the central surface, enhancing gas entrainment and slowing the polymer fall by just a few seconds. With the perforated obstacle (PO) (Figure 2.13b), the fluid accumulates on the obstacle, and a foam column is generated.

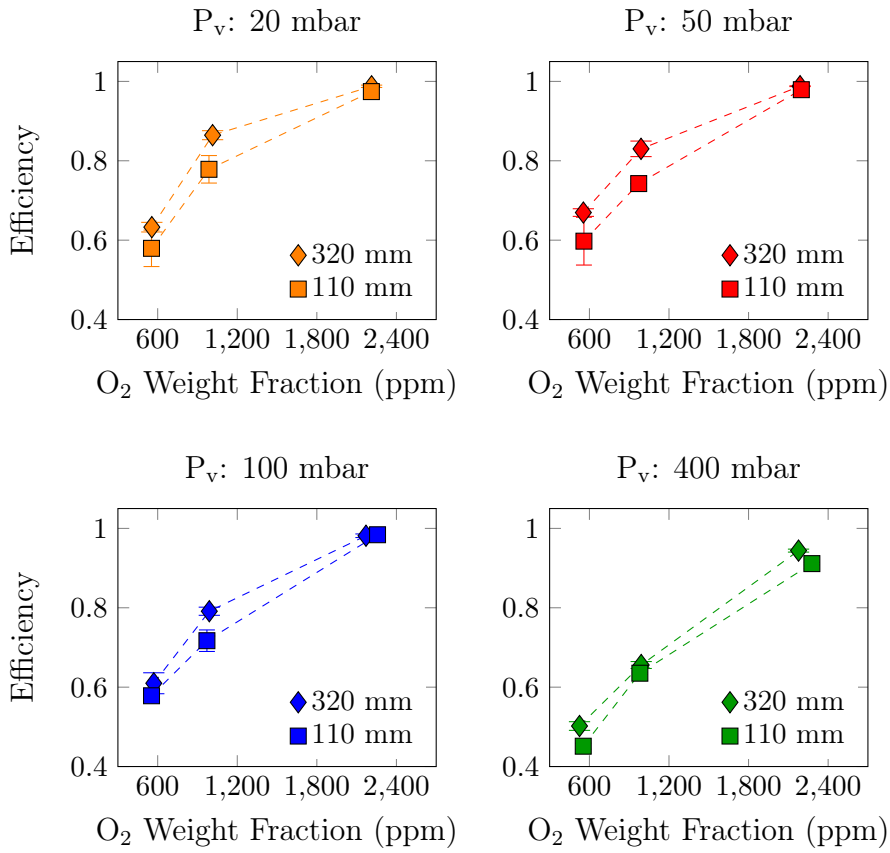

Figure 2.15: Devolatilization efficiency as a function of inlet O_2 weight fraction at two different falling lengths.

The presence of the obstacle is not beneficial at the highest weight fraction of O_2 input since complete devolatilization is already achieved in the falling filament. It is worth noting that, at the highest vacuum pressure P_v =40 kPa, the effect of the obstacle at the lowest O_2 weight fraction is minimal compared to other vacuum pressures. The reason is that for such low O_2 content and high vacuum pressure, nucleation and bubble growth are extremely poor, significantly reducing the active surface area for mass transfer. On average, the presence of the obstacle produces a 13% increase in efficiency.

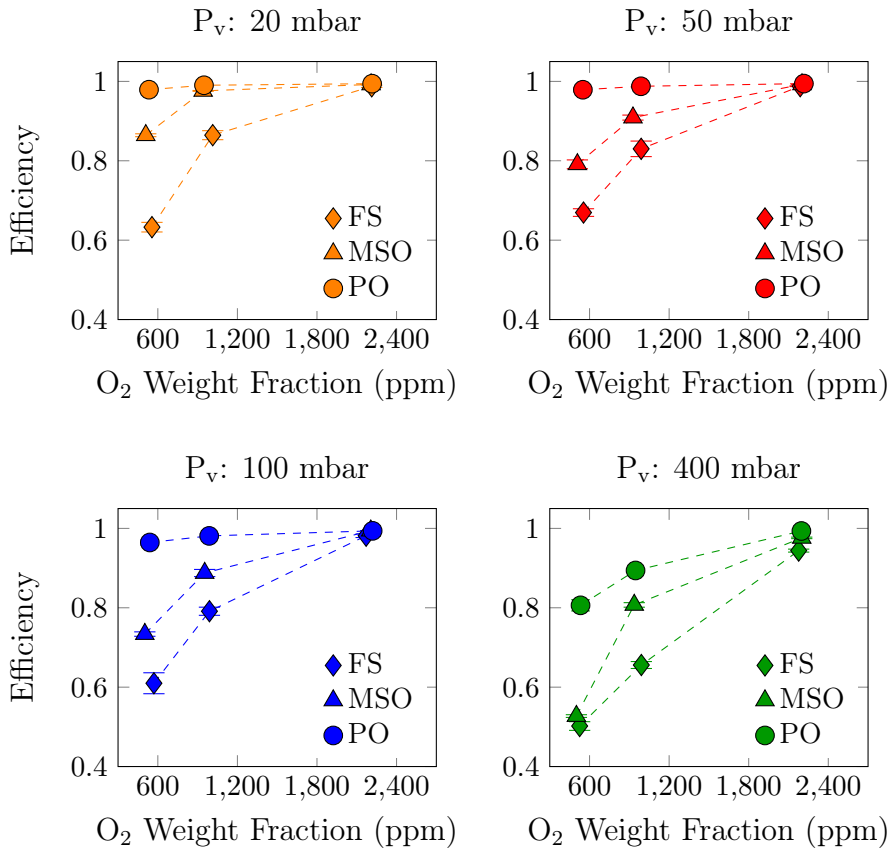

Figure 2.16: Effect of obstacle design on devolatilization efficiency. Data for FS configuration, with a falling length of 320 mm, are reported for comparison.

The data provided suggest that the design of the obstacle has an impact on devolatilization performance. The perforated obstacle is more advantageous than the one that diffuses the melt. The former increases the residence time of the foam more than the latter, improving O_2 removal. This is confirmed by the foam height above the obstacles, which is consistently below 10 mm with the melt spreading obstacle, while it is more significant with the other.

The freshly foamed fluid accumulates on the perforated obstacle, forming a fluid column. The fluid height above the perforated obstacle de-

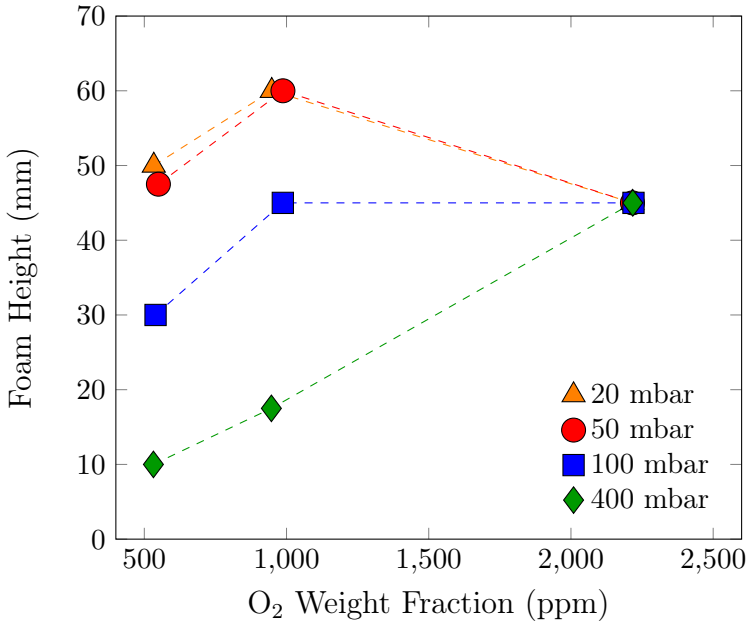

Figure 2.17: Height of foam as a function of inlet O_2 weight fraction, for the perforated obstacle configuration, at different vacuum pressures.

pends mainly on the inlet O_2 content and vacuum pressure, as shown in Figure 2.17. The foam height increases with volatile inlet content at the lowest values for a given vacuum pressure while it decreases to a constant value at the highest O_2 fraction. This behavior is due to the complete removal of volatiles within the falling filament, which occurs at the highest O_2 content, causing less significant foam in the fluid column after the filament.

The previous consideration confirms that the presence of the obstacles is not beneficial at the highest inlet volatile content since a complete devolatilization is already achieved in the falling strand. Nevertheless, for the two lowest O_2 fractions, the efficiency is considerably increased by the presence of obstacles.

2.5.3 Data Scaling

The residence time of the polymer in the capillary is approximately 0.8 s, and a bubble under shear conditions grows with an average rate of about 10 µm/ms just in the first 20 ms after nucleation, resulting in an appreciable increase of size along the capillary [72, 73]. In addition, bubble nucleation strongly depends on the shear rate which is present in the capillary [68–70]. The longer the residence time of the mixture in the capillary, the more the bubbles nucleate and grow due to the combined effect of shear rate and confinement, with a significant increase in the specific surface area for mass transfer and, therefore, removal efficiency.

The nucleation length is a relevant parameter for determining the devolatilization efficiency as shown in Figure 2.18 where the efficiency is plotted as a function of non-dimensional super-heat and nucleation length. An increase in *Sigma* means an increase in the driving force for separation that results in improved efficiency. On the other hand, the quadratic dependence of the efficiency on the non-dimensional nucleation length suggests that multiple phenomena contribute to the removal of O_2. As mentioned earlier, these two phenomena can be identified as shear stress and confined flow conditions.

The trend of the experimental data is well described by the chosen parameters. The measured efficiency values collapse on two different curves, each of these is representative of an experimental configuration. The lower curve is correlated to the pure falling strand configuration, the upper one represents the perforated obstacle configuration. The displacement among these curves represents the difference in residence time of the polymer in the vessel in the three cases, which is lower for the FS configuration, and increases with MSO and Po configurations.

A similar scaling is given for the foam height configuration with the perforated obstacle. The scaled data are shown in Figure 2.19 appear to increase logarithmically with the nondimensional parameter $\Sigma\hat{L}^2/\hat{P}$ confirming how the foam height depends on the initial and final pressure conditions and the nucleation length in the capillary. Of all the height values shown in Figure 2.17, only the data at 500 and 100 ppm initial weight fraction of O_2 were used for scaling. The foam height at 2000 ppm is not representative of the removal efficiency since, under these conditions, an almost complete removal of O_2 was completed before the foam accumu-

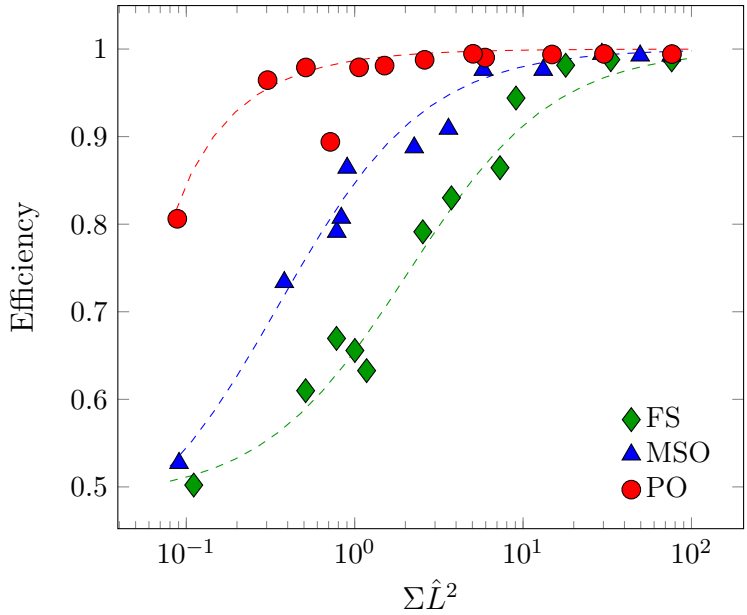

Figure 2.18: Devolatilization efficiency as a function of non-dimensional superheat and nucleation length for different DV configurations

lated on the obstacle (Figure 2.15).

2.6 Conclusions

A new small scale polymer devolatilizer, for measuring volatile removal efficiency has been presented with demonstrations of its flexibility. This apparatus provides the possibility to easily vary different operating conditions, interchange its components and accurately measure process efficiency in-line, all of which are not simply accessible in a pilot scale static devolatilizer. The devolatilizer was operated with a solution of PDMS and O_2, as a model mixture to compare to those used in industrial processes.

Observations from the devolatilization experiments showed that the process efficiency is directly related to the super-heat and to bubble nucleation position inside the capillary, giving more insights on how bubble nucleation and consequently foam interfacial area generated are two aspects

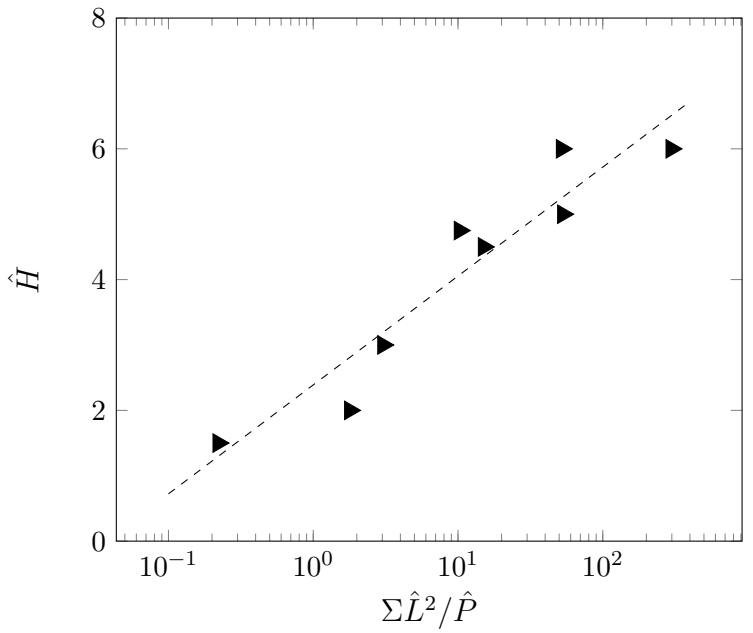

Figure 2.19: Non-dimensional height of foam column as a function of non-dimensional superheat, nucleation length and total pressure.

of major importance for process design. The provided scaling revealed a more than linear dependence of the efficiency on the non-dimensional nucleation length. This finding suggests that the effects contributing to the desorption of O_2 from the polymer may be multiple. Confined conditions and effect of shear enhance bubble nucleation and growth significantly increasing interfacial area for mass transfer. This knowledge could provide innovative practical solutions for devolatilizer design, with the goal of process optimization.

Although the proposed nucleation mechanism is based on falling strand devolatilization, it is reasonable to assume that some of the features observed in this study also play a role in rotational equipment. Since high shear fields characterize the rotary devolatilization equipment, bubble nucleation is expected to occur more than in the falling strand process.

We also demonstrated an increase in separation efficiency due to the presence of two different obstacles along the falling direction of the poly-

mer strand. The 3D printing technique allowed us to test obstacles with complex geometry, increasing the flexibility of the setup. The highest efficiency was achieved with the perforated obstacle, while less removal was possible with the melt spreading obstacle. Furthermore, based on the results observed so far it is plausible to assert that the findings observed in this work may be of great interest for larger scale static devolatilizers design.

In addition, the results observed in this work and the scaling provided may be of great interest for designing large-scale static devolatilizers and improving the accuracy of theoretical models. The link between devolatilization efficiency and foam height was also presented, providing additional information of practical interest for industrial applications.

Chapter 3

Modelling Sorption Thermodynamics and Mass Transport of n-Hexane in a Propylene-Ethylene Elastomer

3.1 Introduction

The advancements in metallocene catalyst technology have accelerated the growth and development of polyolefin elastomers (POE) with a finely controlled structure-property characteristics [77]. These elastomers, belonging to the broader class of thermoplastic elastomers (TPE), have increased in use due to their superior mechanical and thermal properties, versatility, and recyclability [78]. Solution polymerization is one of the critical processes to produce polypropylene (PP) based elastomers. The production of propylene-based polyolefins with various properties has continuously grown since the discovery of Ziegler–Natta catalysts, boosted by the rapid development of catalyst technology combined with polymerization process innovation. Among them, a relevant class is propylene-ethylene copolymers, semi-crystalline performance polymers with tunable amorphous content and mechanical and optical properties. They are economical, recyclable, and can be designed for a specific application (e.g., adhesives, packaging).

Thermodynamics of mixtures of POE and alkane/alkenes hydrocarbon systems are of enormous interest for many industrial applications, like designing polymerization processes, polymer purification technology, and optimizing batch or continuous polymer foaming processes. For instance, the role of solvent concentration in the mentioned processes is fundamental for the following operations:

- Polymerization: The monomer concentration, which can be dissolved in the polymer, determines the concentration at the active site, affecting the polymerization rate and molecular weight distribution [79].
- Polymer foaming: The blowing agent concentration, which can be solubilized in the polymer, affects the final expansion ratio, the cellular morphology, and the final foamed shape [80].
- Separation technology: the maximum degree of separation, i.e., the solvent concentration at equilibrium that may be obtained for a given system, is the most critical parameter of interest to optimize the equipment design while controlling the strict levels of volatile organic compounds (VOCs) in the final product [81].

From a practical viewpoint, the accurate knowledge of the thermodynamics of such polymer-solvent mixtures can be highly beneficial to optimally model and design polymer plants, control stream compositions going into upstream units, and, importantly, abide the strict measures on final product quality, thereby creating a significant industrial impact. Such analysis can be extended to systems with similar characteristics, providing support to ongoing research and contributing to innovation in the field of polymer processing.

Understanding thermodynamics of mixtures of long-chain molecules with short, nonpolar hydrocarbon molecules require sophisticated experiments to provide high quality data and reliable thermodynamic models to explain their complex non-ideal behavior. Sorption thermodynamics has been the center of research for many decades, aimed at describing phase equilibria of polyolefins with several small molecules involved in different polymer processing applications.

Even though several sorption studies of multiple gases in polymers are mentioned inthe literature (e.g., butane in PET, xylene/nonane in

Polystyrene, N2/CO2 in PP, non-polar organic solvents with Poly-isobutylene, PLA) [82], in the case of POE thermodynamic studies are rare. In effect, most of the experimental results and theoretical approaches reported in the literature for POE are restricted to the study of the solubility and transport of gases [83] or to shallow polymer content [81] or at temperatures below the polymer melting temperature [80], while investigations focused on the sorption of vapors, particularly vapors of alkanes are scarce [84]. The lack of reliable thermodynamics data for the POE/alkane system at high polymer content and temperature makes the optimization of the aforementioned industrial processes and the validation of models is complex.

Elaboration of models for the thermodynamics of polymer-containing mixtures, adequate for system description over a wide range of pressure and temperature conditions is still an active and fascinating research area. To this end, a large number of thermodynamic approaches based on statistical thermodynamics have been built rooted on the lattice models developed by Guggenheim [85] and Flory [86] for complex fluids, including polymers. A relevant example is the lattice fluid (LF) theory proposed by Sanchez and Lacombe (SL) [87–89], which was successfully adopted to deal with polymer solutions starting from 1976. Since then, other models, still based on a lattice fluid framework, have been introduced with improved performances in terms of an explicit account of the non-random distribution of molecular species and accessible volume, as well as of the presence of strong specific interactions possibly established between neighboring molecules, such as hydrogen bonding [90–94].

SL and the following improved LF approaches provide both an expression for the Equation of State (EoS) of pure fluids and mixtures, as well as for the chemical potentials of the components of a mixture and can be applied to fluids over an extended range of external conditions, encompassing liquids, vapors, gases, supercritical fluids, amorphous and glassy polymers, homogeneous as well as inhomogeneous systems, complex aqueous systems, associated polymer mixtures, rubbers, and gels. A relatively recent development in this kind is the Non-Random-Hydrogen-Bonding model (NRHB) proposed by Panayiotou et al. [93, 94], a compressible lattice fluid EoS theory that besides the mean-field interactions, also accounts for the presence of specific interactions (e.g., hydrogen bonding,

Lewis acid/Lewis base interactions) and for non-random distribution of components and free volume in pure compounds [93] and their mixtures [94].

Many research efforts have been devoted to making EoS models which accurately describe the polymer solvent phase equilibrium. An EoS can describe the pure component as well as the mixture properties. Solubility of multiple gases, like N_2, H_2, He, and CO_2, in polyolefins have been modeled with different EoSs. However, models to accurately predict equilibrium sorption thermodynamics of small chain hydrocarbon in POEs have yet to be thoroughly tested, especially in the concentrated polymer regime [82]. In addition, the model parameters for POE are not readily available.

In the present contribution, we address the case of n-hexane sorption in a commercial POE is made of isotactic propylene repeating units with random ethylene distribution, produced by ExxonMobil under the trade name Vistamaxx 8880 (V8880). The analysis of this system is helpful for correctly identifying optimal conditions in processing this polymer. Sorption isotherms of n-hexane vapor at several temperatures have been determined by gravimetry. Data were interpreted using a Non-Random Lattice Fluid (NRLF) model analogous to the NRHB model but without the terms accounting for specific interactions, which have not to be considered here given the chemical structure of the polymer (polyolefin) and the penetrant (n-hexane).

The analysis was performed at low relative pressures of n-hexane vapor since the main interest was tailoring processing conditions at low n-hexane concentration conditions. Parameters of the NRLF model for the pure components were determined by fitting with the model, respectively, the observed PVT behavior of the polymer and the density and vapor pressure data at vapor-liquid equilibrium available in the literature for n-hexane. Experimental sorption isotherms were then fitted through the NRLF model to retrieve the value of the binary interaction parameter for the V8880-n-hexane mixture. Mass transport properties were also investigated, determining the mutual diffusivity of the V8880-n-hexane system at several temperatures and concentrations experimentally. From these values, applying a model based on free-volume arguments estimated the n-hexane intradiffusion coefficient in V8880, whose dependence on temperature and mixture composition was interpreted using a semi-empirical model.

3.2 Theoretical Background

3.2.1 Modeling Sorption Thermodynamics by NRLF Approach

The evolution of classical compressible LF theories used to describe the thermodynamics of amorphous rubbery polymer–penetrant mixtures consisted in introducing modifications to the SL theory by accounting for the non-random distribution of components and accessible volume. The NRLF approach adopted here belongs to this class of models and is derived from the NRHB model [93–97] by dropping out the terms related to specific interactions. We only address the specific case of a binary system made of a polymer and a low molecular weight penetrant.

Analogously to the NRHB model, the thermodynamic behavior of a pure component is described using only three characteristic scaling parameters, i.e., $v^*_{i,sp,0}$, $\varepsilon^*_{i,h}$ and $\varepsilon^*_{i,s}$ The first one, $v^*_{i,sp,0}$ ($cm^3\times g^{-1}$), appears in the following expression [96, 98] adopted to calculate the closed-packed specific volume of component i, $v^*_{i,sp}$ ($cm^3\times g^{-1}$):

$$v^*_{i,sp} = v^*_{i,sp,0} + (T - 298.15)v^*_{sp,1} \tag{3.1}$$

where $v^*_{sp,1}$ (cm^3/gK) is a constant for a given homologous series of compounds [99–105] and it is set equal to $-0.412\cdot10^{-3}$ ($cm^3\times g^{-1}\times K^{-1}$) for non-aromatic hydrocarbons, $-0.310\cdot10^{-3}$ ($cm^3\times g^{-1}\times K^{-1}$) for alcohols, $-0.240\cdot10^{-3}$ ($cm^3\times g^{-1}\times K^{-1}$) for acetates, $-0.300\cdot10^{-3}$ ($cm^3\times g^{-1}\times K^{-1}$) for water, and $-0.150\cdot10^{-3}$ ($cm^3\times g^{-1}\times K^{-1}$) for all the other fluids [104, 105]. Finally, T represents the temperature (expressed in Kelvin).

In the case of a polymeric compound, Equation 3.1 is modified so that it also takes into account for the possible pressure dependence, becoming:

$$v^*_{i,sp} = v^*_{i,sp,0} + (T - 298.15)v^*_{sp,1} - 0.135\cdot10^{-3}P \tag{3.2}$$

where P represents the pressure (expressed in MPa in this equation).

The other two energy parameters, $\varepsilon^*_{i,h}$ ($J\times mol^{-1}\times K^{-1}$) and $\varepsilon^*_{i,s}$ ($J\times mol^{-1}\times K^{-1}$), which represent, respectively, the enthalpic and entropic terms, are needed to calculate the average mean field interaction energy

per molecule of component i, ε_i^* , that is expressed as [91, 93]:

$$\varepsilon_i^* = \varepsilon_{i,h}^* + (T - 298.15)\varepsilon_{i,s}^* \tag{3.3}$$

Notably, the volume occupied by a cell of a molecule of species i, v_i^*, is assumed to take the universal value of $9.75/N_{AV}$ ($\mathrm{cm}^3\times$ $\mathrm{molecule}^{-1}$), with N_{AV} representing the Avogadro number. Consistently, in the case of a mixture, the molar volume of lattice cells, indicated as v^*, takes the same value, independently of concentration. This is a relevant point since the assumption of a constant universal value for v_i^* and v^* guarantees the thermodynamic consistency of the thermodynamic model [98], which is, instead, not granted in other lattice fluid theories (see for example the case of the SL model, as discussed in [98]). From this set of parameters, the number of lattice cells occupied by one molecule of species i, b_i, can be calculated [94, 98] using the following expression:

$$b_i = \frac{M_{w,i} v_{i,sp}^*}{v_i^*} \tag{3.4}$$

where $M_{w,i}$ is the molecular weight of component i.

The values of the three model parameters for the pure component i, i.e., $v_{i,sp,0}^*$, $\varepsilon_{i,h}^*$ and $\varepsilon_{i,s}^*$, are generally retrieved from vapor pressure and volumetric properties in the case of a pure component with low molecular weight. In contrast, in the case of a polymer, they are retrieved from PVT data in the melt state. An additive parameter is the so-called molecular shape factor, s_i, defined as the ratio between the number of external lattice contacts per molecule of components i, q_i, and b_i. This parameter can be either evaluated using the UNIFAC group contribution model [106] or can be retrieved from fitting procedures of experimental data, along with the three characteristics scaling parameters.

The relevant model equations (i.e., the expression of Gibbs energy and volumetric EoS) for pure components are expressed in terms of dimensionless reduced variables, i.e., reduced temperature $\widetilde{T}_i$, reduced pressure $\widetilde{P}_i$, and reduced density $\widetilde{\rho}_i$:

$$\widetilde{T}_i = \frac{T}{T_i^*}; \quad \widetilde{P}_i = \frac{P}{P_i^*}; \quad \widetilde{\rho}_i = \frac{\rho}{\rho_i^*}; \tag{3.5}$$

The corresponding normalizing factors for the temperature T, pressure P, and density r, i.e., T^*, P^*, and r^*, are interrelated via the following expressions [93]:

$$\rho_i^* = \frac{M_{w,i}}{b_i v^*} \tag{3.6}$$

$$\varepsilon_i^* = \bar{R} T_i^* = P_i^* v^* \tag{3.7}$$

where $\bar{R}$ is universal gas constant.

In the following, the quantities referred to the low molecular weight penetrant and to the polymer are indicated with the subscripts "1" and "2" respectively. For the case of a binary mixture of components "1" and "2", the average mean field interaction energy per molecule, ε^*, is obtained through the following mixing rule:

$$\varepsilon^* = \theta_1^2 \varepsilon_1^* + 2\theta_1\theta_2\varepsilon_{12}^* + \theta_2^2 \varepsilon_2^* \tag{3.8}$$

where θ_1 and θ_2 are the so-called surface contact fractions [94] which depend on concentration and

$$\varepsilon_{12}^* = (1 - k_{12})\sqrt{\varepsilon_1^* \varepsilon_2^*} \tag{3.9}$$

where the binary interaction parameter, k_{12}, measures the departure of mean field interaction energy from the value provided by the geometric mixing rule. Analogously, in a binary mixture, parameters b and q are calculated using the following simple mixing rules:

$$b = b_1 x_1 + b_2 x_2 \tag{3.10}$$

$$q = q_1 x_1 + q_2 x_2 \tag{3.11}$$

and so

$$s = \frac{q}{b} \tag{3.12}$$

where x_i is the molar fraction of component i.

As for pure components, also for a binary mixture, dimensionless reduced variables, i.e., reduced temperature $\widetilde{T}$, reduced pressure $\widetilde{P}$, and

reduced density $\widetilde{\rho}$ [94], can be defined as follows:

$$\widetilde{T} = \frac{T}{T^*} = \frac{\bar{R}T}{\varepsilon^*} \tag{3.13}$$

$$\widetilde{P} = \frac{P}{P^*} = \frac{Pv^*}{\bar{R}T^*} \tag{3.14}$$

$$\widetilde{\rho} = \frac{1}{\widetilde{v}} = \frac{Nbv^*}{V} \tag{3.15}$$

where V is the volume of the mixture and N is the total number of molecules in the mixture. It is worth recalling that, also in the case of a mixture, v^* is assumed to take the universal value of $9.75/N_{AV}$ ($\mathrm{cm}^3\times$ $\mathrm{molecule}^{-1}$).

The NRLF model provides the dimensionless expressions for the EoS of both the pure components and their mixtures that take the same form in terms of reduced variables [93, 94]:

$$\widetilde{P} + \widetilde{T}\left[\ln(1-\widetilde{\rho}) - \widetilde{\rho}\left(\sum_i \varphi_i \frac{l_i}{b_i}\right) - \frac{z}{2}\ln\left(1 - \widetilde{\rho} + \frac{q}{b}\widetilde{\rho}\right) + \frac{z}{2}\ln\Gamma_{00}\right] = 0 \tag{3.16}$$

where $l_i = (z/2)(b_i - q_i) - (b_i - 1)$ and z is the coordination number of the lattice in which the molecules are assumed to be arranged, φ_i represents the "close-packed" volumetric fraction of species i, and q, defined by Equation 3.11, represents the average number of lattice contacts per molecule in the mixture. In the NRLF model, the state variables G_{ij} represent the multiplicative corrective factors accounting for the non-randomness of contacts among molecular sites of species j and molecular sites of species i within the lattice ($i, j = 0, 1, 2$; in particular, an index equal to 0 stands for the empty cells of the lattice). Their values can be obtained by solving a set of equations obtained by minimizing Gibbs free energy as a function of the number of different kinds of lattice fluid contacts and by imposing material balance expressions for the lattice fluid contacts [93, 94]. In particular, Γ_{00} accounts for non-random distribution of free volume.

Occurrence of phase equilibrium between a binary polymer–penetrant mixture and the pure penetrant in a vapor or liquid state implies the equality of the chemical potentials of the penetrant in the two coexisting phases:

$$\mu_1^V = \mu_1^P \tag{3.17}$$

where μ_1^V represents the molar chemical potential of the penetrant in the pure vapor-liquid phase, while μ_1^P represents that in the polymer–penetrant mixture.

In the case of high molecular weight polymers, as is the case at hand, it is assumed that macromolecules are insoluble in the pure penetrant vapor phase in contact with it. As a consequence, no expression equating the chemical potentials of the polymer in the two phases at equilibrium is imposed, and only Equation 3.17 rules the phase equilibrium. The expression of the chemical potential of the penetrant within the polymer–penetrant phase takes the following dimensionless form [94]:

$$\begin{aligned}\frac{\mu_1^P}{RT} = &\ln\left(\frac{\varphi_1}{\omega_1 b_1}\right) - b_1 \sum_{j=1}^{2} \frac{\varphi_j l_j}{b_j} + \ln\widetilde{\rho} + b_1\,(\widetilde{v}-1)\ln\left(1-\widetilde{\rho}\right) - \\ &\frac{z}{2} b_1 \left(\widetilde{v} - 1 + \frac{q_1}{b_1}\right) \ln\left(1 - \widetilde{\rho} + \frac{q}{b}\widetilde{\rho}\right) + \\ &\frac{z q_1}{2}\left[\ln\Gamma_{11} + \frac{b_1}{q_1}(\widetilde{v}-1)\ln\Gamma_{00}\right] + b_1 \frac{\widetilde{P}\widetilde{v}}{\widetilde{T}} - \frac{q_1}{\widetilde{T}}\end{aligned} \tag{3.18}$$

where R represents the universal constant of gases and ω_i represents a characteristic quantity that accounts for the flexibility and symmetry of molecule of kind i, and it is defined in refs. [92, 93]. This expression must be coupled with the EoS reported before (Equation 3.16). The expressions of the EoS and the chemical potential for pure penetrant in the vapor or liquid state can be obtained respectively from Equation 3.16 and Equation 3.18 by setting $\varphi_1 = 1$, and the number of components in the summation is equal to 1.

The NRLF model described above is suitable for dealing with the sorption thermodynamics of low molecular weight penetrants in amorphous rubbery polymers. This theoretical the approach has been considered appropriate for the interpretation of sorption isotherms of n-hexane in V8880

since tests have been performed at a temperature of 115 °C and higher, at which the polymer can be safely assumed to be amorphous, given the value of the melting temperature of the neat polymer, 97 °C, and of the fact that absorbed n-hexane is expected to promote a decrease of the melting temperature below this value [86].

3.2.2 Modeling Diffusive Mass Transport of n-Hexane

The so-called Fickian constitutive law generally rules the mass transport of low molecular weight compounds in rubbery polymers for diffusion (see the classical reference [107]). The diffusion of gases in rubbery polymers (e.g., oxygen in polyolefins) can be described by a mass balance. Fick's law expresses the diffusive mass flux with a binary (mutual) diffusivity independent of the penetrant concentration. This behavior is referred to as "Ideal Fickian". In the diffusion of vapors in rubbery polymers, a Fickian constitutive expression could still be used to express the mass flux.

However, a concentration-dependent binary (mutual) diffusion coefficient is generally needed. This is known as "non-Ideal Fickian" behavior. In this latter case, the dependence of diffusivity on concentration should be known to interpret sorption kinetics. A way to circumvent this difficulty is to consider sorption step experiments in which a relatively small increment of the pressure of vapor is imposed at each step so that a relatively small change in concentration occurs inside the polymer sample during the sorption experiment. In such a case, the diffusivity can be assumed to take a roughly constant value (i.e., an average value in the concentration range established within the sample during the sorption step). If the concentration of penetrant is relatively high (in general above 10%), one should also consider a mass convective contribution related to the average bulk movement of the polymer–penetrant mixture, besides the mutual diffusion contribution to the mass flux.

In the case at hand, we have interpreted sorption kinetics data assuming a non-Ideal Fickian behavior. A relatively small pressure accompanied each sorption step increase and, consequently, a small concentration. Hence, each step was interpreted using the classical solution of the differential mass balance provided by an "Ideal Fickian" constitutive expression for mass flux [108].

Since diffusivity depends on gas concentration, one expects to determine different diffusion coefficient values at each step. The determined value of binary (mutual) diffusivity can be assumed to be associated with the average concentration of n-hexane present within the sample (i.e., the average between the initial and final values of concentration of the step considered). In addition, given the relatively small values of n-hexane concentration (mass fraction values <0.1, i.e., percentage <10%), no mass convection (bulk flow) contribution has been considered in the expression for n-hexane flux.

In the case of an Ideal Fickian behavior, experimental sorption kinetics at each pressure step can be expressed as the diffusion of a penetrant in a plane sheet at a uniform initial internal concentration of penetrant and uniform and constant concentrations of the penetrant at the sample surface, by [108]:

$$\frac{M_t}{M_\infty} = 1 - \sum_{n=0}^{\infty} \frac{8}{(2n+1)^2\pi^2} \exp\left[-\frac{D(2n+1)^2\pi^2 t}{4l^2}\right] \tag{3.19}$$

where M_t denotes the total amount of diffusing substance that has entered the sheet at time t, M_∞ is the corresponding quantity after infinite time (i.e., at equilibrium) and $2l$ is the sheet thickness. It is worth noting that the mutual binary diffusion coefficient D, the fitting parameter, is characteristic of the polymer–penetrant couple considered. Given the sample geometry adopted in this investigation , we can consider that we are testing a plane sheet with only one surface exposed to the penetrant vapor, the other being adherent to the surface of the pan. Consequently, using Equation 3.19, the adopted value of $2l$ is twice the actual sheet thickness.

To gather information on the true intrinsic mobility of each component, one should consider the "intra-diffusion" coefficient of each of them. The intrinsic mobility of n-hexane in the polymer-penetrant mixture is represented by the n-hexane intra-diffusion coefficient, which is indicated as D_1 in the present context. It reflects the mobility of n-hexane molecules in the absence of any driving force, particularly the one expressed by the gradient of chemical potential. Sometimes this coefficient is also reported as the self-diffusion coefficient [32]. However, this term is more appropriate concerning the case of a pure component (i.e., self-diffusivity of pure n-hexane

or pure polymer, representing the intrinsic mobility of the molecules of a component in a pure state).

The intra-diffusion coefficient of a penetrant tends to the value of the penetrant self-diffusion coefficient as its mass fraction in the mixture tends to 1. The intra-diffusion coefficient of the polymer (indicated as D_2 in the present context) tends to the value of the polymer self-diffusion coefficient as the mass fraction of polymer in the mixture tends to 1. While the mutual diffusivity is simple to measure, the intra-diffusion (or self-diffusion) coefficient is more complex to evaluate experimentally.

There are theories, however (for example, the free volume theory of Vrentas and Duda [30, 31]), providing theoretical or semi-empirical expressions for the intra-diffusion coefficients. Then, if some simplifying assumption is taken as appropriate (i.e., the penetrant–polymer molecular friction coefficient is the geometric average of the penetrant–penetrant and polymer-polymer molecular friction coefficients [30, 31]), one can express the mutual diffusivity in terms of the intra-diffusion coefficients of the components of the mixture. In the case of low concentration of the penetrant, a further simplification can be adopted, and D can be expressed only in terms of D_1 [30, 31] (see the following Equation 3.20).

Based on these premises, we can relate the n-hexane-V8880 mutual diffusion coefficient, D, to the n-hexane intra-diffusion coefficient, D1, according to the following "free volume theory" expression [30, 31]:

$$D = \frac{D_1 \rho_1 \hat{V}_2 \rho_2}{\bar{R}T} \left(\frac{\partial \mu_1}{\partial \rho_1} \right)_{T,P} \tag{3.20}$$

where $\hat{V}_2$ represents the partial specific volume of the polymer, b_1 and b_2 represent, respectively, the density of n-hexane and polymer (expressed in grams of n-hexane or polymer per unit volume of polymer–penetrant mixture) and μ_1 represents the equilibrium molar chemical potential of n-hexane within the mixture at the given conditions. The values of $\hat{V}_2$ and of $(\partial \mu_1 / \partial \rho_1)_{T,P}$ can be evaluated numerically using the NRLF model for mixtures.

3.3 Materials and Methods

3.3.1 Materials

The investigated polymer is a commercial semicrystalline polyolefin elastomer (POE) made of isotactic propylene repeating units with random ethylene distribution. It is produced by ExxonMobil under the trade name VistamaxxTM 8880. Its physical properties, available from the data sheet provided by the producer [109], are summarized in Table 3.1, where ρ, T_g, and T_m are polymer density, glass transition temperature, and melting temperature, respectively.

A reagent-grade n-hexane with a purity $\geq$ 99% was purchased from Sigma Aldrich, Milan, Italy.

Table 3.1: Physical properties of Vistamaxx™ 8880 [109].

$\boldsymbol{\rho}$ (g/cm^3)	$\boldsymbol{T_g}$ (°C)	$\boldsymbol{T_m}$ (°C)
0.879	-22	97

3.3.2 Charaterzation of PVT Behavior

The specific volume of the V8880 elastomer, at equilibrium conditions, has been measured as a function of temperature and pressure in the following ranges: 25–200 °C, 10.0–200.0 MPa, and it was used for the determination of the NRLF model [93] parameters. The apparatus used for this purpose was a high-pressure dilatometer by GNOMIX (Gnomix Inc., Boulder, CO, USA—see the scheme of the apparatus reported in Figure 3.1). Polymer granules, ca. 1 g, were inserted in a nickel cup in the cell's sample compartment. They were subjected to isothermal tests with a pressure step increase of 10.0 MPa and with 20 s waiting time before each measurement.

Since the GNOMIX equipment determines only volume changes, a reference absolute density measurement is required at known temperature and pressure conditions. To this aim, a Helium Pycnometer (AccuPyc II

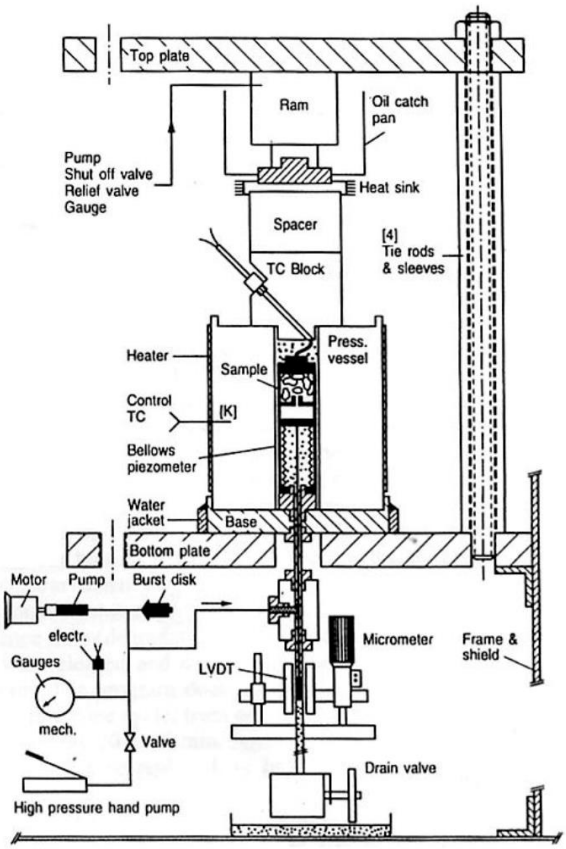

Figure 3.1: Schematic representation of GNOMIX high pressure dilatometer.

1340, Micromeritics-Alfatest, Italy) was utilized to determine the density of the polymer at T = 25 °C and P = 0.1 MPa.

Figure 3.2 shows the outcomes of the experiments performed with the dilatometer in terms of density vs. pressure at different temperatures. The PVT data are reported in the pressure range 10–200 MPa and the temperature range from 120 to 220 °C, since only data in this range have been used to retrieve the NRLF model parameters for pure V8880. Data fitting of PVT data was performed to determine the three scaling parameters of

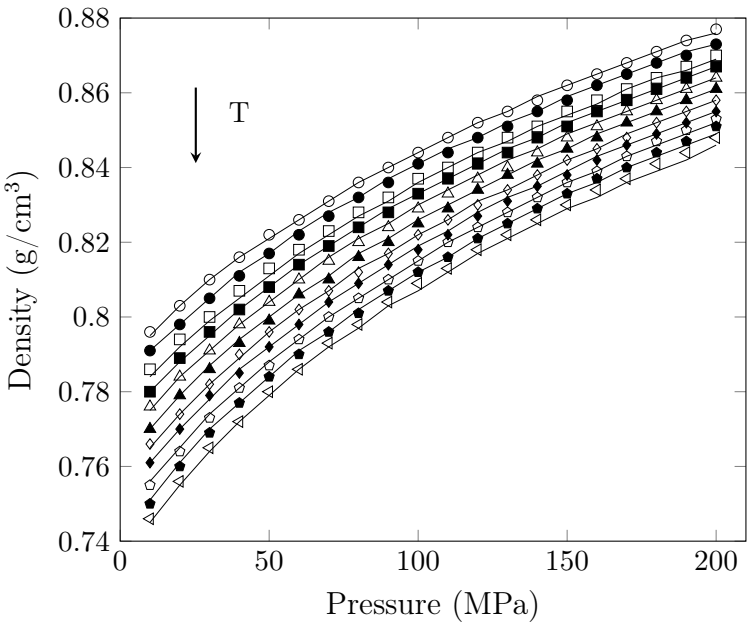

Figure 3.2: Density vs. pressure isothermal data for V8880. Lines represent the results of simultaneous best fitting of equilibrium dilatometric data using NRLF model. Temperature analyzed are, respectively, from top to bottom: 123.49 °C; 132.42 °C; 145.50 °C; 152.80 °C; 161.31 °C; 171.06 °C; 180.96 °C; 188.84 °C; 198.91 °C; 207.57 °C; 219.39 °C.

the model, along with the molecular shape factor. Data fitting results are also reported in Figure 3.2 and are discussed in Section 3.4.2.

3.3.3 Equilibrium Data for Pure n-Hexane

Vapor pressure and equilibrium density data at liquid-vapor equilibrium for n-hexane were retrieved from thermodynamics databases (available online at the NIST website: https://webbook.nist.gov/chemistry/, accessed on 2 December 2020). In Figure 3.3a are reported the vapor pressure as a function of temperature at vapor-liquid equilibrium conditions. In Figure 3.3b are reported temperature vs. equilibrium density data for the vapor phase (data on the left) and the liquid phase (data on the right) at phase equilibrium. Data fitting of these equilibrium data was performed

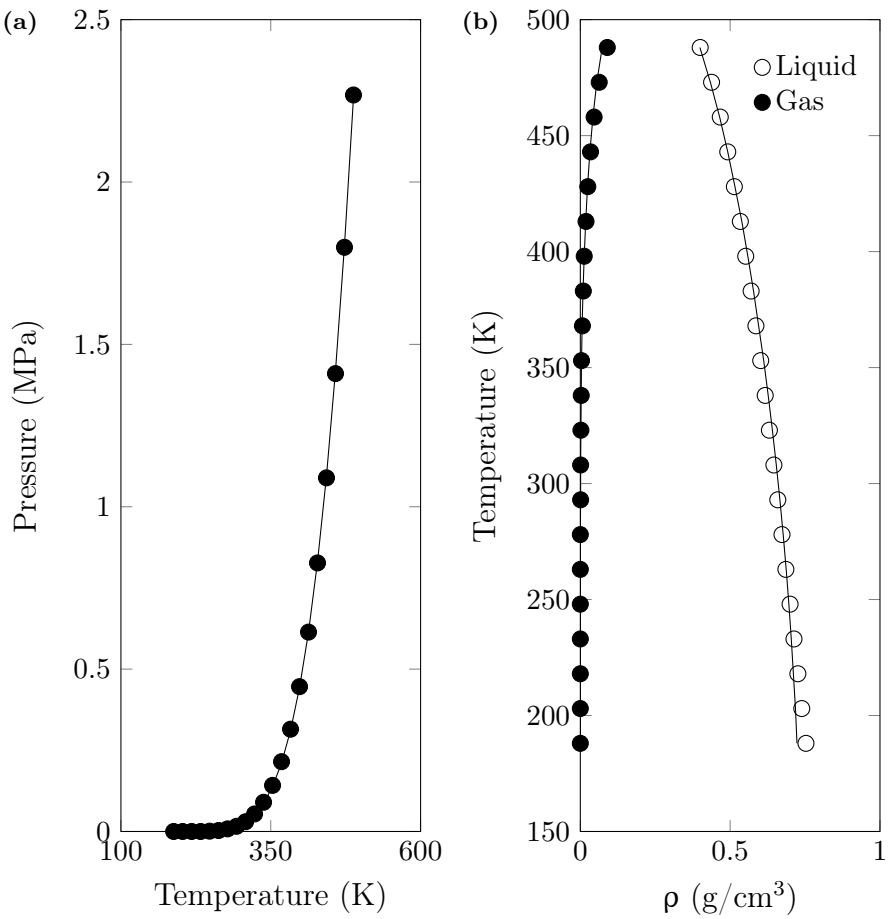

Figure 3.3: n-hexane equilibrium data: 3.3a Vapor pressure data of n-hexane as a function of temperature; 3.3b temperature vs. density data for n-hexane at vapor–liquid equilibrium. Experimental points were retrieved from https://webbook.nist.gov/chemistry/. Results of simultaneous best fitting of data by using NRLF model are reported as continuous lines.

to determine the scaling parameters of NRLF model for pure n-hexane (see continuous lines in Figure 3.3a and Figure 3.3b) as it will be discussed in SectionSection 3.4.2.

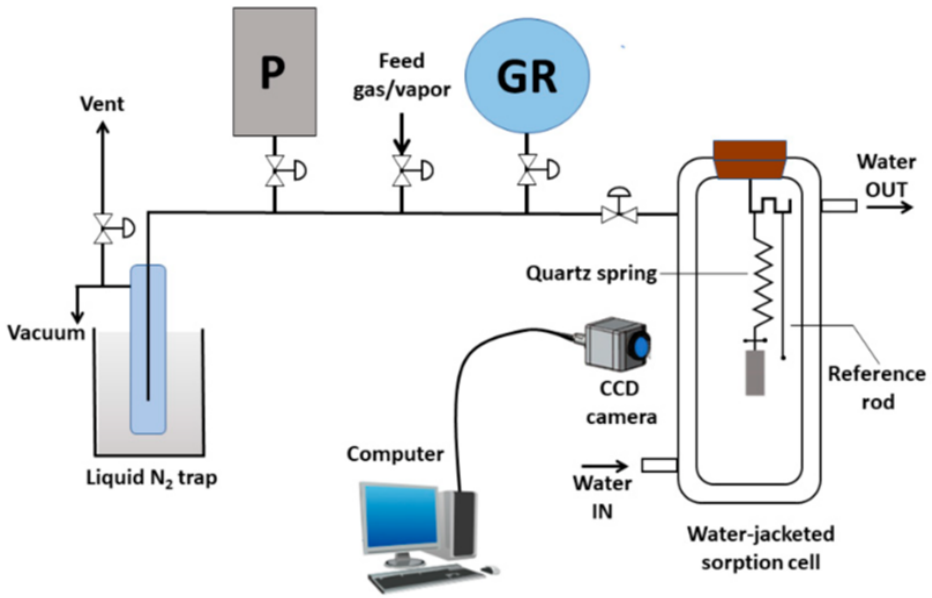

Figure 3.4: Schematic representation of a McBain quartz spring sorption apparatus. The polymer sample hangs from the quartz spring located in the sorption chamber. (P: pressure transducer; GR: gas/vapor reservoir). Reprinted with permission from [98]. Copyright 2019 Elsevier B.V.

3.3.4 Gravimetric Sorption Tests

Vapor sorption experiments of n-hexane in V8880 were performed using a controlled atmosphere McBain micro-balance (see Figure 3.4), consisting of a quartz spring made of two counter-rotating elements (Ruska Instrument Co., Houston, TX, USA) located in a jacketed thermostated glass measuring cell.

The tests have been performed according to a standard procedure described in full details in [110]. The weight increase of the polymer sample exposed to n-hexane vapor was determined from the measurement of the elongation of a quartz spring at which the sample was hung. The sample was placed in a cylindrical pan suspended to the spring's terminal hook. The thickness of the sample has been calculated from density data based on the geometrical dimensions of the adopted cylindrical sample pan.

Service lines connect the thermostated measuring cell (accuracy of temperature control of the cell environment ± 0.05 °C) to a flask, to a pressure transducer (MKS Baratron 121A, with a full-scale of 1000 mbar, a sensitivity of 0.1 Torr, an accuracy of 0.1% of the reading) to the liquid pure n-hexane reservoir, to a turbomolecular vacuum pump, and the exhaust line. The spring was calibrated at three temperatures in the range 110–140 °C to account for the possible drift of the calibration constant with temperature. The adopted spring had a nominal elongation of 400 mm for 50 mg (with a sensitivity of 1.25×10^{-4} mg/μm).

Spring elongation was continuously acquired using a traveling camera, with a microscope objective. The camera was fixed to a high accuracy motorized translation stage (V-817 by Physik Instrumente Karlsruhe, Germany) that was computer controlled, with a positioning accuracy of ± 2.5 μm. The measuring system, considering the adopted quartz spring's characteristics and the translational stage's accuracy, featured a minimum detectable weight change equal to 3.12×10^{-4} mg. The video signal from the camera was continuously acquired and stored at prescribed time intervals in a computer. The whole measuring system (camera, moving stage) was controlled using Labview® acquisition software by National Instruments, Austin, TX, USA.

Vapor sorption experiments were performed at 115, 122, 130, and 140 °C at the pressure values of n-hexane vapor reported in Table 3.2. The determination of each sorption isotherm was repeated three times. As already mentioned, in this temperature range the polymer is above its melting temperature. As an example of a typical sorption run, it is reported in Figure 3.5 the sorption step was performed from 576 mbar to 1001 mbar at 115 °C. The experiment started at the instant of time at which n-hexane vapor entered the measuring cell. The displacement of the quartz spring end (where the sample is placed inside a quartz pan) is then followed as a function of time and recorded until the sorption equilibrium is attained. A time-independent equilibrium state is assumed when the constant asymptotic value is maintained for at least twice the time needed to reach that value. In Figure 3.5, the entire experiment lasts about 5600 s, the time needed to reach the constant spring displacement being about 1800 s, and the time waited at the plateau value about 3800 s.

The increase of sample weight (corresponding to the weight of absorbed

Table 3.2: Operating pressures (mbar) at the four different temperatures investigated.

115 °C	**122 °C**	**130 °C**	**140°C**
20	80	20	201
79	254	156	597
151	536	252	1058
297	774	414	
405	1047	662	
576		1045	
1001			

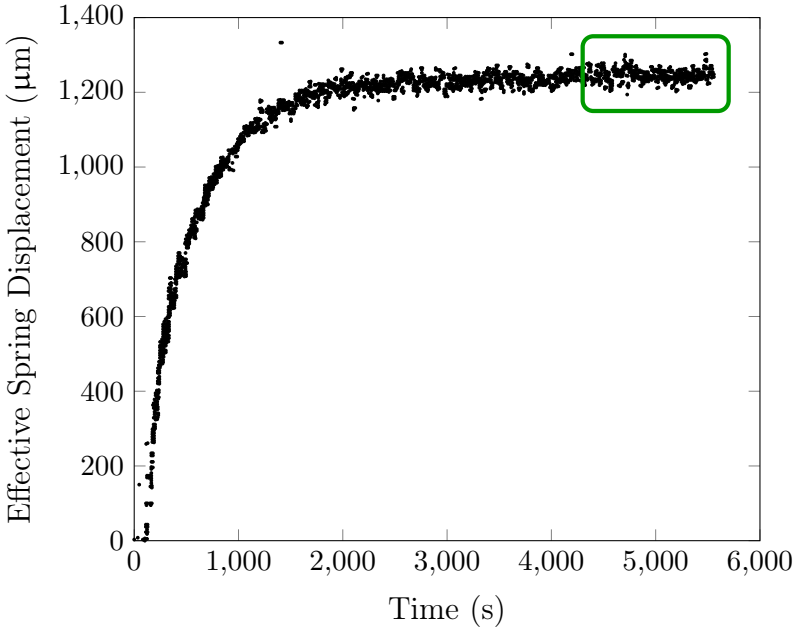

Figure 3.5: Effective spring displacement during the experiment performed from 575.6 mbar to 1001.2 mbar at 115 °C. Equilibrium data are retrieved from the final constant displacement (relevant equilibrium data are highlighted by the green rectangle).

n-hexane) was retrieved from the spring displacement by using the spring weight/displacement calibration constant. The weight increase was then transformed into mass fraction of n-hexane absorbed in the polymer-n-hexane mixture (i.e., grams of n-hexane per gram of mixture). Buoyancy effects exerted by the n-hexane vapor have been taken into account by calculating the thrust of the vapor from the weight registered using the spring balance. The thrust has been estimated, for each sorption kinetics test, by extrapolating the weight increase down to the starting time of each test. In addition, a remarkable but physically sound assumption is that no polymer is present in the vapor phase, given the vanishingly low vapor pressure of the polymer.

3.4 Results and Discussion

3.4.1 Sorption Isotherms for n-Hexane/V8880 System

Experimental sorption tests of n-hexane vapor in V8880 have been performed at 115, 122, 130, and 140 °C. At each temperature, the vapor pressure of n-hexane has been increased stepwise, collecting at each step sorption kinetics and the equilibrium sorption value. The pressure range of pure n-hexane vapor was from 0 to around 1 atm (0.1 MPa). The results in terms of equilibrium sorption isotherms are reported in Figure 3.6. Data fitting by the NRLF model for mixtures applied to the n-hexane/V8880 system is also reported and discussed in Section 3.4.3.

It is worth noting that three runs of "step-increase of pressure" experiments have been performed at each temperature. After a run made of several increases of the pressure of n-hexane vapor, a total desorption on n-hexane was performed, followed by another set of steps of increase of pressure. The average value of these measurements is reported at each pressure. As expected for rubbery polymer–penetrant mixtures, no hysteresis effect was noticed, and all the data of the three runs performed at each temperature accommodated on a single isotherm.

Very few data are available in the literature to be compared with our results for sorption isotherms of n-hexane in polymer systems similar to the one under investigation. In particular, Francouer [111] reports results for n-hexane sorption in EPDM (i.e., terpolymers composed of ethylene,

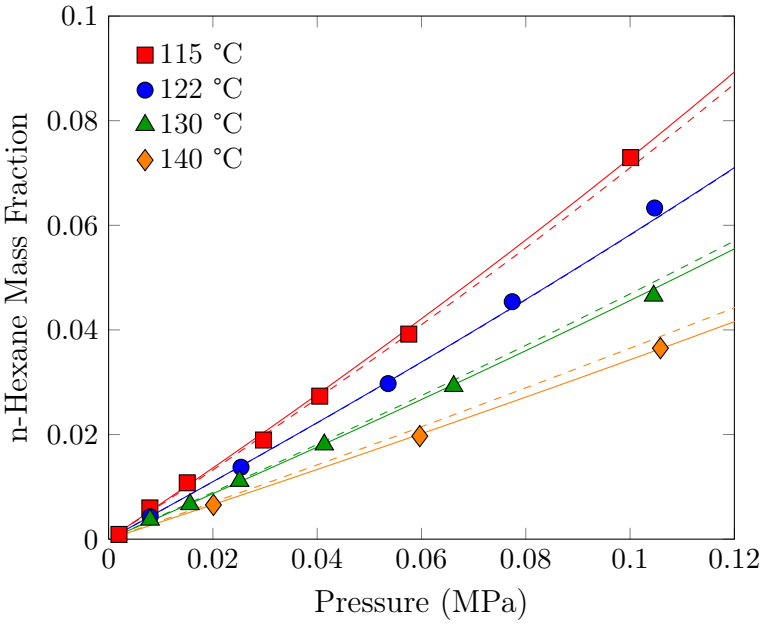

Figure 3.6: Experimental sorption isotherms of n-hexane vapor in V8880. Results of simultaneous best fitting of data by using Non Random Lattice Fluid (NRLF) model for mixtures with a temperature-independent binary interaction parameter are reported as dashed lines (best fitting value of $k_{12} = -0.0754$). Results of simultaneous best fitting of data by using NRLF model for mixtures using a k_{12} linearly dependent on temperature are reported as continuous lines (best fitting values of the two parameters are $k_{12,a} = -0.1505$ and $k_{12,b} = 1.9 \times 10^{-4}\ K^{-1}$).

propylene, and various diene monomers). These data were collected in the 90–140 °C interval, although the exact temperatures at which data were collected are not specified for proprietary reasons, indicating simply T1 for the highest temperature investigated and T5 for the lowest. These results compare well with those determined in the present investigation. The solubilities reported by Fracouer, expressed in terms of Henry's constant, are around 0.008 phr/mbar (phr stands for grams of n-hexane per 100 g of polymer) in the lowest temperature range (presumably 90 to 115 °C) and about 0.0026 at 140 °C. In our case, we have determined, respectively, a value of 0.0081 phr/mbar at 115 °C and of 0.0029 phr/mbar at 140 °C.

3.4.2 Determination of NRLF Model Parameters for Pure Components

As anticipated, based on the information available on the polymer's molecular structure, no specific self-interactions are expected to establish among groups on the polymer chains, so a thermodynamic model has been used (NRLF) that does not contain any parameter related to specific interactions. The NRLF parameters determined by the best fitting procedure of the PVT behavior of pure polymer were only the three scaling parameters and the surface-to-volume ratio s. The fitting procedure performed using the NRLF model has been applied exclusively to the data acquired above the melting temperature. The results of this procedure are reported in Figure 3.2, and the best fitting values of model parameters for pure V8880 are reported in Table 3.3. The molecular weight of the polymer has been assumed to be 80,000 g/mol.

Table 3.3: NRLF parameters calculated by best fitting procedures.

Fluid	$\boldsymbol{\varepsilon^*_h}$ (J× mol^{-1})	$\boldsymbol{\varepsilon^*_s}$ (J× mol^{-1}× K^{-1})	$\boldsymbol{\varepsilon^*_{sp,0}}$ (cm^3× g^{-1})	$\boldsymbol{s}$
n-hexane	3986.0	1.5009	1.2771	0.857
V8880	4292.4	2.7679	1.1043	0.631

The values of the three scaling parameters of the NRLF model for the case of pure n-hexane were retrieved by a fitting procedure of data on vapor-liquid equilibrium at several temperatures. Furthermore, given the chemical structure of n-hexane, no specific interactions need to be accounted for in this case. The surface-to-volume ratio, s, in this case, was taken from the literature (see Table 3.3 for details). Results of the best fitting procedure using the NRLF model for pure compounds are reported in Figure 3.3. The estimated values of model parameters are reported in Table 3.3.

3.4.3 Fitting of Sorption Isotherms

Once the NRLF parameters of the two pure compounds have been retrieved, the NRLF model for mixtures has been implemented to in-

terpret phase equilibrium between pure n-hexane vapor and binary n-hexane/V8880 mixtures. Because of the high molecular weight of the polymer molecules, the assumption that the polymer is not present in the external vapor phase has been made. Given the molecular structure of both polymer and n-hexane molecules, no self- or cross- hydrogen-bonding (or any other specific interaction) needs to be accounted for. As discussed, the NRLF model has been considered adequate to describe sorption isotherms.

To model sorption isotherms, besides the model parameters determined for pure V8880 and pure n-hexane, one additional parameter is still required, i.e., the polymer–penetrant mean field binary interaction parameter k_{12}. It measures the departure of the mean-field interaction energy of the binary mixture from the geometric mixing rule. This parameter is related to the compounds involved in the binary mixture. Based on the Lorentz–Berthelot combining rule for dispersive cross energy, we have that [112]:

$$\varepsilon_{ij} = (1 - k_{ij})\sqrt{\varepsilon_i \varepsilon_j} \tag{3.21}$$

where ε_i and ε_j are the intersegmental interaction energies in the close-packed state for pure components i and j, while ε_{ij} is the intersegmental interaction energy (cross-interaction energy) in the close-packed state for between a segment of a molecule of component i and a segment of a molecule of component j in a mixture.

The interaction parameter k_{ij} is introduced to correct for the dispersion energies of unlike molecules. Other mixing rules have been proposed for asymmetric systems or in order to better represent the critical area. The value of the interaction parameter, k_{ij}, is typically retrieved from the fitting of experimental sorption isotherms, as we have done in the case at hand. However, some theoretical insight is useful for understanding its physical origin. In fact, for relatively simple systems (e.g., mixtures of hydrocarbons or gases with hydrocarbons), the interaction parameter can be estimated from the following equation, derived from the Hudson–McCoubrey theory assuming the validity of Lennard-Jones potential [112]:

$$k_{ij} = 1 - \left[2^7 \left(\frac{\sqrt{I_i I_j}}{I_i + I_j} \right) \left(\frac{\varsigma_i^3 \varsigma_j^3}{(\varsigma_i + \varsigma_j)^6} \right) \right] \tag{3.22}$$

I_i and I_j are, respectively, the ionization potentials of compound i and

compound j, expressed in eV. ς_i and ς_j are the diameters of segments of, respectively, molecules of type i and type j. The molecular-size diameters are expressed in Å. The Lennard-Jones value of the exponent in the attractive potential (n = 6) has been used in the previous equation. With some degree of approximation, Equation 3.22 can be restated as:

$$k_{ij} = 1 - \left[\left(\frac{\sqrt{I_i I_j}}{I_i + I_j} \right) \right] \tag{3.23}$$

Different expressions are obtained in the case of different interaction potentials. Based on these theoretical arguments, one would expect a limited temperature dependence of k_{ij} and a stronger dependence on density (i.e., on mixture concentration). As reported in the literature [113], it is essential to assume the binary interaction parameter to be at least linearly dependent on temperature to correlate liquid-liquid equilibria for polymers adequately:

$$k_{ij}(T) = k_{ij,a} + k_{ij,b}T \tag{3.24}$$

In the following experimental sorption isotherms are interpreted using two approaches:

(i) using a temperature independent k_{12} ("athermal" assumption), whose value is obtained by a concurrent fitting of all four experimental isotherms;

(ii) using a k_{12} that is linearly dependent on temperature, whose value is again obtained by a concurrent fitting of all the four experimental isotherms.

- *Use of a temperature independent binary interaction parameter*

The value of the temperature independent binary interaction parameter has been retrieved by performing a one parameter concurrent best fitting with NRLF model of the four isothermal data sets for n-hexane sorption in V8880. Based on the fitting procedure, whose results have already been reported in Figure 3.6, we obtained the value $k_{12} = -0.0754$.

- *Use of a temperature dependent binary interaction parameter*

The four experimental isotherms were interpreted using the NRLF model with a k_{12} assumed to be linearly dependent on temperature:

$$k_{12}(T) = k_{12,a} + k_{12,b}T \tag{3.25}$$

From concurrent fitting of the four sorption isotherms (see Figure 3.6) we have obtained the following values for the two fitting parameters: It is

Table 3.4: Sorption isotherms fitting parameters.

$k_{12,a}$	$k_{12,b}$ (K^{-1})
-0.1505	1.900×10^{-4}

noted from Figure 3.6 that the fitting quality is improved at 130 and 140 °C as compared to the case of a temperature independent binary interaction parameter.

The values of the interaction parameters have been retrieved by fitting the experimental sorption isotherms at 115, 122, 130, and 140 °C, the NRLF model for mixtures, has been used to predict the sorption isotherms. These fittings were carried out in the case of temperature independent and temperature dependent k_{12} values. The investigated conditions are at 200 and 250 °C up to 0.2 MPa (2 atm), which are of industrial interest and not accessible with the available experimental apparatus. In Figure 3.7, it is reported the comparison of the model predictions for n-hexane solubility isotherms at T = 200 °C and T = 250 °C. The predictions were made under the assumptions of k_{12} independent of T (i.e., athermal) and k_{12} linearly dependent on T (i.e., "linear"), respectively. The predicted values of the n-hexane mass fraction obtained using a linearly dependent binary interaction parameter are lower at both temperatures than those predicted by using a temperature independent value.

The physical motivation behind the NRLF approach is the simplicity of compressible lattice fluid models. This theoretical framework is well suited for describing the thermodynamics of a mixture of solvents with rubbery/molten polymer [98] without specific interactions. The NRLF model is a reasonable compromise. It displays a more complex structure compared to the more straightforward SL theory [87–89], to account for

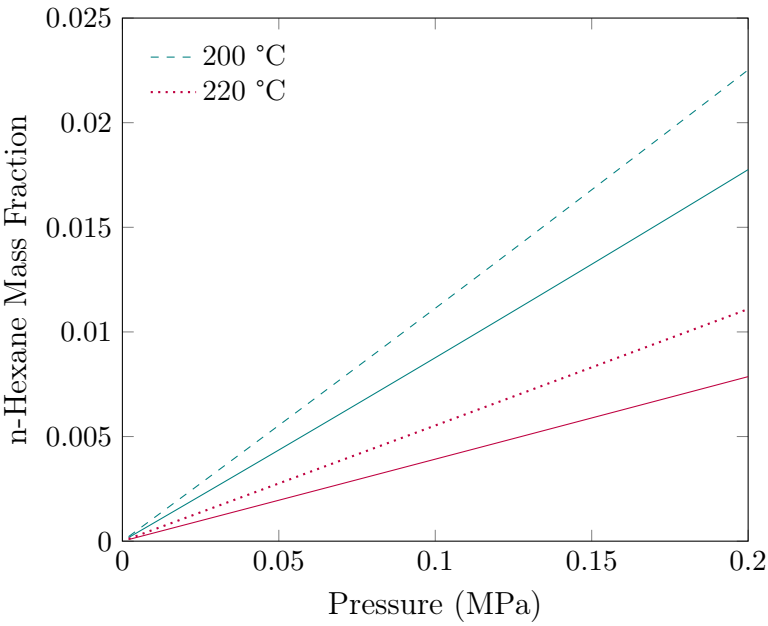

Figure 3.7: Comparison between the model prediction of n-hexane solubility isotherms in V8880, carried out respectively assuming k_{12} independent on T ("athermal", dashed and dotted lines) and k_{12} linearly dependent on T ("linear", solid line).

the non-randomness of contacts. However, unlike the SL model, it is thermodynamically consistent (see for a discussion on this point ref. [98]). Furthermore, the NRLF cannot deal explicitly with the effect of a copolymer structure.

We simplified the matter by treating the polymer as a homo-polymer. Consequently, the adopted model with the estimated parameters is only suited for describing the specific system considered (V8880) and is limited to its structural peculiarities.

Some EoS based approaches have been proposed in the literature to tackle the challenging task of modeling the thermodynamics of mixtures of copolymers and solvents. A first attempt to extend EoS theories to the case of hetero-polymers was performed by Panayiotou et al. in the framework of a preliminary simplified formulation of a non-random com-

pressible LF theory [114]. This approach is suited for the case of block copolymers of two different unit types. However, it is not adequate for different backbone structures, for example, the case of alternate copolymers. Afterward, Panayiotou et al. [115], developed a model for the case of random copolymers that was, however, limited to the prediction of the volumetric properties (EoS) of the pure copolymers.

More recently, an alternative approach has been proposed by the authors of the perturbed-chain statistical associating fluid theory (PC-SAFT) [116]. They have extended this model to the case of copolymers and their binary mixtures with low molecular weight penetrants [117]. In particular, their approach was applied to hetero-segmented molecules, displaying a well-defined alternating sequence of two repeating units or random sequences of blocks, interpreting the sorption of n-pentane in an ethylene-propylene copolymer.

Both the above mentioned LF and the PC-SAFT approaches need the introduction of *ad hoc* mixing rules for the evaluation of scaling parameters for the pure hetero-polymer based on the properties of the corresponding homo-polymers that take into account the composition in terms of types of unit segments and their statistical arrangement on the backbone. Three binary parameters, two polymer–penetrant and one polymer/polymer interaction parameters, are necessary to describe the sorption thermodynamics of polymer–penetrant binary mixtures. A pre-requisite for these approaches is a detailed knowledge of the chemical structure and the type of arrangement of the repeating units, which are not available for the industrial polymer of interest in the present investigation. Therefore, in the case at hand, the only feasible procedure consisted of using a reliable EoS model, treating the copolymer as an equivalent "fictive" homo-polymer.

3.4.4 Modelling n-Hexane Diffusivity

An example of the results of best fitting of the experimental sorption kinetics data with Equation 3.19 is reported in Figure 3.8 for the pressure step from 405 to 576 mbar at 115 °C. It is evident how the sample attains a time-independent equilibrium value in the time frame of the experiment. The very good fitting quality indicates that the assumption of "Ideal Fickian" behavior is well suited.

The same fitting method has been applied for every pressure step at

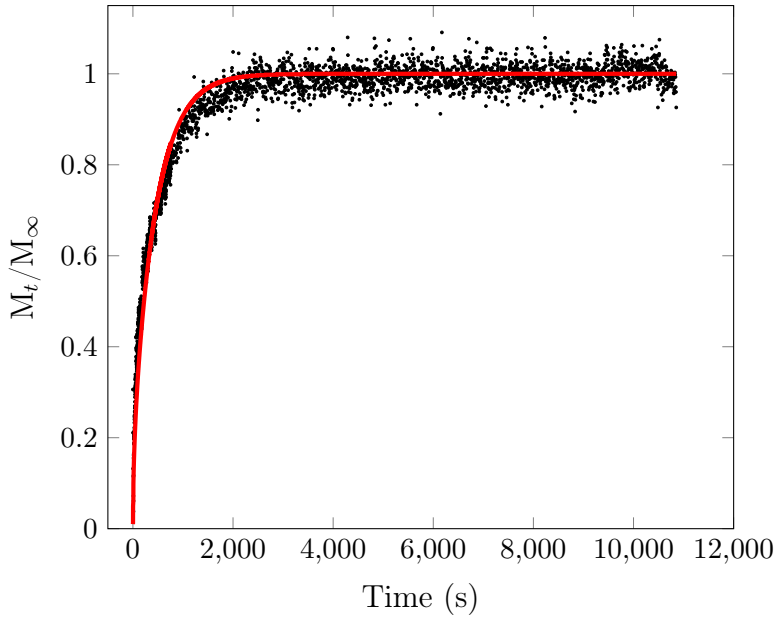

Figure 3.8: Fitting of sorption kinetics data of n-hexane for the pressure step from 405 to 576 mbar at 115 °C. Red continuous line is the result of data best fitting with Equation 3.19.

all temperatures. In Figure 3.9 are reported the calculated values of n-hexane-V8880 Fickian mutual diffusivity (determined at the four investigated temperatures by the fitting procedure of sorption kinetics curves) as a function of the average mass fraction of n-hexane in each test.

The values of mutual diffusivity evaluated at each incremental pressure step have been associated with the average value of n-hexane concentration within the sample during the sorption test, expressed as a mass fraction in the polymer–penetrant mixture (calculated by taking the arithmetic average of the initial and final values of n-hexane mass fraction at each pressure step). The values of D are affected by an error that is estimated to be $\pm\ 2 \times 10^{-7}$ cm^2/s.

In order to verify the reliability of the values determined for mutual diffusivity of n-hexane in V8880, we have compared these results with the very few data available in the literature for the diffusion of n-hexane in

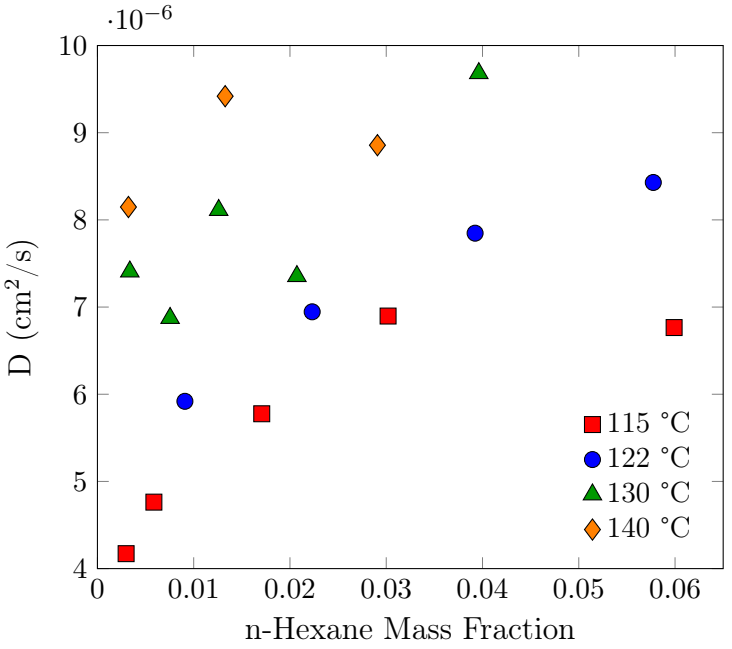

Figure 3.9: Values of n-hexane-V8880 mutual diffusivity as a function of n-hexane mass fraction in the polymer-penetrant mixture at the four investigated temperatures.

similar polymer systems. In particular, data are available in the literature for n-hexane diffusion in EPDM [111]. These data were collected in the 90–140°C interval. However, the exact temperatures are not specified for proprietary reasons, indicating simply T1 for the highest temperature investigated in that range and T5 for the lowest. The n-hexane mass fraction varied from 0 to 0.08. These results indicate that the diffusivity spans the range between 2×10^{-6} cm^2/s (at the lowest temperature and concentration) and 6×10^{-6} cm^2/s (at the highest temperature and concentration). These values are in good agreement with our data.

Further data are available in [118] for n-hexane diffusivity at 115 °C and at the zero concentration limit in ethylene-propylene elastomers. These authors determined a value of 2.241×10^{-6} cm^2/s that compares well with the value of 3×10^{-6} cm^2/s that one would estimate by extrapolating at zero concentration conditions our data collected at 115 °C.

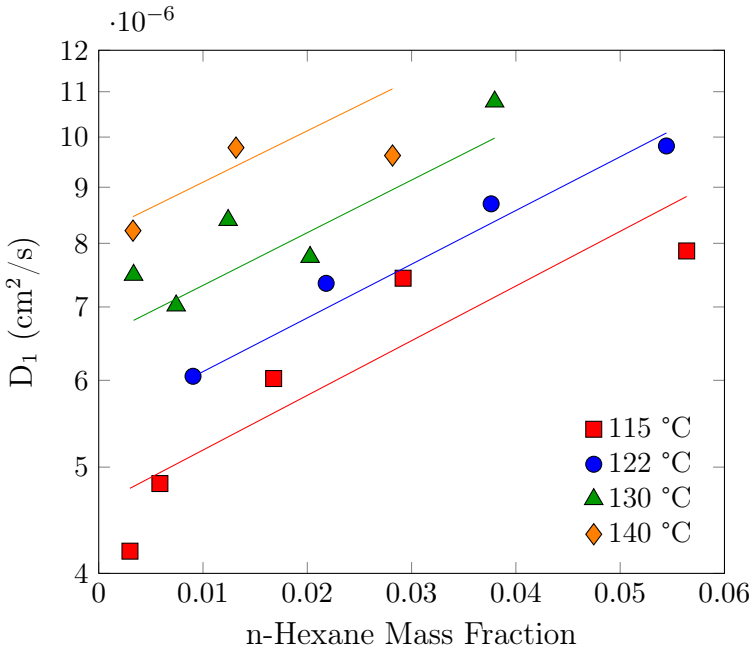

Figure 3.10: Values of D_1 as a function of mass fraction of n-hexane (log y axis) at the four investigated temperatures. Continuous lines represent best fitting of data by means of Equation 3.26

Using Equation 3.19, values of D_1 can be readily obtained at the four investigated temperatures from the values of D and are reported in Figure 3.10. Based on the free volume theory of Duda and Vrentas [30, 31], the following semi-empirical expression for the penetrant intra-diffusion coefficient can be obtained:

$$D_1 = D_{00} \exp\left(\frac{E_D}{T}\right) \exp(E_C \omega_1) \tag{3.26}$$

Note that, in formulating Equation 3.26, an explicit account of the effects of pressure has been disregarded due to the low values of pressures investigated. Here D_{00}, E_D, and E_C represent the model parameters, which can be retrieved by a concurrent regression of the available values

of D_1 reported as a function of ω_1, which represents the n-hexane mass fraction. Results of this best fitting procedure performed on the calculated values of D_1 are reported in Figure 3.10. The optimized values of the parameters obtained are:

Table 3.5: Equation 3.26 fitting parameters.

D_{00} (cm^2/s)	E_D (K)	E_C
5.57×10^{-2}	-3.653×10^3	1.220

3.5 Conclusions

Mixture thermodynamics and mass transport properties of a POE/n-hexane system have been investigated experimentally and interpreted theoretically given the considerable interest in tailoring conditions for processing operations involving this class of thermoplastic elastomers.

The experimental results regarding sorption equilibrium and diffusivities are valuable since very few experimental data are available in the literature. In particular, sorption isotherms of n-hexane in the industrial copolymer V8880 have been determined at several temperatures at subatmospheric pressures. Mutual diffusivities have also been determined at several temperatures and n-hexane concentrations; from them, intradiffusion coefficients of n-hexane in V8880 have been estimated.

Modeling sorption thermodynamics in copolymers, like the one under investigation, is challenging and possible if the macromolecular structure is known. Since details on the structure of the investigated industrial copolymer were unavailable, the polymer has been treated as a "fictive" homo-polymer approaching the modeling of sorption thermodynamics on the basis of a non-random lattice fluid theory, NRLF, developed for homopolymers. This model provided a very satisfactory interpretation of the sorption isotherms producing an excellent concurrent fitting of the experimental results at several temperatures, both with a temperature-dependent and a temperature-independent binary interaction parameter.

Dependences of mutual diffusivity of the POE/n-hexane mixture on temperature and concentration have been successfully interpreted using a semi-empirical model. The model is based on free volume concepts regarding the n-hexane intra-diffusion coefficient and a thermodynamic contribution accounting for the composition dependence of n-hexane chemical potential.

Once inserted in the equations that rule the evolution of the V8880/n-hexane system under processing, the quantitative information provided by the thermodynamic and mass transport models developed here allows the adequate simulation and optimization of working conditions.

Chapter 4

Effect of volatile solvents on bubble and bulk foam stability in nonaqueous systems

4.1 Introduction

A liquid foam consists of a gas dispersed in a continuous liquid phase, where bubbles are generated by entrainment or by the diffusion of a dissolved gas [119]. Liquid foams are found in a variety of industrial and daily-life applications such as bioreactors [120], bubble columns [121, 122], polymer processing [123], froth flotation [124], water waste treatment [125], food [126, 127], and pharmaceuticals [128]. Liquid mixtures commonly encountered in these applications may include various components such as surfactants, volatile components, and antifoaming agents [129]. In the present work the focus is on simple binary mixtures of two soluble liquids.

Since bubbles are the defining component of foams, it is necessary to analyze their behavior to fully understand this type of system. For example, when a single bubble rises to the gas-liquid interface, a thin liquid film is entrained in the center of the bubble (Figure 4.1) [130], and the time for this film to drain is central to determining the foamability of a liquid and the stability of the foam [131, 132]. The interest in single-bubble characterization techniques has continued to increase [133], with particular emphasis on dynamic fluid-film interferometry (DFI) which is a well-established and

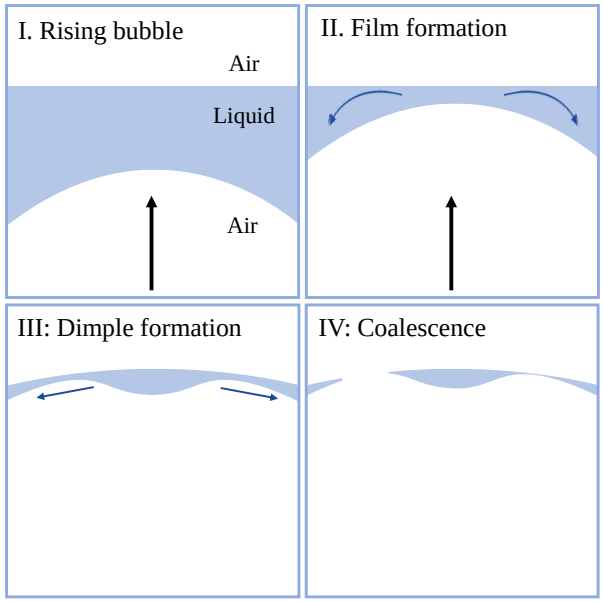

Figure 4.1: Sketch of thin liquid film formation and evolution. (I) Prior to film formation, the bubble rises and is relatively far from the interface. (II) Upon reaching the air-liquid interface, the bubble traps a thin liquid film that begins to drain due to the combined effect of bubble movement and capillary forces. (III) Once the bubble is no longer moving, it stabilizes at the air-liquid interface. The pressure in the film increases, reaching the pressure in the bubble and causing the film to deform into the so-called dimple shape. (IV) Eventually the film ruptures where it is thinnest, inducing bubble coalescence.

reliable approach used in a number of different custom-built experimental setups [130, 134–142]. DFI can be used to examine the drainage mechanism of thin film, by precisely tracking the shape of the film as it evolves due to gravitational and interfacial stresses. As such, the present work also leverages DFI to study single bubble-films due to the established link to bulk foams [143].

Many factors influence the film drainage process, such as surface tension, viscosity, temperature, bubble size, surfactants, Marangoni stresses, and evaporation. In some cases, a stable foam is desired as part of a food product made with edible oils [144]. Whereas foams are deleterious and

must be destabilized in liquid filling operations and separation processes [145, 146]. Previous studies in this research area have sought to understand this dependence, though most of this work investigates aqueous solutions [143, 147–152], while nonaqueous systems are studied far less.

Recently, the study of the stability of foams in binary mixtures of nonaqueous liquids has been shown to involve previously unanticipated complexity. For example, it was found that the interaction between the liquid components may lead to time-dependent oscillations in the the film thickness [153, 154], or even to non-monotonic trends in the foamability with varying weight fractions [155, 156]. It is quite common in industry to have polymers or oils mixed with compatible solvents [157, 158]. Such solvents are often much more volatile than the oil or polymer and may be present in concentrations that can cover several orders of magnitude.

The present work concerns film drainage in surfactant-free, non-aqueous binary mixtures, where one component has a much lower viscosity and much higher volatility than the other, but similar surface tension. The hypothesis is that four competing effects will be directly observed trough changes in the rate of film drainage. First, the evaporation of the volatile solvent will contribute to faster thinning of the film by simple mass loss. Second, as the concentration of the low-viscosity, volatile component decreases (due to evaporation) during drainage, this will lead to an increase in film viscosity that will slow down drainage. Third, evaporative cooling in the film will result thermal Marangoni flows that stabilize the film by reversing the flow out of the film [151]. Finally, the slight difference in surface tension between the two components will result in a solutocapillary Marangoni flow that will speed up drainage.

A secondary hypothesis tested in this work is that results of single-film experiments will be useful in predicting the stability of bulk foams made from the same binary mixtures. Such a connection to bulk foams would further confirm the validity of the single-film approach for foam characterization, encouraging future research with DFI techniques to increase fundamental knowledge of a wide variety of foam systems.

4.2 Materials and methods

4.2.1 Chemicals and mixtures

Binary mixtures of silicone oil (Clearco Products Inc. PSF-10,000cSt and PSF-1,000cSt) with acetone (ACS Grade) or decane (Tokyo Chemical Industry Co., Ltd. Decane #D0011) as solvents were used for single-film experiments. Bulk foam mixtures were made by mixing silicone oil (Clearco Products Inc. PSF-100cSt and PSF-10cSt) with acetone as the solvent.

4.2.2 Dynamic fluid-film interferometer

Single-film experiments were performed with a dynamic fluid-film interferometer (DFI) as shown in Figure 4.2 (modified from the design published in [143]). A single bubble with a volume of approximately 380 ± 9 nL (450 μm spherical radius) is released into a chamber filled with liquid (PDMS mixture). The bubble is released from a plastic tube (Miniature Firm EVA Plastic Tubing, $1/16''$ OD $\times$ $0.02''$ ID) connected trough a screw fitting (PEEK Fitting, $1/16''$ ID) to the bottom of the chamber, approximately 10 mm below the liquid surface. The bubble then rises towards the air-liquid interface, where the chamber is slightly overfilled to generate a convex meniscus to guarantee that the bubble is axially centered.

The bubbles used for experiments were generated in a T-junction with air entering perpendicular to the flow of liquid. The flows are generated by a two-barrel syringe pump (Harvard Apparatus PHD ULTRA) controlling two syringes (1 mL Luer-Lok™ Syringe and 3 mL Luer-Lok™ Syringe), and the flow-rates and flow-rate ratio can be changed (by changing the syringes) to reach the desired bubble diameter [159, 160]. The resulting bubbles have a stable, slug shape. Once a uniform train of bubbles is generated, the flow is stopped, and eventually, each bubble can be used for a DFI experiment when necessary, by displacing the fluid volume needed to release a single bubble from the tube.

The chamber was machined from black Delrin plastic to reduce the amount of light reflected by the background, and has a volume of approximately 0.15 mL (4 mm ID $\times$ 12 mm depth) (Figure 4.2b). The design of the chamber also allows us to enclose the interface with a lid made from black Delrin with a sapphire window that only reflects near-infrared ra-

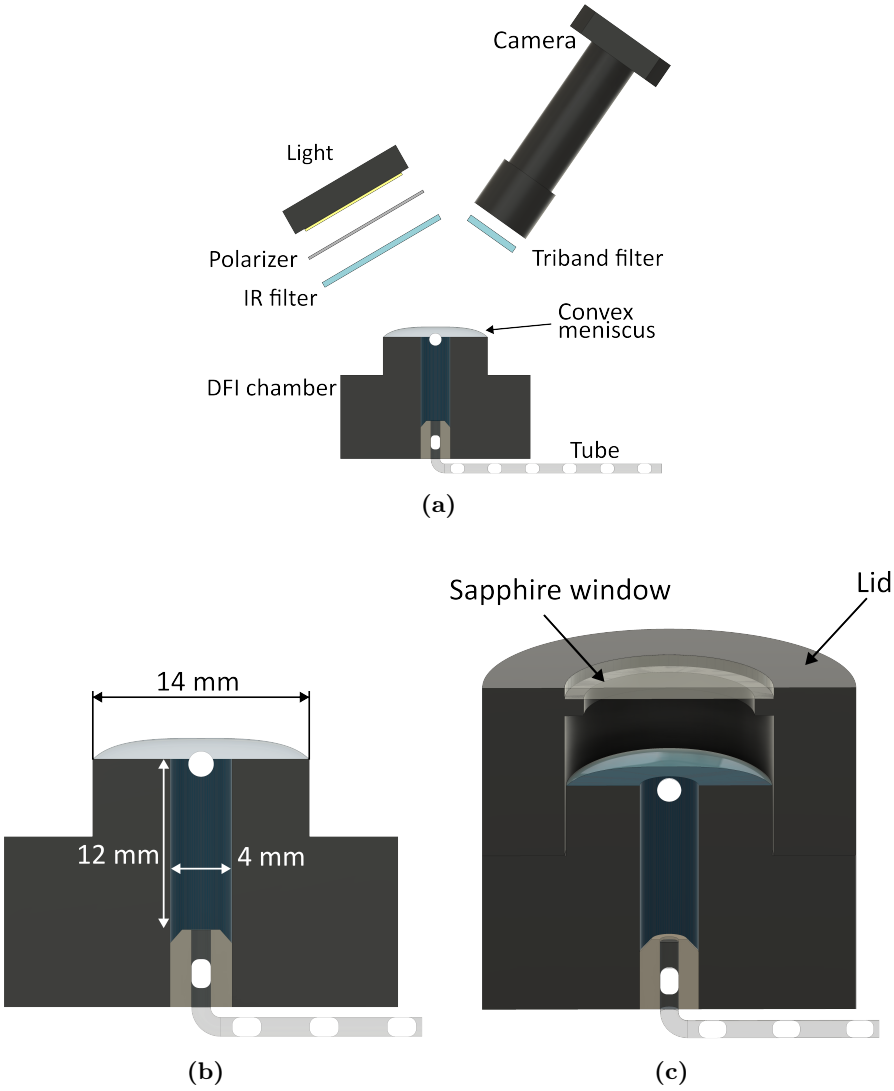

Figure 4.2: (4.2a) Schematic of the entire DFI setup showing optical components. (4.2b) Detail of the DFI chamber showing the most relevant dimensions. (4.2c) Closed configuration of DFI chamber. The lid suppresses solvent evaporation.

diation (Edmund Optics #20-642) (Figure 4.2c). The upper part of the chamber is narrower than the body, to allow the formation of a stable convex meniscus of liquid. The liquid meniscus together with the aspect ratio of the interior of the chamber keeps the bubble on the axis of symmetry during the experiment.

As shown in Figure 4.2a, the optical components consist of a camera (Imaging Development Systems UI-3880LE) and a light source (CCS Inc. TH2-51×51SW) both at an angle of 40° relative to the axis of symmetry. To improve the quality of the light interference, the camera is equipped with a dichroic filter (Edmund Optics #87245) with three pass-bands and center wavelengths at 457 nm, 530 nm, and 628 nm. In addition, a high transmission linear polarizing film (Edmund Optics #19-020), oriented in the *p*-polarizing direction, is attached to the light. Finally, an infrared cut-off filter (Edmund Optics #54-516) is interposed between the light and the chamber to reduce radiative heating and act as a baffle to reduce air flow near the chamber caused by natural convection from the heat of the light source. The entire setup is also enclosed in a transparent box and situated on a vibration-isolating table to reduce other environmental disturbances.

During each of the experiments reported in this paper, a bubble is released from the tube and rises in the liquid until it reaches the air-liquid interface. As the bubble nears the interface, the film drainage begins and light interference in the film is recorded until the bubble coalesces. There are two primary advantages of this setup with respect to the state of the art. First, the angled configuration of the light and camera are adopted to avoid non-uniform illumination of the film that can be a problem in coaxial lighting setups. Second, the formation of individual bubbles in a T-junction, rather than releasing them from an air-filled needle, aids in achieving significantly smaller bubble sizes in a convenient and highly repeatable way.

4.2.3 Analysis of interference data

The theory for light interference is well known and clearly described by other researchers [161, 162]. In general terms, light directed towards a thin film surrounded by a medium with a different refractive index is reflected from the upper and lower interfaces of the film. The reflected light waves interfere with one another, generating a pattern of colors that correspond

to the thickness of the film. The intensity for each wavelength of light can be described as a function of the corresponding Fresnel coefficients.

In the majority of DFI setups, the camera is perpendicular to the film. However, in this work an angled configuration with a polarized light source is presented, leading to a less simplified equation for the intensity of interfering light. While the equations do not change significantly for an incident angle $\alpha < 30^o$, our setup has an incident angle of approximately 40^o and its effect must be taken into account. In this case, the intensity of the interfering light as a function of wavelength $I(\lambda)$ and the Fresnel reflectivity coefficients R_1 and R_2, are computed through the following equations:

$$I(\lambda, d) = I_0(\lambda)\left[R_1 + R_2(1-R_1)^2 + 2\sqrt{R_1 R_2(1-R_1)^2}\cos\Phi\right] \tag{4.1}$$

$$\Phi = \left(\frac{4\pi n_2 d}{\lambda} + \psi\right)\cos(\Theta) \tag{4.2}$$

$$R_1 = \left|\frac{n_1\sqrt{1-(\frac{n_1}{n2}\sin\alpha)^2} - n_2\cos\alpha}{n_1\sqrt{1-(\frac{n_1}{n2}\sin\alpha)^2} + n_2\cos\alpha}\right|^2 \tag{4.3}$$

$$R_2 = \left|\frac{n_2\cos\alpha - n_1\sqrt{1-\frac{n_1}{n2}\sin\alpha)^2}}{n_2\cos\alpha + n_1\sqrt{1-(\frac{n_1}{n2}\sin\alpha)^2}}\right|^2 \tag{4.4}$$

Here I_0 is the incident light intensity, λ is the wavelength of the light, and Φ is the phase difference between the light beams reflected from the two film interfaces. The phase difference Φ is a function of the film thickness d, the liquid film refractive index n_2, the refraction angle in the film Θ, which is evaluated by $\Theta = \arcsin(n_1/n_2 \sin\alpha)$, and the phase shift ψ resulting from reflection at an interface between two media with different refractive indices. Upon reflection at the upper interface, the light is reflecting from a medium with a higher refractive index, so a phase shift of π occurs; but when it reflects from the lower interface, it is reflecting from a medium with lower refractive index and no phase shift occurs for a total relative phase shift of $\psi = \pi$.

A reference color map correlating the resultant color to the thickness of

the film is generated by taking into account the interference in the film from the specific light source, along with filtering caused by the transmission of the various optical components, and integrating based on the sensitivity of the red, green, and blue camera pixels at each wavelength. The refractive index of silicone oil was measured at different solvent concentrations, and found to have a maximum deviation of 0.6% from the pure silicone oil refractive index of 1.403, which has no impact on the color map. The interference colors recorded in an experiment are then manually matched, frame by frame, with the corresponding colors on the color map with the help of custom software written in Python. On each frame, the colors matched at different spatial locations are then used with interpolation to obtain a complete thickness map of the film. The data is finally reduced to the volume of the film, as well as the film thickness at the center of the film and maximum, mean, and minimum film thicknesses as a function of time.

4.2.4 Bulk foam measurements

The bulk foam measurements are performed with a foam analyzer (Krüss Scientific DFA100). The foam analyzer consists of a glass porous plate (pore size: 10–16 μm) placed at the bottom of a glass column (40 mm I.D.), held together by a clamp and sealed with a silicone gasket. The column is located between an LED light and a line-scan camera (1×1728 pixels), and is filled with 60 mL of liquid (unless stated otherwise). Air is pumped into the liquid from below through the porous plate at a constant flow rate of 0.5 L min^{-1} (unless stated otherwise) in order to produce foaming. The foam-air boundary is detected over time with an accuracy of ± 1 mm.

The initial volume of liquid and the airflow rate were selected after a few trials with pure silicone oil. The total volume of liquid plus foam produced – at steady state – as a function of gas flow rate and initial liquid volume are shown in Figure 4.3. We see that the foam volume (total volume minus initial liquid volume) is maximized at an airflow of 0.5 L min^{-1} and is approximately the same for both initial liquid volumes. Initially, at lower flow rates, the volume increases proportionally with the flow rate, but decreases again at higher flow rates, likely due to the formation of larger bubbles from the porous plate at such high flow rates.

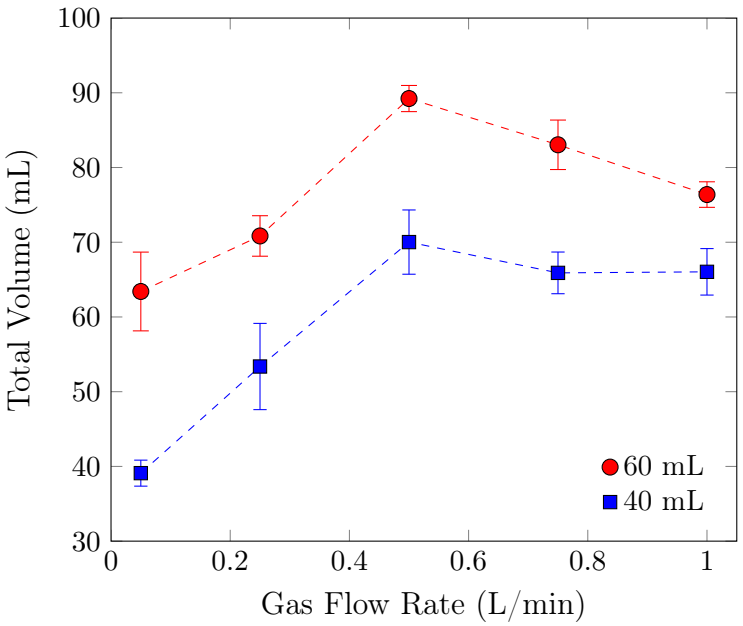

Figure 4.3: Total volume of liquid plus foam of 100 cSt silicone oil at steady state, after at least 100 s of continuous bubbling.

4.2.5 Surface tension and viscosity

Surface tension was measured with the pendant droplet technique using open-source software [163]. Surface tension vs. composition for the different mixtures used are given in Figure 4.4. The viscosity was measured with a conventional rotational rheometer (Anton Paar MCR 302). All the measurements were conducted at 23°C with a temperature resolution of ±0.1°C and a 50 mm diameter parallel plate configuration (PP50 and inset I-PP50/SS, Cat. No. 16222). The shear rate was varied logarithmically in the range 0.1-100 s^{-1} and the viscosity was found to be Newtonian in that range. Figure 4.5 shows shear-averaged viscosity at different solvent weight fractions.

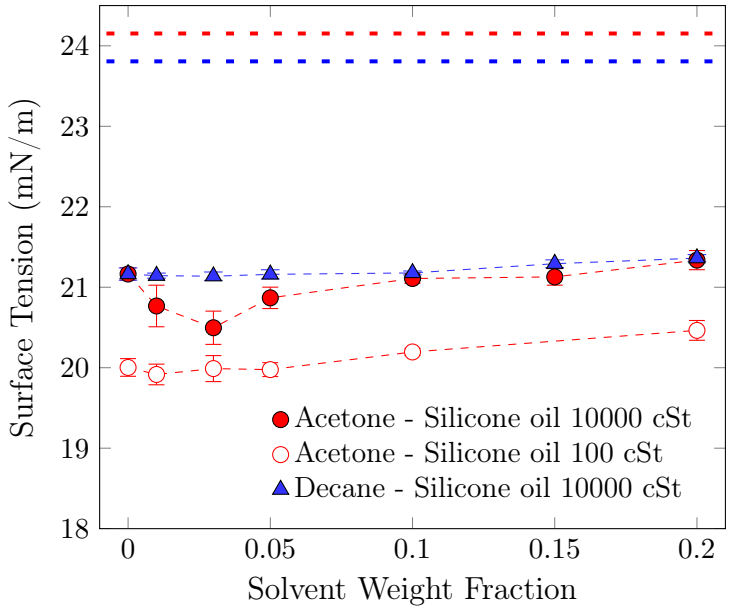

Figure 4.4: Surface tension isotherms for mixtures used for DFI and bulk foam experiments. Horizontal dashed lines represent the surface tension of pure solvents.

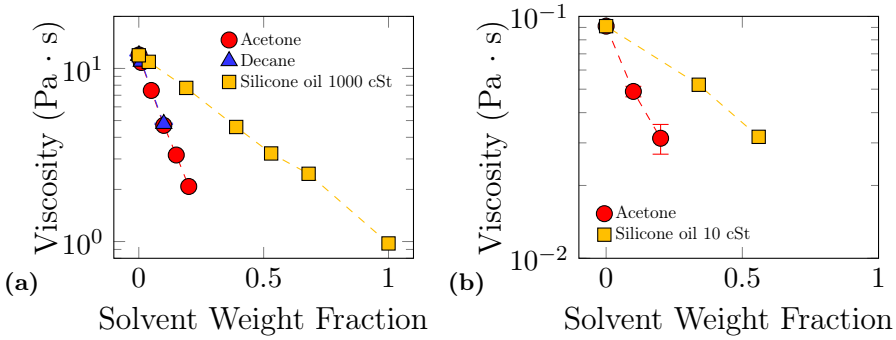

Figure 4.5: (4.5a): Viscosity isotherms for silicone oil 10000 cSt mixtures. (4.5b): Viscosities of silicone oil 100 cSt solutions used for bulk foam experiments.

4.3 Results and discussion

4.3.1 Data reduction of single-film experiments

As mentioned above, the DFI technique allows the film thickness between the bubble and the atmosphere to be measured as a function of time and space. In Figure 4.6, the center-point, maximum, minimum, and mean film thicknesses coupled with the film radius and volume of the film are shown for a typical single-film experiment. Because the films generated in this study are all axisymmetric until the final stages of drainage, the shape of the film is accurately represented by the 2D slices of the film shown in Figure 4.6c. In addition, the majority of the physics related to film drainage can be captured by tracking only the minimum and center-point film thicknesses of the film. This choice has the advantage of being easily computed from the data and is also used in several previous studies [135, 147, 148, 164].

Analysis of Figure 4.6 shows that the bubble interface exhibits a rounded shape at the early stages of the drainage, whereas it assumes an inverted curvature at long times. This accumulation of fluid at the center of the bubble is the so-called dimple and its appearance has been well-known for many years [165]. As can be seen in Figure 4.6a, the appearance of the dimple is clearly marked by the time point when the minimum film thickness begins to deviate from the thickness at the center of the bubble. The continual decrease of the minimum thickness after dimpling shows that the film continues to thin at the rim until rupture, as expected [166].

For these experiments with a freely-rising bubble, the film radius first increases almost linearly as an effect of the bubble deformation against the air-liquid interface. Then the film radius suddenly switches to a more slowly increasing function that approaches a constant value as shown in Figure 4.6b. This sudden change in the rate of increase in the film radius occurs exactly at the moment that the film volume stops increasing with time due to the competing effects of film expansion and drainage as described previously by Frostad et al. [143]. Note that the film volume V_f is computed by integrating thickness over the film area and the mean film

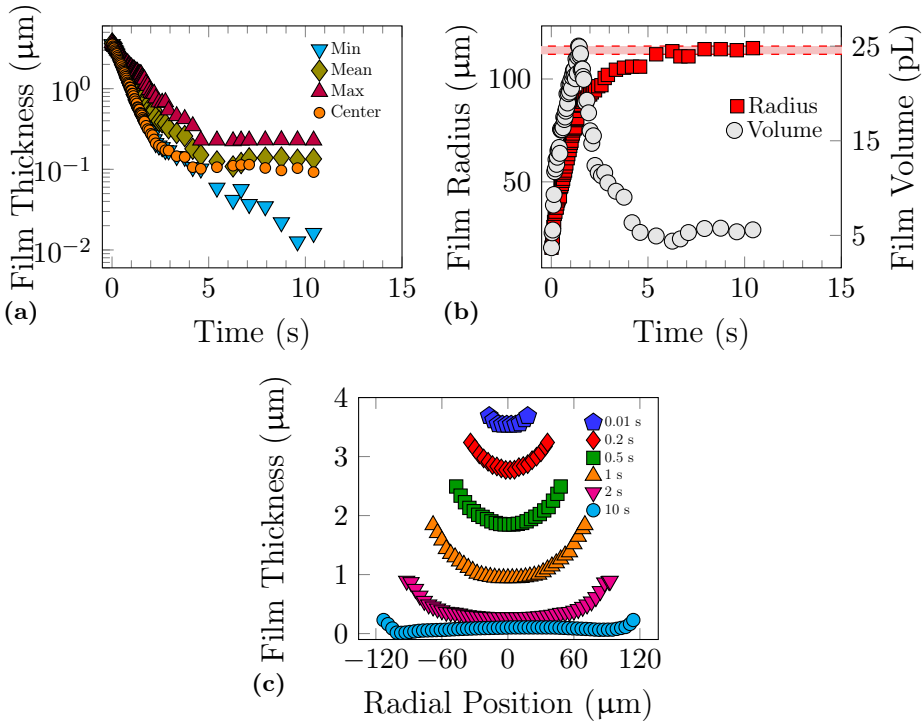

Figure 4.6: (4.6a) Evolution of minimum, mean, maximum and center film thicknesses measured with DFI experiments for pure silicone oil 12 Pa · s. (4.6b) Behavior of the film radius and volume. The dashed red lines represent the theoretical film radius of the bubble at equilibrium, computed based on the maximum and minimum radii of the bubbles generated in the T-junction. (4.6c) Film thickness profiles at the centerline.

thickness h_{mean} is defined based on this volume as:

$$h_{mean} = \frac{V_f}{\pi R_f^2}, \tag{4.5}$$

where R_f is the film radius.

4.3.2 Relation of pure fluid data to established theory

In recognition of the fact that the hydrodynamics of the film drainage problem for a clean interface are understood relatively well, here we briefly outline the relevant theoretical predictions. In particular, we identify the appropriate scaling factors for non-dimensionalizing our data that will be useful when evaluating the role of a volatile solvent on the drainage process. An important dimensionless quantity for this system is the Bond number:

$$Bo = (\rho_l - \rho_g) g R^2 / \gamma, \tag{4.6}$$

where ρ_l and ρ_g are the liquid and gas densities respectively, γ is the surface tension of the liquid, g is the acceleration due to gravity and R is the bubble radius. In the present work, where $Bo \ll 1$, the film drainage is mainly controlled by capillary forces. In that limit and for thin films, the lubrication approximation offers an accurate description of the film drainage problem [167].

From the lubrication approximation (and other relevant assumptions) the rate of film drainage can be predicted in two regimes. First, the initial rate of film drainage at the center of the film h_c is well described by an exponential decay [135, 148, 164, 168]. Assuming zero interfacial stress and a flat air-liquid upper interface, a balance between the radial component of the tensile stress σ_{rr} and the capillary pressure in the film can be written as follows:

$$\sigma_{rr} = -3\eta \frac{1}{h_c} \frac{dh_c}{dt} = \frac{\gamma}{R}, \tag{4.7}$$

which after integration leads to:

$$h_c = h_0 \exp\left(-\frac{1}{3}\frac{t}{t_c}\right), \tag{4.8}$$

where h_0 is the initial film thickness at the center, t is time, and $t_c = \eta R/\gamma$ is the viscocapillary time scale with η being the viscosity.

At later times, after dimpling has begun, the rate of decrease in minimum film thickness h_m is predicted by the following scaling relations

[166, 169]:

$$\frac{h_m}{R} \sim \left(\frac{t}{t_c}\frac{R}{\lambda R_f}\right)^{-1}; \qquad \frac{h_m}{R} \sim \left(\frac{t}{t_c}\frac{R}{R_f}\right)^{-2/3} \tag{4.9}$$

where the former applies when the interfacial stress is zero (a clean interface), the latter applies when the tangential velocity of the interface is zero (usually caused by surface active components), and λ is the ratio of the bubble viscosity to the liquid viscosity. Finally, the expected maximum film radius is predicted from a balance between buoyancy and capillary forces acting on the film at equilibrium:

$$\frac{R_f}{R} = \sqrt{\frac{2}{3}Bo}, \tag{4.10}$$

$$\frac{R_f^2}{R^2} = \frac{2}{3}\frac{\Delta\rho g R^2}{\gamma}, \tag{4.11}$$

and for this specific case $R_f/R \approx 0.248$.

Comparing Equation 4.8 with the data in Figure 4.7c we see excellent agreement with the theory. While the data for the minimum film thickness is a little bit noisy, in Figure 4.7b we see that the data for high-viscosity silicone oils (12–10.8 Pa · s) and low-viscosity (7.4–2.1 Pa · s) follow the scaling relations for mobile and immobile interfaces provided in Equation 4.9, respectively. The different rates of decrease in minimum thickness for different viscosities can be attributed to the magnitude of thermal Marangoni stresses, which increase as viscosity decreases, immobilizing the interface. Finally, in Figure 4.6b and Figure 4.7d, we see the final radius of the film matches the theoretical prediction very precisely.

4.3.3 Effect of a volatile solvent

As our first step to understand the influence of a volatile solvent on the film drainage process, we performed a drainage experiment in a liquid where acetone is mixed with 10 St PDMS (with a viscosity of 12 Pa·s) to form a mixture that is 20% acetone by weight. To observe any differences due to the solvent, the results are compared to the pure 12 St PDMS without solvent, as well as to a mixture of two different viscosities of PDMS

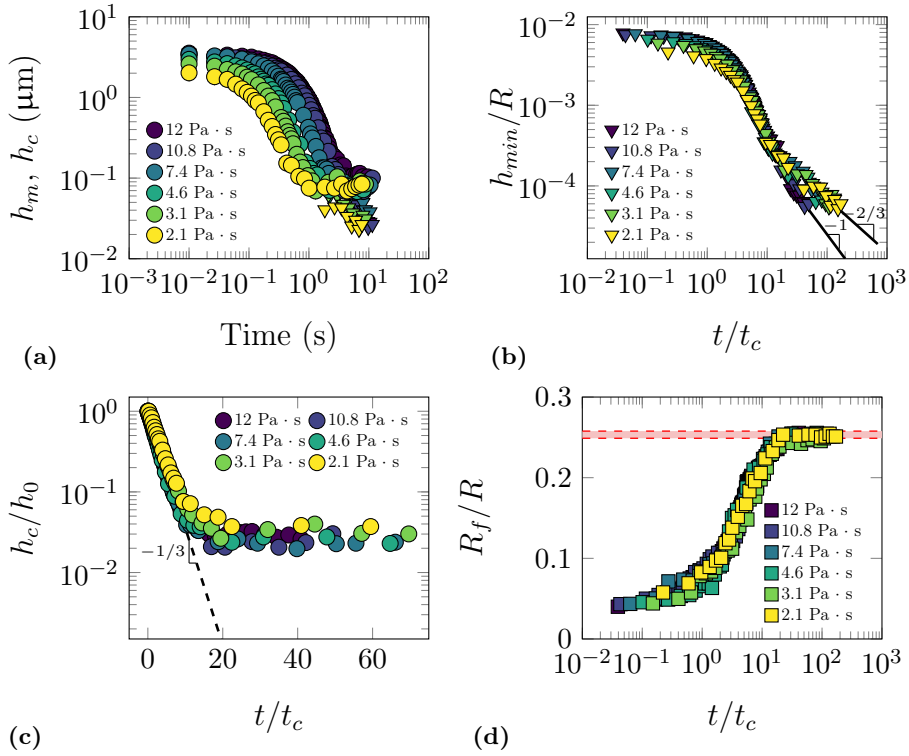

Figure 4.7: (4.7a) Film thickness as a function of time for pure silicone oils with different viscosities. (4.7b) Film thickness scaled by bubble radius as a function of non-dimensional time. Solid lines represent the scaling relations provided in Equation 4.9. (4.7c) Film thickness scaled by initial film thickness as a function of non-dimensional time. The dashed line represents exponential drainage provided in Equation 4.8. (4.7d) Radial extend of the thin film region scaled by bubble radius as a function of non-dimensional time. In (4.7a), (4.7b), and (4.7c) circles and triangles represent center and minimum film thickness, respectively.

(10 St + 1 St) such that the viscosity matches that of the solvent mixture (2.1 Pa·s). In Figure 4.8a, we show the time evolution of the film thickness at the center of the film for each of these fluids with the chamber in both the open and closed chamber configurations (see Figure 4.2).

The film thickness vs. time shown in Figure 4.8a shows that the

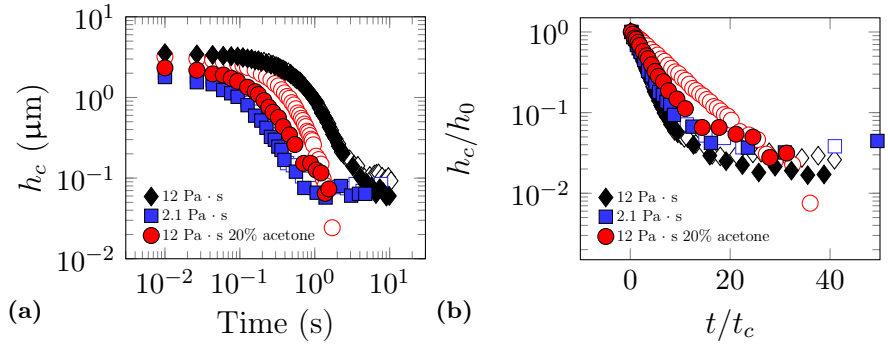

Figure 4.8: (4.8a) Effect of evaporation on silicone oils film drainage at the bubble center. (4.8b) The same data scaled according to the exponential drainage (Equation 4.8). Unfilled and filled markers represent open and closed chamber configuration respectively.

thickness for the acetone mixture appears to be bounded between the 10 St PDMS and the viscosity-matched PDMS. However, as mentioned in the previous section, comparing the data in a normalized way by non-dimensionalizing in accordance with known theory is helpful for seeing the mechanistic differences, as done in Figure 4.8b. As expected, the dimensionless drainage rate for both viscosities of PDMS, in both the open and closed configuration, collapse to approximately the same curve (with the minor differences being similar in magnitude to those shown in Figure 4.7c).

When acetone is present in the liquid, the initial rate of drainage is significantly reduced in the open configuration where evaporation occurs continuously. This decrease in the drainage rate suggests that of the four mechanisms identified in the introduction that may alter the drainage rate – mass loss (speeds up drainage), viscosification (slows down), thermal Marangoni stress (slows down), and solutocapillary Marangoni stress (speeds up drainage in most cases) – one or both of the two that slow down drainage are dominant. However, in the closed configuration, evaporation is expected to be stopped or at least significantly reduced and the drainage rate is only slightly slower than the PDMS without acetone.

After the initial portion of the drainage where the slope is constant on semi-log coordinates, the thickness at the center of the film will become

nearly constant as expected when a dimple forms. This behavior is clearly seen for every case in Figure 4.8b except for the solvent mixture in the open configuration. This absence of a dimple is at odds with the slowing down that is observed because both a viscosification of the film and thermal Marangoni stresses would be expected to enhance dimple formation [151]. Therefore, this suggests that as the film continuously gets thinner, that one of the other mechanisms that speed up drainage is increasing in importance. From a practical standpoint, this suggests that the presence of a solvent tends to inhibit film stabilization, even though the initial rate of drainage is slowed down.

4.3.4 Effect of solvent volatility and concentration

In the previous section, we showed that the presence of a solvent can alter the rate of drainage both quantitatively and qualitatively. In both cases, viewing the data plotted in a dimensionless way made these differences easy to observe, so the data will continue to be plotted in this way. In this section, we examine the influence of the amount of acetone by varying its mass fraction from 0.1% to 20%, as well as the type of solvent. Decane was selected as the alternate solvent due to its similar viscosity and surface tension, but lower volatility compared to acetone. In all cases, the experiments were performed with the chamber in the open and closed configurations (see Figure 4.2).

In Figure 4.9a, we see that for both solvents and both configurations, with a solvent concentration of 1% or less, there is no difference from the pure PDMS case.

According to the analysis in Section 4.3.2, the slope of the minimum thickness drainage curve on log-log coordinates should present values between two limiting cases of zero interfacial stress and zero tangential velocity at the interface. Figure 4.10a clearly shows how the slope in the presence of 15% and 20% acetone is larger than -1, suggesting that the abrupt decay in minimum thickness before coalescence is not solely due to Marangoni stresses. Previous studies have shown that the speed-up of drainage when the film gets thinner ($\approx$100 nm) is attributable to mass loss due to evaporation [147, 170]. These authors proposed a model accounting for evaporation that can predict drainage slopes greater than -1, which may provide a physical interpretation to our findings. Moreover, the fact

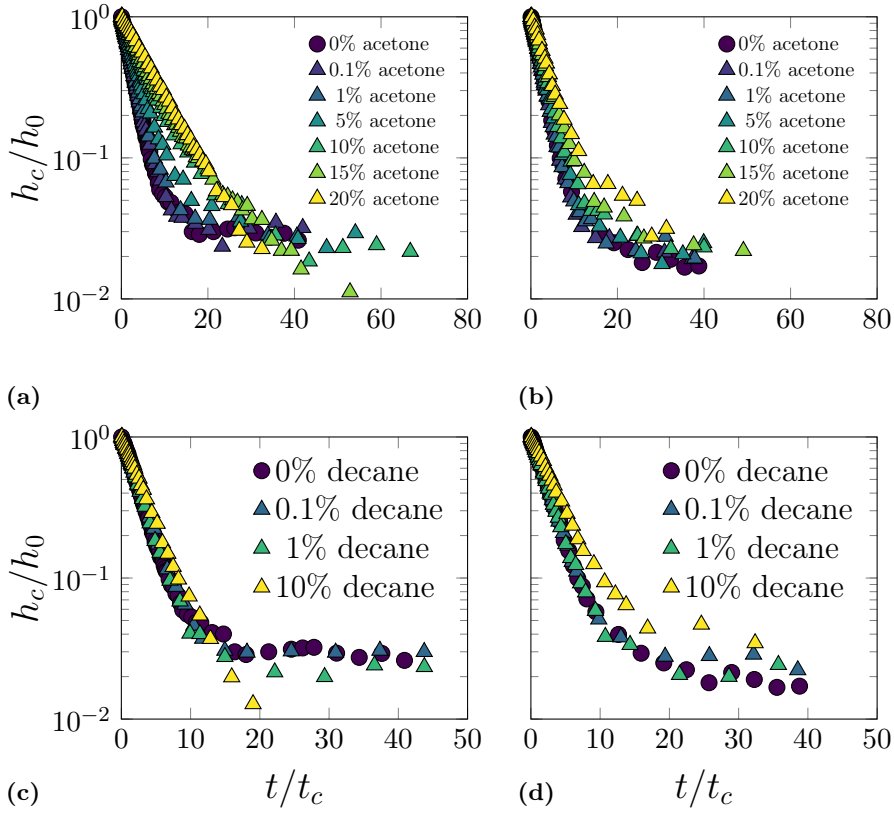

Figure 4.9: Film thickness at the bubble center scaled with the initial thickness as a function of non-dimensional time. Circles represent pure silicone oils while triangles represent silicone oil-solvent mixtures with the same initial viscosity. (4.9a and 4.9b) Data of silicone oil-acetone mixtures with open and closed chamber configuration, respectively. (4.9c and 4.9d) Data of silicone oil-decane mixtures with open and closed chamber configuration, respectively.

that this behavior occurs only at the highest acetone concentration supports this hypothesis.

In the presence of decane, film viscosification is bland before and during film drainage, as shown in Figure 4.9c. However, with 10% decane the film does not stabilize before coalescence, showing no dimple formation. According to Figure 4.10c drainage slope is similar to that with 20%

acetone shown in Figure 4.10a. This behavior suggests that decane evaporation from the liquid surface is very slow when the bubble is far from the interface, but when the film becomes very thin, decane mass loss becomes dominant.

Figure 4.9b and Figure 4.9d show drainage data of silicone oil in the closed chamber for acetone and decane, respectively. The curves at the higher solvent weight fractions separate slightly from the others. This happens because after the chamber was closed, we waited 10 minutes to reach the equilibrium partial pressure of the solvent before releasing the first bubble. During this time, it is possible that a small amount of acetone evaporated from the film. On the other hand, the first bubble was released immediately after the mixture was poured into the chamber for the open configuration.

4.3.5 Impact on coalescence

The bubble coalescence time is shown as a function of solvent weight fraction in Figure 4.11 to emphasize the destabilization effect of the solvent.

The minimum and center film thicknesses exhibit a non-monotonic behavior, at least for acetone. This result suggests that in the concentration range 0–0.05 there is a dominance of the stabilizing thermal Marangoni flow over the solutocapillary Marangoni flow induced by solvent evaporation. Whereas, increasing the weight fraction in the range 0.05–0.2 the behavior is different.

Figure 4.12a shows how the center and minimum film thickness have the same value at the highest acetone concentrations. This suggests that when acetone is relatively abundant, it may be present even at the very end of drainage, inhibiting film stabilization. In such conditions, the film is less likely to assume a more stable dimpled shape. This characteristic can be better appreciated in Figure 4.13, which shows how a barely asymmetric dimple is always present before coalescence in the concentration range 0–10. On the other hand, at 15% and 20% acetone, solvent evaporation prevents dimple formation preserving an axisymmetric concave thickness profile.

Another remarkable insight is the increase in film radius with the solvent concentration. Figure 4.14 shows how the radius of the film increases with solvent concentration up to 30% more than the pure silicone oil film.

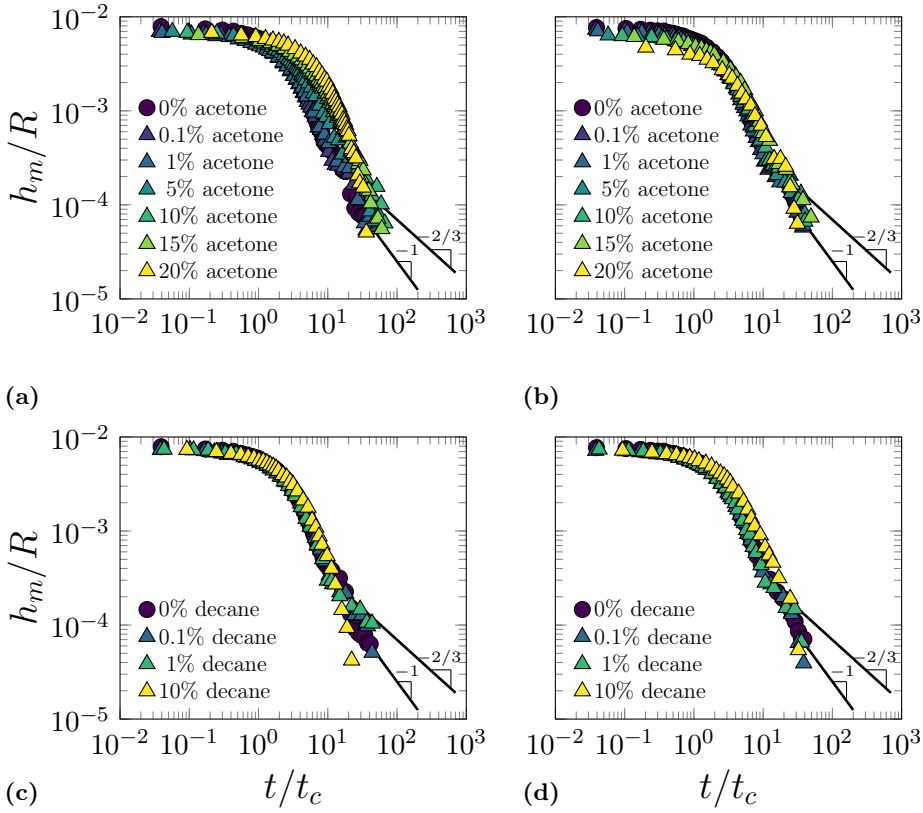

Figure 4.10: Minimum film thickness scaled with the bubble radius as a function of non-dimensional time. Circles represent pure silicone oils while triangles represent silicone oil-solvent mixtures with the same initial viscosity. (4.10a and 4.10b) Data of silicone oil-acetone mixtures with open and closed chamber configuration, respectively. (4.10c and 4.10d) Data of silicone oil-decane mixtures with open and closed chamber configuration, respectively.

This increase is probably due to solvent evaporation during bubble rise in the bulk liquid, increasing bubble volume. Interestingly, the film radius decreases for silicone oil with 20% acetone, suggesting that the bubble coalesces when it has not stabilized at the interface yet. This interpretation is reinforced by the fact that the coalescence time is the smallest at the highest concentration (Figure 4.11).

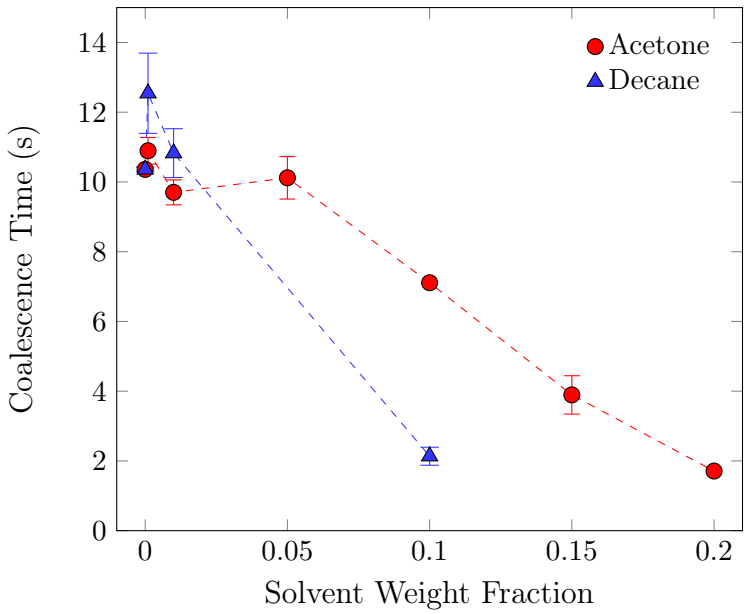

Figure 4.11: Time elapsed from the first visible interference color until bubble coalescence as a function of solvent weight fraction.

4.3.6 Viscosification effect evaluation

The actual viscosity of silicone-solvent mixtures is found by fitting the exponential portion of the data to Equation 4.8, keeping a slope of $-1/3$. The viscosities are compared to the initial ones in Figure 4.15, confirming the previous findings, of a film viscosification due to solvent evaporation. It is evident how the viscosity of silicone-solvent mixtures provided by the DFI data fitting is bigger than the viscosity of the same mixture measured with the rheometer without evaporation, especially for acetone trials.

4.3.7 Bulk foam experiments

The foamability of different silicone oil mixtures has been evaluated by measuring the rise in volume while bubbling the mixtures with air, as described in Section 4.2.4. The results for two silicone oil-acetone mixtures and three pure silicone oils are shown in Figure 4.16. Concerning the

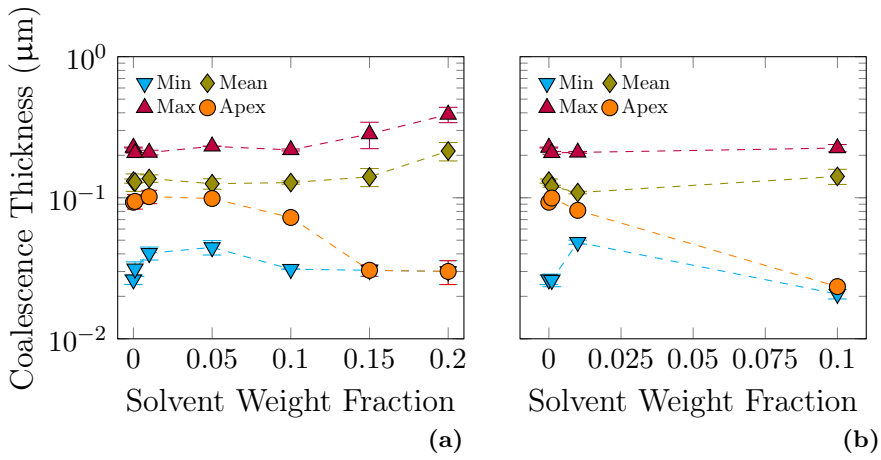

Figure 4.12: (4.12a and 4.12b) Maximum, mean, minimum, and center thicknesses at the last frame before bubble coalescence as a function of acetone and decane weight fraction, respectively.

pure silicone oils, the increase in volume is more significant for the low viscous ones (40 and 25 cSt), whereas it is less pronounced for the 100 cSt. Nearly a volume doubling occurs in ten seconds for low-viscosity silicone oils, while it takes ten times longer for high-viscosity silicone oil. The experiments with silicone oil-acetone mixtures suggest that acetone inhibits foam growth, keeping the total volume very close to the initial one for the whole duration of the experiment. The reasons behind these results will be examined and discussed in Section 4.3.8.

4.3.8 Comparison of bulk foam and single bubble behavior

In addition to using DFI data to clarify the physics of draining thin films in binary mixtures, it is possible to give them a twofold significance, with both fundamental and practical implications. As mentioned above, one of the research questions behind this investigation is if there is a correlation between bulk foam volume and single-bubble film drainage for the binary mixtures under examination. To test the consistency in predicting bulk foam behavior with DFI experiments, the foamability of silicone oil-acetone mixtures has been evaluated with a foam analyzer.

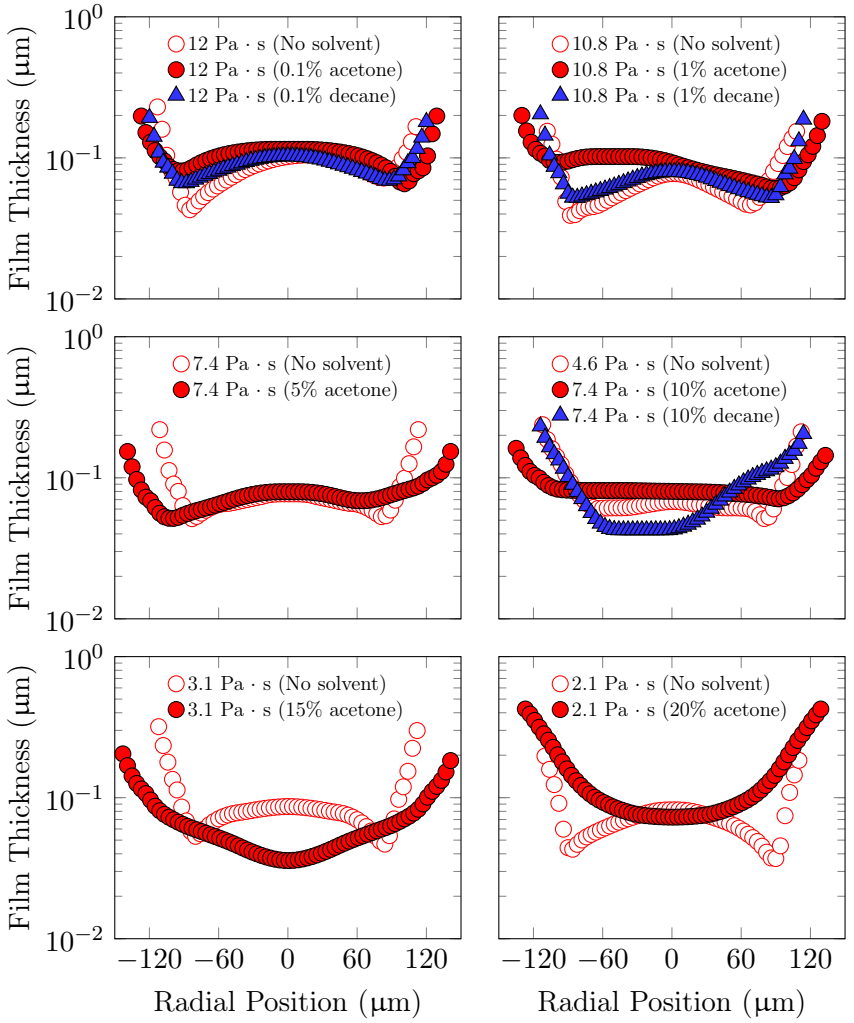

Figure 4.13: Film thickness profiles at the centerline just before bubble coalescence. Each plot shows profiles for different solvent concentrations and for pure silicone oils with the same viscosity as the mixture with solvent.

Unfortunately, it was not possible to compare bulk foam experiments with single bubble experiments for the same mixtures because of the inability to generate small bubbles in the high-viscosity silicone oils with

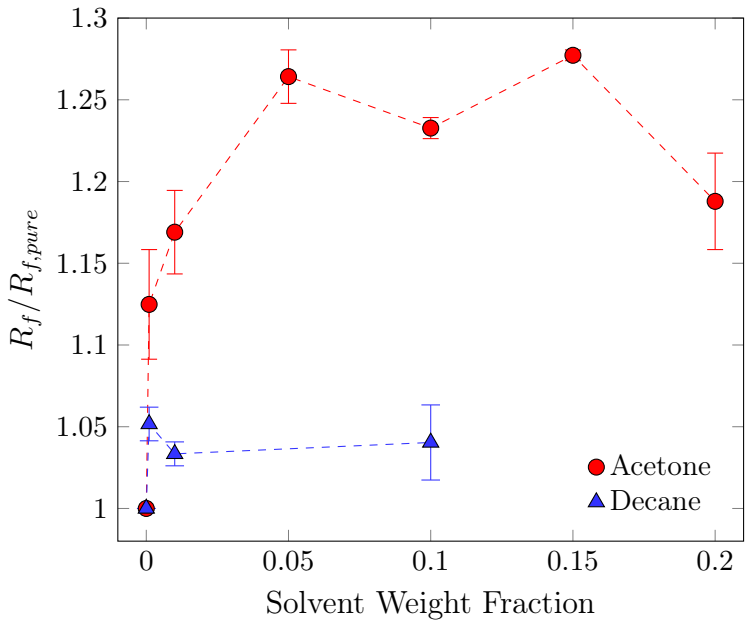

Figure 4.14: Film radius normalized by the pure silicone oil film radius as a function of solvent weight fraction.

out setup. The difficulties in generating a foam stem from the long time it takes for a bubble to rise in a highly viscous liquid. The bubbles tend to coalesce on the sparger at the bottom of the column, forming a huge bubble that rises very quickly and eventually bursts. However, since this study aims to assess the relative importance of viscosity and surface tension on thin film drainage and foam stability, it is no doubt of interest to measure these properties for low-viscosity fluids. The addition of acetone to low-viscosity silicone oil induces a significant decrease in viscosity and a slight increase in surface tension, as is the case with higher-viscosity oils.

First, the average volume normalized by the initial liquid volume of different foamed mixtures is shown in Figure 4.17. The results concerning the pure silicone oils indicate that the mean volume decreases with increasing viscosity. Whereas the silicone oil-acetone mixtures exhibit the lowest volumes with quite similar values. Notably, in the latter case, the average volume is virtually equal to the initial volume, indicating the difficulty of

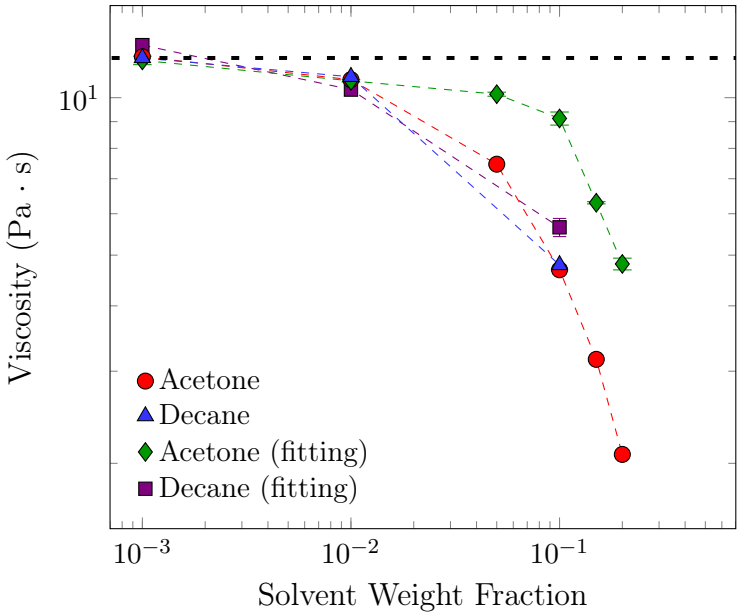

Figure 4.15: Comparison between viscosity isotherms for silicone oil 10000 cSt mixtures, and viscosities obtained by fitting the exponential decay (Equation 4.8) to drainage data. Horizontal dashed line represents the viscosity of pure 10000 cSt silicone oil.

generating stable foam.

To test the consistency in predicting bulk foam behavior with DFI experiments, the single bubble coalescence time t_d scaled by viscocapillary time is reported as a function of the initial viscosity of the mixture in Figure 4.18. The data clearly show that bubble coalescence occurs more rapidly in the presence of a solvent than with pure silicone oil, regardless of viscosity. This has been attributed to mass-loss due to solvent evaporation that causes an early coalescence of bubbles.

On the other hand, pure silicone oil bubbles coalesce faster by increasing viscosity. This was justified by thermal Marangoni flows caused by air circulation on the liquid surface (Section 4.3.2). Figure 4.18 shows that the bubble coalescence time is less with a closed chamber than with an open one for pure silicone oil. This confirms the previous explanation since thermal Marangoni flows should be weakened by the presence of the

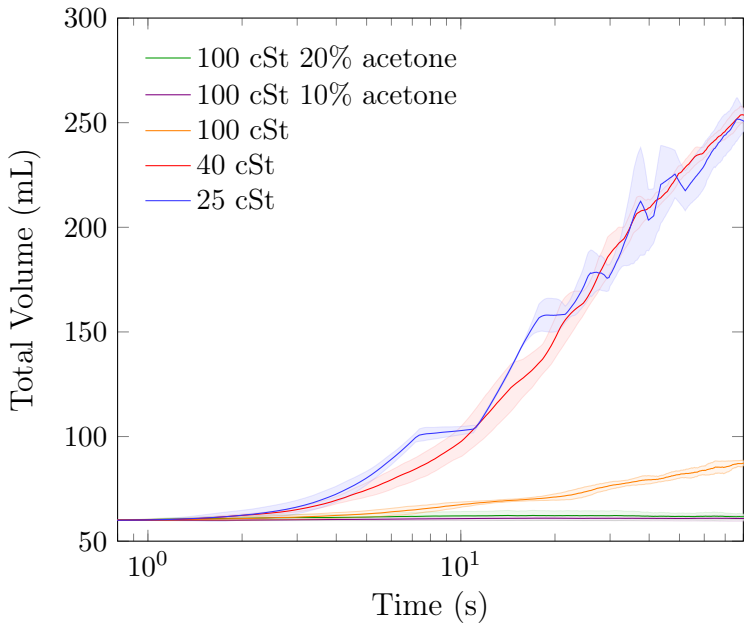

.

Figure 4.16: Total volume evolution measured from bulk foam experiments. The liquid has an initial volume of 60 mL, and it was maintained under continuous bubbling at 0.5 L/min

lid.

The results of bulk foam experiments with pure silicone oils can be interpreted by considering the same mechanism controlling single bubble coalescence. Ambient air circulation may be responsible for the thermal gradients on the surface of the foam, slowing down liquid drainage. On the other hand, solvent evaporation may be responsible for the scarce foamability in the presence of acetone shown in Figure 4.16. Remarkably, the tendency for acetone to destabilize the bubbles, and the presence of thermal Marangoni flows are revealed by both single bubble and bulk foam experiments, confirming that there exists a strong correlation between the two investigations.

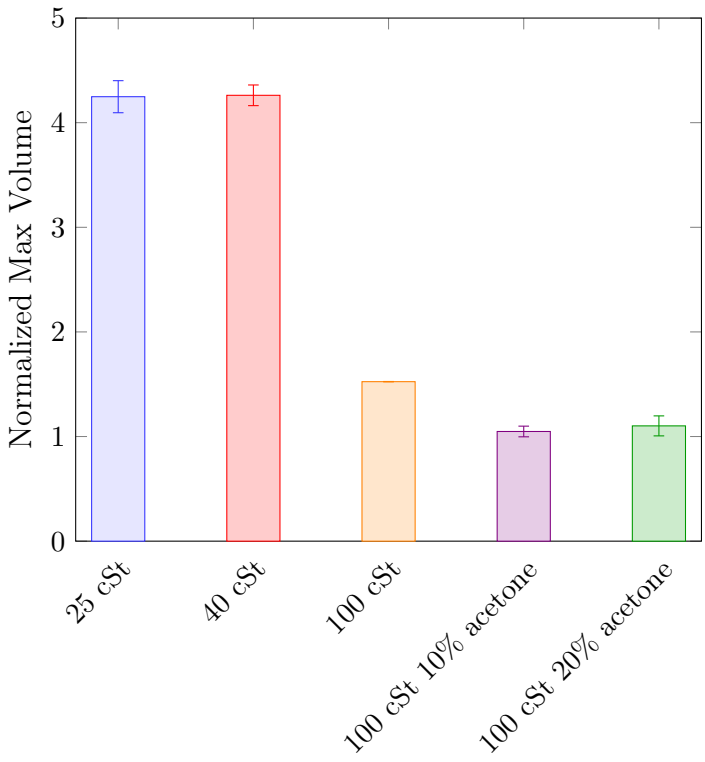

Figure 4.17: Mean volume normalized by the initial liquid volume, of the bubbling solution during bulk foam experiments. Note that the initial volume is the same for each measurement and, it is equal to 60 mL.

4.3.9 Acetone evaporation from bulk foam

The volume of a mixture of silicone oil 100 cSt-20% acetone was recorded for 8 hours of continuous bubbling to measure the evaporation time of acetone from a foaming mixture. Data shown in Figure 4.19 indicate that foam growth is almost inhibited by the presence of acetone for the first hour, the reason for which has already been discussed in Section 4.3.8. Only a slight froth formation is noticeable during this time frame, increasing the total volume by about 4 mL. The notable drop in foam volume is due to the evaporation of a considerable amount of acetone during the

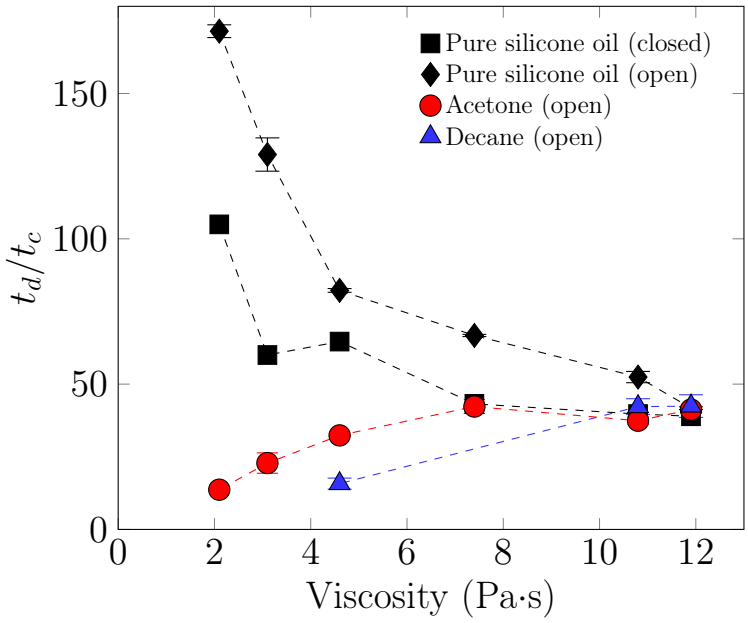

Figure 4.18: Single bubble coalescence time scaled by viscocapillary time as a function of initial viscosity of the mixture for pure silicone oils and in the presence of solvents, for closed and open chamber configurations. Note that this time for acetone and decane, viscocapillary time is computed with the viscosity obtained through fitting (Figure 4.15).

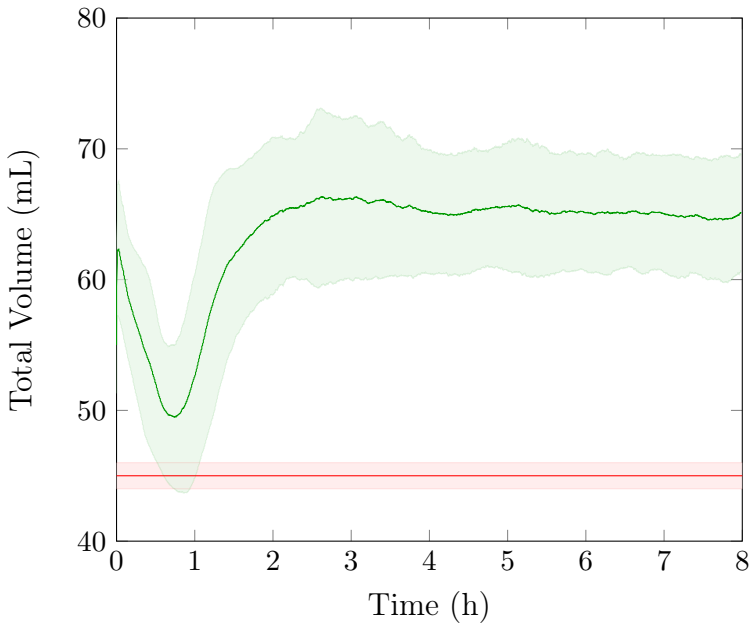

Figure 4.19: Total volume of the silicone oil 100 cSt-20% acetone mixture during 8 hours of continuous bubbling. The initial volume of liquid is equal to 60 mL (about 45 mL of pure silicone oil) and the air flow rate is 50 L/min. The red line corresponds to the liquid volume once the bubbling is stopped after 8 hours.

first hour.

The foam starts growing again in the second hour, suggesting that the acetone concentration has decreased significantly. Assuming that the 4 mL increase in total volume due to foam formation is constant in the first hour, it is possible to estimate the amount of acetone in the mixture when the volume is minimal (Figure 4.19). Considering the initial volume of liquid and the variation of silicone oil density with acetone concentration, we estimated the presence of about 4% acetone at this point. This value falls in the vicinity of the maximum in minimum film thickness shown in Figure 4.12a, meaning that the concentration range in which a single bubble is stable or unstable is the same for a bulk foam. This insight significantly increases the predictive capabilities of single bubble experiments on bulk

foam behavior.

After 2 hours of foaming, there is no significant change in the volume of the mixture, suggesting that the acetone has completely evaporated. To further confirm no acetone is left after 8 hours of bubbling, the final liquid volume without bubbles is shown in Figure 4.19. The final volume of the liquid is about 45 mL and is the same as the pure silicone oil used to prepare the mixture.

4.4 Conclusions

We assessed the effect of solvent evaporation on the film drainage of bubbles in binary mixtures, showing a viscosification effect that slows down the film evolution. Two solvents with different volatilities have been compared showing two different behaviors, and to further confirm our initial hypothesis we suppressed evaporation by closing the chamber.

We found that in the case of pure silicone oil, thin-film drainage appears to be affected by interfacial stresses, probably due to thermal Marangoni flows induced by air flows above the bubble. Interestingly, the presence of a solvent seems to inhibit film stabilization inducing an early bubble coalescence because of evaporative mass loss of the solvent from the film. On the other hand, film viscosification significantly impacts drainage dynamics at early times because of solvent evaporation from the liquid surface before the bubble approaches the air-liquid interface. This interpretation was confirmed by changing solvent volatility or suppressing evaporation with a closed chamber. These findings are in excellent agreement with scaling relations provided by lubrication theory.

To test the predictive capability of single film measurements on complete foams, we evaluated the foamability of mixtures containing silicone oil and acetone. The pure silicone oils showed increased foaming capacities by decreasing viscosity, while the presence of acetone completely counters foam growth. As for single-bubble coalescence, these behaviors can be attributed mainly to thermal Marangoni flows and evaporative mass-loss of solvent. Such a strong correlation is confirmed by several characteristics of thin films, including coalescence time and film thickness at coalescence, which explain the results of the bulk foam experiments.

The acetone evaporation time from a foaming silicone oil-acetone mix-

ture has been evaluated bubbling the mixture for 8 hours continuously. It has been found the acetone takes approximately 2 hours to evaporate. This result is certainly relevant for polymer processing industry where mixture properties may vary significantly during operations. In bubble columns or polymer devolatilization, it is vital to control the foam level constantly to avoid undesirable conditions such as overflow or flooding. This additional insight can be helpful for the design of such equipment.

Our findings suggest that viscosification and evaporative mass loss are the dominant mechanisms for bubble stabilization in mixtures with volatile compounds. Thermal and solutocapillary Marangoni flows appear negligible compared with the other two mechanisms in thin film stabilization in the presence of volatile compounds. Further research may be devoted to developing a more comprehensive model describing films containing volatiles, considering time-dependent concentration and viscosity and including evaporative mass loss and cooling. Questions persists, on the importance of thermal and solutocapillary Marangoni flows in the presence of volatile solvents.

In light of these findings, the DFI is confirmed as a reliable experimental technique for studying the interfacial rheology of multiphase systems. We believe that our analysis may contribute to understanding the interfacial properties of these systems from a fundamental standpoint and give more practical insights into polymer-solvent mixtures. However, it is worth mentioning that the system under investigation is a model system that includes a Newtonian fluid. Polymers processed in industrial applications exhibit viscoelastic behavior that is certainly relevant in the extensional deformation caused by the rise of bubbles against the air-liquid interface.

Because trends in foam levels coincide with differences observed in DFI experiments, this corroborates how simple single bubble experiments using interferometry can be extremely useful for formulation purposes. Adding multiple solvents with different volatilities or heat of vaporization may produce unexpected foam properties, which can be revealed by the investigation of individual bubbles. The scrutiny of these conditions is underway.

Chapter 5

Conclusions

This work aims to understand the working principle of a static DV, improve its separation capabilities, and present innovative design solutions. This has been successfully accomplished by the design and construction of a novel laboratory-scale devolatilization apparatus. The presented equipment has demonstrated to be a powerful tool to obtain measurements that are not possible in any other existing device. Observations from devolatilization experiments have shown that the efficiency of the process is directly related to SH and the time at which bubble nucleation begins. The experimental results and scaling provided may be of great interest for future work aimed at designing large-scale static devolatilizers and improving the accuracy of theoretical models.

In addition to performing devolatilization experiments, the mixture thermodynamics and mass transport properties of a POE/n-hexane system were studied experimentally and interpreted theoretically, given the considerable interest in defining processing conditions for this class of thermoplastic elastomers commonly found in devolatilization processes. Experimental results related to adsorption equilibrium and gas diffusion in a polymer are also valuable because little experimental data are available in the literature. The NRLF has been shown to accurately describe absorption isotherms for systems involving copolymers, producing an excellent fitting of experimental results at different temperatures.

As stated in the introduction of this dissertation, another goal of the work was to shed light on the mechanism that leads to foam stabilization in

binary mixtures composed of polymers and volatile components. This was accomplished by producing a large amount of liquid film drainage data at the bubble-air interface with newly developed DFI equipment. It has been demonstrated how single bubble experiments can accurately predict bulk foam behavior for complex systems of this kind, provide new quantitative detail on the mechanisms of thin film drainage in polymer-volatile blends, such as the impact of solvent on film size, shape, and coalescence time. From a practical point of view, the proposed foam stabilization mechanisms due to the presence of volatiles directly impact the devolatilization process optimization since foam stability is strongly related to removal efficiency. On the other hand, the previous analysis can contribute to the understanding of the interfacial properties of these systems from a fundamental point of view and provide practical insights into polymer-solvent mixtures, hopefully helping future researchers. These results open many research opportunities, such as adding multiple solvents with different volatilities or heat of vaporization that could produce unexpected foam properties.

Those offered in these conclusions are just a few examples of the many possibilities for future work in this field. It is my hope, as the author of this dissertation, that the work presented here may be of some help to future researchers.

Bibliography

[1] R J Albalak, E W Merrill, J M Zielinski, J L Duda, A V Yazdi, E J Beckman, M Favelukis, S.-T. Lee, A Tukachinsky, T Chechik, Y Talmon, and Z Tadmor. *Polymer Devolatilization*. Marcel Dekker Inc., New York, 1996.

[2] Costas G Gogos and Zehev Tadmor. *Principles of polymer processing*. John Wiley & Sons, 2013.

[3] UN. Geneva Protocol concerning the control of emissions of volatile organic compounds, 11 1991. URL https://unece.org/sites/default/files/2021-10/1991.VOC_.e.pdf.

[4] UN. Protocol of Kyoto, 12 1997. URL https://unfccc.int/sites/default/files/resource/docs/cop3/l07a01.pdf.

[5] EU. Limitation of emissions of volatile organic compounds due to the use of organic solvents in certain activities and installations, 3 1999. URL https://eur-lex.europa.eu/legal-content/EN/TXT/PDF/?uri=CELEX:31999L0013&from=EN.

[6] EU. National emission ceiling for certain atmospheric pollutants, 10 2001. URL https://eur-lex.europa.eu/legal-content/EN/TXT/PDF/?uri=CELEX:32001L0081&from=EN.

[7] EU. Limitation of emissions of volatile organic compounds due to the use of organic solvents in certain paints and varnishes and vehicle refinishing products and amendi, 4 2004. URL https://eur-lex.europa.eu/legal-content/EN/TXT/PDF/?uri=CELEX:32004L0042&from=EN.

[8] EU. Registration, Evaluation, Authorisation and Restriction of Chemicals (REACH), 12 2006. URL https://eur-lex.europa.eu/legal-content/EN/TXT/PDF/?uri=CELEX:32006R1907&from=IT.

[9] UN. Paris Agreement, 4 2016. URL https://unfccc.int/sites/default/files/english_paris_agreement.pdf.

[10] Edward L. Baker. A Review of Recent Research on Health Effects of Human Occupational Exposure to Organic Solvents: A Critical Review. *Journal of Occupational Medicine*, 36(10):1079–1092, 10 1994.

[11] M.O. Rodrigues, N. Abrantes, F.J.M. Gonçalves, H. Nogueira, J.C. Marques, and A.M.M. Gonçalves. Impacts of plastic products used in daily life on the environment and human health: What is known? *Environmental Toxicology and Pharmacology*, 72:103239, 11 2019. ISSN 13826689. doi: 10.1016/j.etap.2019.103239.

[12] Yoshinori Kamiya, Takuji Hirose, Keishin Mizoguchi, and Yasutoshi Naito. Gravimetric study of high-pressure sorption of gases in polymers. *Journal of Polymer Science Part B: Polymer Physics*, 24(7):1525–1539, 7 1986. ISSN 08876266. doi: 10.1002/polb.1986.090240711.

[13] Timothy Merkel, V I Bondar, K Nagai, B D Freeman, and I Pinnau. Gas Sorption, Diffusion, and Permeation in Poly(dimethylsiloxane). *Journal of Polymer Science: Part B: Polymer Physics*, 38:415–434, 2000.

[14] Joseph A. Biesenberger and Shau-Tarng Lee. A fundamental study of polymer melt devolatilization. Part I: Some experiments on foam-enhanced devolatilization. *Polymer Engineering and Science*, 26(14):982–988, 8 1986. ISSN 0032-3888. doi: 10.1002/pen.760261404.

[15] J A Biesenberger and S T Lee. A Fundamental Study of Polymer Melt Devolatilization: II. A Theory of Foam-Enhanced DV. *Proceedings of the 44th ANTEC of SPE, Boston*, 846, 1986.

[16] Joseph A Biesenberger and Shau-Tarng -T Lee. A fundamental study of polymer melt devolatilization: III More experiments on foam-enhanced DV. *Polymer Engineering & Science*, 27(7):510–517, 1987. ISSN 15482634. doi: 10.1002/pen.760270706.

[17] S. T. Lee and J. A. Biesenberger. A fundamental study of polymer melt devolatilization. IV: Some theories and models for foam-enhanced devolatilization. *Polymer Engineering and Science*, 29(12):782–790, 6 1989. ISSN 0032-3888. doi: 10.1002/pen.760291206.

[18] Alicia De San Luis, Catherine C Santini, Yvan Chalamet, and Véronique Dufaud. Removal of Volatile Organic Compounds from Bulk and Emulsion Polymers: A Comprehensive Survey of the Existing Techniques. *Industrial and Engineering Chemistry Research*, 58(27):11601–11623, 2019. ISSN 15205045. doi: 10.1021/acs.iecr.9b00968.

[19] Yan Bin Li, Wei Liu, Xia Zhang, Bao Chang Sun, Yong Luo, and Guang Wen Chu. Enhancement of devolatilization performance in a rotating packed bed with different packing structures. *Separation and Purification Technology*, 278(June 2021):119527, 2022. ISSN 18733794. doi: 10.1016/j.seppur.2021.119527. URL https://doi.org/10.1016/j.seppur.2021.119527.

[20] Junhao Wang, Hao Fu, Haibing Ding, Yufeng Qian, Zhipeng Li, Zhengming Gao, and J J Derksen. Film formation and surface renewal on a rotating spoked disk for polymer devolatilization. *Chemical Engineering Research and Design*, 170:45–53, 2021. ISSN 02638762. doi: 10.1016/j.cherd.2021.03.030. URL https://doi.org/10.1016/j.cherd.2021.03.030.

[21] Wenkai Cheng, Jiajun Wang, Xueping Gu, and Lianfang Feng. Film flow on rotating wheel in a horizontal twin-shaft reactor for polymer devolatilization. *Chemical Engineering Science*, 191:468–478, 2018. ISSN 00092509. doi: 10.1016/j.ces.2018.07.011. URL https://doi.org/10.1016/j.ces.2018.07.011.

[22] R H M Simon. Falling-Strand Devolatilization. In *Polymer Devolatilization*, chapter 9, pages 261–290. Marcel Dekker Inc., New York, 1996.

[23] R J Albalak, Z Tadmor, and Y Talmon. Scanning electron microscopy studies of polymer melt devolatilization. *AIChE Journal*, 33(5):808–818, 1987. ISSN 15475905. doi: 10.1002/aic.690330514.

[24] Ramon J Albalak, Zehev Tadmor, and Yeshayahu Talmon. Polymer melt devolatilization mechanisms. *AIChE Journal*, 36(9):1313–1320, 1990. ISSN 15475905. doi: 10.1002/aic.690360904.

[25] K T O'Brien. Devolatilisation. In A Whelan and J L Craft, editors, *Developments in Plastics Technology*, chapter Devolatili, pages 47–86. Elsevier, London, 1985. ISBN 9789401083584.

[26] Stefan Hirschfeld, Lutz Hermann, and Olaf Wünsch. Polymer Devolatilization in a Rotating Apparatus. *Pamm*, 15(1):511–512, 2015. doi: 10.1002/pamm.201510246.

[27] Rafael Salazar, Pedro Ilundain, Daniel Alvarez, Louis Da Cunha, María J. Barandiaran, and José M. Asua. Reduction of the Residual Monomer and Volatile Organic Compounds by Devolatilization. *Industrial & Engineering Chemistry Research*, 44(11):4042–4050, 5 2005. ISSN 0888-5885. doi: 10.1021/ie050151g.

[28] G. M. Bristow and W. F. Watson. Cohesive energy densities of polymers. Part 1.—Cohesive energy densities of rubbers by swelling measurements. *Trans. Faraday Soc.*, 54(0):1731–1741, 1958. ISSN 0014-7672. doi: 10.1039/TF9585401731.

[29] G. M. Bristow and W. F. Watson. Cohesive energy densities of polymers. Part 2.—Cohesive energy densities from viscosity measurements. *Trans. Faraday Soc.*, 54(0):1742–1747, 1958. ISSN 0014-7672. doi: 10.1039/TF9585401742.

[30] J. S. Vrentas and J. L. Duda. Diffusion in polymer—solvent systems. I. Reexamination of the free-volume theory. *Journal of Polymer Science: Polymer Physics Edition*, 15(3):403–416, 3 1977. ISSN 00981273. doi: 10.1002/pol.1977.180150302.

[31] J. S. Vrentas and J. L. Duda. Diffusion in polymer–solvent systems. II. A predictive theory for the dependence of diffusion coefficients on temperature, concentration, and molecular weight. *Journal of Polymer Science: Polymer Physics Edition*, 15(3):417–439, 3 1977. ISSN 00981273. doi: 10.1002/pol.1977.180150303.

[32] J L Duda and John M Zielinski. Free-volume theory. In *Diffusion in Polymers*, volume 32, pages 143–171. Marcel Dekker Inc., 1996.

[33] Morrel H. Cohen and David Turnbull. Molecular Transport in Liquids and Glasses. *The Journal of Chemical Physics*, 31(5):1164–1169, 11 1959. ISSN 0021-9606. doi: 10.1063/1.1730566.

[34] Berry G. C. and Fox T. G. The viscosity of polymers and their concentrated solutions. In *Advances in Polymer Science*, volume 5/3, pages 261–357. Springer Berlin Heidelberg, Berlin, Heidelberg, 1968. ISBN 978-3-540-35769-8.

[35] I Gestring and D Mewes. Degassing of molten polymers. *Chemical Engineering Science*, 57(16):3415–3426, 2002. ISSN 00092509. doi: 10.1016/S0009-2509(02)00207-5.

[36] George A Latinen. Devolatilization of Viscous Polymer Systems. pages 235–246, 1962. doi: 10.1021/ba-1962-0034.ch019.

[37] George W. Roberts. A surface renewal model for the drying of polymers during screw extrusion. *AIChE Journal*, 16(5):878–882, 9 1970. ISSN 0001-1541. doi: 10.1002/aic.690160530.

[38] R. W. Coughlin and G. P. Canevari. Drying polymers during screw extrusion. *AIChE Journal*, 15(4):560–564, 7 1969. ISSN 0001-1541. doi: 10.1002/aic.690150416.

[39] David B. Todd. Residence time distribution in twin-screw extruders. *Polymer Engineering and Science*, 15(6):437–443, 6 1975. ISSN 0032-3888. doi: 10.1002/pen.760150607.

[40] G. P. Collins, C. D. Denson, and G. Astarita. Determination of mass transfer coefficients for bubble-free devolatilization of polymeric solutions in twin-screw extruders. *AIChE Journal*, 31(8):1288–1296, 8 1985. ISSN 0001-1541. doi: 10.1002/aic.690310807.

[41] K G Powell and C D Denson. A model for the devolatilization of polymeric solutions containing entrained bubbles. *75th Ann. Meet. of the American Institute of Chemical Engineers Washington DC*, 1983.

[42] Joseph A. Biesenberger. Polymer devolatilization: Theory of equipment. *Polymer Engineering and Science*, 20(15):1015–1022, 10 1980. ISSN 0032-3888. doi: 10.1002/pen.760201506.

[43] Joseph A Biesenberger. Polymer melt devolatilization: On equipment design equations. *Advances in Polymer Technology*, 7(3):267–278, 1987. ISSN 10982329. doi: 10.1002/adv.1987.060070304.

[44] Milton Blander and Joseph L. Katz. Bubble Nucleation in Liquids. *AIChE Journal*, 21(5):833–848, 1975. doi: https://doi.org/10.1002/aic.690210502.

[45] L.E. Scriven. On the dynamics of phase growth. *Chemical Engineering Science*, 10(1-2):1–13, 4 1959. ISSN 00092509. doi: 10.1016/0009-2509(59)80019-1.

[46] E. J. Barlow and W. E. Langlois. Diffusion of Gas from a Liquid into an Expanding Bubble. *IBM Journal of Research and Development*, 6(3):329–337, 7 1962. ISSN 0018-8646. doi: 10.1147/rd.63.0329.

[47] J. L. Duda, J. S. Vrentas, S. T. Ju, and H. T. Liu. Prediction of diffusion coefficients for polymer-solvent systems. *AIChE Journal*, 28(2):279–285, 3 1982. ISSN 0001-1541. doi: 10.1002/aic.690280217.

[48] K. Ravindranath and R.A. Mashelkar. Analysis of the role of stripping agents in polymer devolatilization. *Chemical Engineering Science*, 43(3): 429–442, 1988. ISSN 00092509. doi: 10.1016/0009-2509(88)87003-9.

[49] Joseph A Biesenberger and Donald H Sebastian. Principles of Polymerization Engineering. In *Princ of Polym Eng*. John Wiley & Sons, 1983.

[50] J. S. Vrentas, J. L. Duda, and H.-C. Ling. Enhancement of impurity removal from polymer films. *Journal of Applied Polymer Science*, 30(12):4499–4516, 12 1985. ISSN 00218995. doi: 10.1002/app.1985.070301201.

[51] C. C. Chen. A Continuous Bulk Polymerization Process for Crystal Polystyrene. *Polymer-Plastics Technology and Engineering*, 33(1):55–81, 1 1994. ISSN 0360-2559. doi: 10.1080/03602559408010731.

[52] Bruce Allan Ashby. Continuous devolatilization of silanol-terminated silicone polymer, 1978.

[53] R H M Simon. 'Flash Evaporators and Falling Strand Devolatilizers. *Devolatilization of Polymers, JA Biesenberger, Ed., Hanser, Munich*, 1983.

[54] William B Glover. Selecting evaporators for process applications. *Chemical engineering progress*, 100(12):26–33, 2004.

[55] Randolph E. Newman. Falling strand devolatilizer, 1981.

[56] Timothy F. McKenna. Design model of a wiped film evaporator. Applications to the devolatilisation of polymer melts. *Chemical Engineering Science*, 50(3):453–467, 2 1995. ISSN 00092509. doi: 10.1016/0009-2509(94)00257-R.

[57] Joseph A Biesenberger and G Kessidis. Devolatilization of polymer melts in single-screw extruders. *Polymer Engineering & Science*, 22(13):832–835, 1982.

[58] Zehev Tadmor, Pradip S Mehta, Lefteris N Valsamis, and Jan Chin Yang. Corotating disk pumps for viscous liquids. *Industrial & Engineering Chemistry Process Design and Development*, 24(2):311–320, 1985.

[59] Lefteris N Valsamis and Gary S Donoian. The DISKPACK plastics compounder. *Advances in Polymer Technology: Journal of the Polymer Processing Institute*, 4(2):131–146, 1984.

[60] L N Valsamis and Z Tadmor. Mixing in Corotating Disk. *Mixing in Polymer Processing*, 23:405, 1991.

[61] Pradip S Mehta and Gary S Donoian. Heat-transfer characteristics of a rotary disk processor. *Industrial & engineering chemistry research*, 29(5): 829–841, 1990.

[62] Franz Wenzel, Heinz-Dieter Bruemmer, and Manfred Krieg. Acrylonitrile copolymers having low residual monomer content and methods for their preparation, 12 1980.

[63] Varun Ullal and Douglas E Spearot. Molecular dynamics simulation of O2 diffusion in polydimethylsiloxane (PDMS) and end-linked PDMS networks. *Molecular Simulation*, 40(12):976–986, 2014. ISSN 10290435. doi: 10.1080/08927022.2013.830183.

[64] Daniele Tammaro, Lorenzo Lombardi, Giuseppe Scherillo, Ernesto Di Maio, Navanshu Ahuja, and Giuseppe Mensitieri. Modelling Sorption Thermodynamics and Mass Transport of n-Hexane in a Propylene-Ethylene Elastomer. *Polymers*, 13(7):1157, 2021. ISSN 20734360. doi: 10.3390/polym13071157.

[65] R E McMillen and F A Streiff. Assembly of crossing elements and method of constructing same - CA2491755C, 2010.

[66] Joseph R Stetter and Jing Li. Amperometric gas sensors - A review. *Chemical Reviews*, 108(2):352–366, 2008. ISSN 00092665. doi: 10.1021/cr0681039.

[67] Steven Lubetkin and Mark Blackwell. The Nucleation of Bubbles in Supersaturated Solutions. *Journal of Colloid and Interface Science*, 26(2), 1988.

[68] James H Han and Han Chang Dae. A Study of Bubble Nucleation in a Mixture of Molten Polymer and Volatile Liquid in a Shear Flow Field. *Polymer Engineering and Science*, 28(24), 1988.

[69] Lee Chen, Xiang Wang, Rich Straff, and Kent Blizard. Shear Stress Nucleation in Microcellular Foaming Process. *Polymer Engineering and Science*, 42(6), 2002.

[70] A. Wong and C. B. Park. A visualization system for observing plastic foaming processes under shear stress. *Polymer Testing*, 31(3):417–424, 5 2012. ISSN 01429418. doi: 10.1016/j.polymertesting.2011.12.012.

[71] Moris Amon and Costel D Denson. A study of the dynamics of foam growth: Analysis of the growth of closely spaced spherical bubbles. *Polymer Engineering & Science*, 24(13):1026–1034, 1984. ISSN 15482634. doi: 10.1002/pen.760241306.

[72] Moshe Favelukis, Zehev Tadmor, and Raphael Semiat. Bubble growth in a viscous liquid in a simple shear flow. *AIChE Journal*, 45(4):691–695, 1999. ISSN 00011541. doi: 10.1002/aic.690450404.

[73] Liaofei Yin and Li Jia. Confined bubble growth and heat transfer characteristics during flow boiling in microchannel. *International Journal of Heat and Mass Transfer*, 98:114–123, 7 2016. ISSN 00179310. doi: 10.1016/j.ijheatmasstransfer.2016.02.063.

[74] Glenn O Brown. The History of the Darcy-Weisbach Equation for Pipe Flow Resistance. *Environmental and Water Resources History*, pages 34–43, 2003.

[75] Élise Lorenceau, David Quéré, and Jens Eggers. Air entrainment by a viscous jet plunging into a bath. *Physical Review Letters*, 93(25), 12 2004. ISSN 00319007. doi: 10.1103/PhysRevLett.93.254501.

[76] Hossein Hosseini, Ali Farnudi, Mohammad Hassan Khatami, and Mehdi Habibi. Bubble generation in liquid rope coiling. *RSC Advances*, 6(107):105469–105475, 2016. ISSN 20462069. doi: 10.1039/c6ra23012a.

[77] Ahmad Shamiri, Mohammed Chakrabarti, Shah Jahan, Mohd Hussain, Walter Kaminsky, Purushothaman Aravind, and Wageeh Yehye. The Influence of Ziegler-Natta and Metallocene Catalysts on Polyolefin Structure, Properties, and Processing Ability. *Materials*, 7(7):5069–5108, 7 2014. ISSN 1996-1944. doi: 10.3390/ma7075069.

[78] Xiangyang Song, Lixin Cao, Ryo Tanaka, Takeshi Shiono, and Zhengguo Cai. Optically Transparent Functional Polyolefin Elastomer with Excellent Mechanical and Thermal Properties. *ACS Macro Letters*, 8(3):299–303, 3 2019. ISSN 2161-1653. doi: 10.1021/acsmacrolett.9b00005.

[79] Daniele Tammaro, Salvatore Iannace, and Ernesto Di Maio. Insight into bubble nucleation at high-pressure drop rate. *Journal of Cellular Plastics*, 53(5):551–560, 9 2017. ISSN 0021-955X. doi: 10.1177/0021955X17695094.

[80] Aarón J. Cancelas, Miguel A. Plata, Muhammad Ahsan Bashir, Michael Bartke, Vincent Monteil, and Timothy F. L. McKenna. Solubility and Diffusivity of Propylene, Ethylene, and Propylene-Ethylene Mixtures in Polypropylene. *Macromolecular Chemistry and Physics*, 219(8):1700565, 4 2018. ISSN 10221352. doi: 10.1002/macp.201700565.

[81] E. W. Merrill. Thermodynamic Aspects of Devolatilization of Polymers. In *Polymer Devolatilization*, pages 13–34. Marcel Dekker Inc., New York, 1st edition, 1996.

[82] Jason K. Lee, Selina X. Yao, Guangming Li, Martin B. G. Jun, and Patrick C. Lee. Measurement Methods for Solubility and Diffusivity of Gases and Supercritical Fluids in Polymers and Its Applications. *Polymer Reviews*, 57(4):695–747, 10 2017. ISSN 1558-3724. doi: 10.1080/15583724.2017.1329209.

[83] J.P.G. Villaluenga, M. Khayet, M.A. López-Manchado, J.L. Valentin, B. Seoane, and J.I. Mengual. Gas transport properties of polypropylene/-clay composite membranes. *European Polymer Journal*, 43(4):1132–1143, 4 2007. ISSN 00143057. doi: 10.1016/j.eurpolymj.2007.01.018.

[84] Baochun Guo, Zhenghai Tang, and Liqun Zhang. Transport performance in novel elastomer nanocomposites: Mechanism, design and control. *Progress in Polymer Science*, 61:29–66, 10 2016. ISSN 00796700. doi: 10.1016/j.progpolymsci.2016.06.001.

[85] Edward Armand Guggenheim. *Mixtures: the theory of the equilibrium properties of some simple classes of mixtures, solutions and alloys*. Clarendon Press, 1952.

[86] Paul J Flory. *Principles of polymer chemistry*. Cornell university press, 1953.

[87] Isaac C. Sanchez and Robert H. Lacombe. An elementary molecular theory of classical fluids. Pure fluids. *The Journal of Physical Chemistry*, 80(21):2352–2362, 10 1976. ISSN 0022-3654. doi: 10.1021/j100562a008.

[88] Robert H. Lacombe and Isaac C. Sanchez. Statistical thermodynamics of fluid mixtures. *The Journal of Physical Chemistry*, 80(23):2568–2580, 11 1976. ISSN 0022-3654. doi: 10.1021/j100564a009.

[89] Isaac C. Sanchez and Robert H. Lacombe. Statistical Thermodynamics of Polymer Solutions. *Macromolecules*, 11(6):1145–1156, 11 1978. ISSN 0024-9297. doi: 10.1021/ma60066a017.

[90] Constantinos G. Panayiotou. Thermodynamics of alkanol-alkane mixtures. *The Journal of Physical Chemistry*, 92(10):2960–2969, 5 1988. ISSN 0022-3654. doi: 10.1021/j100321a048.

[91] Masoud Taimoori and Costas Panayiotou. The non-random distribution of free volume in fluids: polydisperse polymer systems. *Fluid Phase Equilibria*, 205(2):249–265, 4 2003. ISSN 03783812. doi: 10.1016/S0378-3812(02)00294-7.

[92] Costas Panayiotou. The QCHB model of fluids and their mixtures. *The Journal of Chemical Thermodynamics*, 35(2):349–381, 2 2003. ISSN 00219614. doi: 10.1016/S0021-9614(02)00372-5.

[93] Costas Panayiotou, Maria Pantoula, Emmanuel Stefanis, Ioannis Tsivintzelis, and Ioannis G Economou. Nonrandom hydrogen-bonding model of fluids and their mixtures. 1. Pure fluids. *Industrial & engineering chemistry research*, 43(20):6592–6606, 2004.

[94] Costas Panayiotou, Ioannis Tsivintzelis, and Ioannis G. Economou. Nonrandom Hydrogen-Bonding Model of Fluids and Their Mixtures. 2. Multicomponent Mixtures. *Industrial & Engineering Chemistry Research*, 46(8):2628–2636, 4 2007. ISSN 0888-5885. doi: 10.1021/ie0612919.

[95] Costas Panayiotou. New expressions for non-randomness in equation-of-state models. *Fluid Phase Equilibria*, 237(1-2):130–139, 10 2005. ISSN 03783812. doi: 10.1016/j.fluid.2005.08.019.

[96] Costas G Panayiotou. Hydrogen bonding in solutions: the equation-of-state approach. *The Handbook of Surface and Colloid Chemistry*, pages 5–66, 2003.

[97] Costas G Panayiotou. Hydrogen bonding and nonrandomness in solution thermodynamics. *Handbook of Surface and Colloid Chemistry,*, pages 45–89, 2009.

[98] Giuseppe Mensitieri, Giuseppe Scherillo, Costas Panayiotou, and Pellegrino Musto. Towards a predictive thermodynamic description of sorption processes in polymers: The synergy between theoretical EoS models and vibrational spectroscopy. *Materials Science and Engineering: R: Reports*, 140:100525, 4 2020. ISSN 0927796X. doi: 10.1016/j.mser.2019.100525.

[99] Andreas Grenner, Ioannis Tsivintzelis, Ioannis G. Economou, Costas Panayiotou, and Georgios M. Kontogeorgis. Evaluation of the Nonrandom Hydrogen Bonding (NRHB) Theory and the Simplified Perturbed-ChainStatistical Associating Fluid Theory (sPC-SAFT). 1. VaporLiquid

Equilibria. *Industrial & Engineering Chemistry Research*, 47(15):5636–5650, 8 2008. ISSN 0888-5885. doi: 10.1021/ie071381t.

[100] Ioannis Tsivintzelis, Theodora Spyriouni, and Ioannis G. Economou. Modeling of fluid phase equilibria with two thermodynamic theories: Nonrandom hydrogen bonding (NRHB) and statistical associating fluid theory (SAFT). *Fluid Phase Equilibria*, 253(1):19–28, 4 2007. ISSN 03783812. doi: 10.1016/j.fluid.2007.01.008.

[101] Ioannis Tsivintzelis, Andreas Grenner, Ioannis G. Economou, and Georgios M. Kontogeorgis. Evaluation of the Nonrandom Hydrogen Bonding (NRHB) Theory and the Simplified Perturbed-ChainStatistical Associating Fluid Theory (sPC-SAFT). 2. LiquidLiquid Equilibria and Prediction of Monomer Fraction in Hydrogen Bonding Systems. *Industrial & Engineering Chemistry Research*, 47(15):5651–5659, 8 2008. ISSN 0888-5885. doi: 10.1021/ie071382l.

[102] Ioannis Tsivintzelis, Ioannis G. Economou, and Georgios M. Kontogeorgis. Modeling the solid-liquid equilibrium in pharmaceutical-solvent mixtures: Systems with complex hydrogen bonding behavior. *AIChE Journal*, 55(3): 756–770, 3 2009. ISSN 00011541. doi: 10.1002/aic.11716.

[103] Ioannis Tsivintzelis, Ioannis G. Economou, and Georgios M. Kontogeorgis. Modeling the Phase Behavior in Mixtures of Pharmaceuticals with Liquid or Supercritical Solvents. *The Journal of Physical Chemistry B*, 113(18): 6446–6458, 5 2009. ISSN 1520-6106. doi: 10.1021/jp807952v.

[104] Ioannis Tsivintzelis and Georgios M. Kontogeorgis. Modeling the vapor–liquid equilibria of polymer–solvent mixtures: Systems with complex hydrogen bonding behavior. *Fluid Phase Equilibria*, 280(1-2):100–109, 6 2009. ISSN 03783812. doi: 10.1016/j.fluid.2009.03.018.

[105] Costas Tsioptsias, Ioannis Tsivintzelis, and Costas Panayiotou. Equation-of-state modeling of mixtures with ionic liquids. *Physical Chemistry Chemical Physics*, 12(18):4843, 2010. ISSN 1463-9076. doi: 10.1039/c000208a.

[106] A. Fredenslund and M.J. Sorensen. Group Contribution Estimation Methods. In *Models for Thermodynamic and Phase Equilibria Calculations*, pages 287–362. Marcel Dekker Inc., New York, 1st edition, 1994.

[107] Geoffrey Sheard Park and John Crank. Diffusion in polymers. 1968.

[108] C A Coulson and J Crank. *The Mathematics of Diffusion*. Oxford University Press, Oxford, second edition, 1975. doi: 10.2307/3609455.

[109] Product Datasheet of VistamaxxTM Performance Polymer 8880 (Propylene Elastomer), 7 2020. URL http://exxonmobilchemical.ulprospector.com/datasheet.aspx?I=61702&E=114465&FMT=PDF.

[110] S.M. Wiederhorn, R.J Fields, S. Low, G.-W. Bahng, A. Wehrstedt, J. Hahn, Y. Tomota, T. Miyata, H. Lin, and B.D. Freeman. Experimental Measurement of Gas and Vapor Sorption. In *Springer Handbook of Metrology and Testing*, pages 438–439. Springer, Berlin/Heidelberg, 2nd edition, 2011.

[111] Angelica J. B. Francoeur, Hadiseh Karimi, Kim B. McAuley, and Luigi D'Agnillo. A model for the devolatilization of EPDM rubber in a series of steam stripping vessels. *AIChE Journal*, 60(7):2596–2606, 7 2014. ISSN 00011541. doi: 10.1002/aic.14448.

[112] Georgios M Kontogeorgis and Georgios K Folas. *Thermodynamic models for industrial applications: from classical and advanced mixing rules to association theories*. John Wiley & Sons, 2009.

[113] Ryan A. Krenz, Torben Laursen, and Robert A. Heidemann. The Modified SanchezLacombe Equation of State Applied to Polydisperse Polyethylene Solutions. *Industrial & Engineering Chemistry Research*, 48(23):10664–10681, 12 2009. ISSN 0888-5885. doi: 10.1021/ie801451a.

[114] C Panayiotou and J H Vera. Thermodynamics of Polymer–Polymer–Solvent and Block Copolymer–Solvent Systems II. Theoretical Treatment of Data with the Nonrandom New Flory Theory. *Polymer Journal*, 16(2):103–112, 2 1984. ISSN 0032-3896. doi: 10.1295/polymj.16.103.

[115] C. Panayiotou and F. Oehmke. Volumetric properties of random copolymers. An experimental and theoretical study. *Fluid Phase Equilibria*, 126(2):289–298, 12 1996. ISSN 03783812. doi: 10.1016/S0378-3812(96)03065-8.

[116] Joachim Gross and Gabriele Sadowski. Perturbed-Chain SAFT: An Equation of State Based on a Perturbation Theory for Chain Molecules. *Industrial & Engineering Chemistry Research*, 40(4):1244–1260, 2 2001. ISSN 0888-5885. doi: 10.1021/ie0003887.

[117] Joachim Gross, Oliver Spuhl, Feelly Tumakaka, and Gabriele Sadowski. Modeling Copolymer Systems Using the Perturbed-Chain SAFT Equation of State. *Industrial & Engineering Chemistry Research*, 42(6):1266–1274, 3 2003. ISSN 0888-5885. doi: 10.1021/ie020509y.

[118] Frank J. Matthews, James R. Fair, Joel W. Barlow, Donald R. Paul, and Charles Cozewith. Solvent removal from ethylene-propylene elastomers. 1. Determination of diffusion mechanism. *Industrial & Engineering Chemistry Product Research and Development*, 25(1):58–64, 3 1986. ISSN 0196-4321. doi: 10.1021/i300021a013.

[119] Laurier L Schramm and others. Fundamentals and applications in the petroleum Industry. *Adv. Chem*, 231:3–24, 1992.

[120] A. Etoc, F. Delvigne, J. P. Lecomte, and P. Thonart. Foam Control in Fermentation Bioprocess. In *Twenty-Seventh Symposium on Biotechnology for Fuels and Chemicals*, pages 392–404. Humana Press, Totowa, NJ, 2006. doi: 10.1007/978-1-59745-268-7{_}32.

[121] Akhilesh Kumar, T. E. Degaleesan, G. S. Laddha, and H. E. Hoelscher. Bubble swarm characteristics in bubble columns. *The Canadian Journal of Chemical Engineering*, 54(5):503–508, 10 1976. ISSN 00084034. doi: 10.1002/cjce.5450540525.

[122] Nigar Kantarci, Fahir Borak, and Kutlu O. Ulgen. Bubble column reactors. *Process Biochemistry*, 40(7):2263–2283, 6 2005. ISSN 13595113. doi: 10.1016/j.procbio.2004.10.004.

[123] Chi Tai Yang, Theodore G Smith, David I Bigio, and Colin Anolick. Polymer Trace Devolatilization: I. Foaming Experiments and Model Development. *AIChE Journal*, 43(7):1861–1873, 1997. ISSN 00011541. doi: 10.1002/aic.690430721.

[124] N. Barbian, E. Ventura-Medina, and J.J. Cilliers. Dynamic froth stability in froth flotation. *Minerals Engineering*, 16(11):1111–1116, 11 2003. ISSN 08926875. doi: 10.1016/j.mineng.2003.06.010.

[125] Maria Cristina Collivignarelli, Marco Baldi, Alessandro Abbà, Francesca Maria Caccamo, Marco Carnevale Miino, Elena Cristina Rada, and Vincenzo Torretta. Foams in Wastewater Treatment Plants: From Causes to Control Methods. *Applied Sciences*, 10(8):2716, 4 2020. ISSN 2076-3417. doi: 10.3390/app10082716.

[126] Juan M. Rodríguez Patino, Cecilio Carrera Sánchez, and Ma Rosario Rodríguez Niño. Implications of interfacial characteristics of food foaming agents in foam formulations. *Advances in Colloid and Interface Science*, 140(2):95–113, 8 2008. ISSN 00018686. doi: 10.1016/j.cis.2007.12.007.

[127] D. Evan Evans and Marian C. Sheehan. Don't be fobbed off: The substance of beer foam - A review. *Journal of the American Society of Brewing Chemists*, 60(2):47–57, 2002. ISSN 03610470. doi: 10.1094/asbcj-60-0047.

[128] Maryam Parsa, Anna Trybala, Danish Javed Malik, and Victor Starov. Foam in pharmaceutical and medical applications. *Current Opinion in Colloid & Interface Science*, 44:153–167, 12 2019. ISSN 13590294. doi: 10.1016/j.cocis.2019.10.007.

[129] V. Chandran Suja, A. Kar, W. Cates, S. M. Remmert, and G. G. Fuller. Foam stability in filtered lubricants containing antifoams. *Journal of Colloid and Interface Science*, 567:1–9, 5 2020. ISSN 10957103. doi: 10.1016/j.jcis.2020.01.103.

[130] R S Allan, G E Charles, and S G Mason. THE APPROACH OF GAS BUBBLES TO A GAS/LIQUID INTERFACE 1. Technical report, 1961.

[131] Robert J. Pugh. *Bubble and Foam Chemistry*. Cambridge University Press, 7 2016. ISBN 9781107090576. doi: 10.1017/CBO9781316106938.

[132] A Prins and others. Principles of foam stability. *Advances in food emulsions and foams.*, pages 91–122, 1988.

[133] V. Chandran Suja, M. Rodríguez-Hakim, J. Tajuelo, and G. G. Fuller. Single bubble and drop techniques for characterizing foams and emulsions, 12 2020. ISSN 00018686.

[134] Jean-Luc Joye, George J. Hirasaki, and Clarence A. Miller. Asymmetric Drainage in Foam Films. *Langmuir*, 10(9):3174–3179, 9 1994. ISSN 0743-7463. doi: 10.1021/la00021a046.

[135] G. Debrégeas, P. G. de Gennes, and F. Brochard-Wyart. The Life and Death of "Bare" Viscous Bubbles. *Science*, 279:1704–1707, 1998. URL https://www.science.org.

[136] Roeland C.A. Van Der Veen, Tuan Tran, Detlef Lohse, and Chao Sun. Direct measurements of air layer profiles under impacting droplets using high-speed color interferometry. *Physical Review E - Statistical, Nonlinear, and Soft Matter Physics*, 85(2), 2 2012. ISSN 15393755. doi: 10.1103/PhysRevE.85.026315.

[137] Vincent Adriaan Nierstrasz and Gert Frens. Marginal Regeneration and the Marangoni Effect. *Journal of Colloid and Interface Science*, 215(1): 28–35, 7 1999. ISSN 00219797. doi: 10.1006/jcis.1999.6226.

[138] J. Senée, B. Robillard, and M. Vignes-Adler. Films and foams of Champagne wines. *Food Hydrocolloids*, 13(1):15–26, 1 1999. ISSN 0268005X. doi: 10.1016/S0268-005X(98)00061-7.

[139] V. Chandran Suja, A. Verma, E.J.L. Mossige, K.W. Cui, V. Xia, Y. Zhang, D. Sinha, S. Joslin, and G.G. Fuller. Dewetting characteristics of contact lenses coated with wetting agents. *Journal of Colloid and Interface Science*, 614:24–32, 5 2022. ISSN 00219797. doi: 10.1016/j.jcis.2022.01.075.

[140] Vincenzo Ferraro, Massimiliano M. Villone, Volodymyr Tkachenko, Lisa Miccio, Lorenzo Lombardi, Daniele Tammaro, Ernesto Di Maio, Gaetano D'Avino, and Pier Luca Maffettone. Axisymmetric bare freestanding films of highly viscous liquids: Preparation and real-time investigation of capillary leveling. *Journal of Colloid and Interface Science*, 596:493–499, 8 2021. ISSN 10957103. doi: 10.1016/j.jcis.2021.03.102.

[141] Karol J. Mysels. Soap Films and Some Problems in Surface and Colloid Chemistry. *The Journal of Physical Chemistry*, 68(12):3441–3448, 12 1964. ISSN 0022-3654. doi: 10.1021/j100794a001.

[142] V. Chandran Suja, J. Sentmanat, G. Hofmann, C. Scales, and G. G. Fuller. Hyperspectral imaging for dynamic thin film interferometry. *Scientific Reports*, 10(1), 12 2020. ISSN 20452322. doi: 10.1038/s41598-020-68433-0.

[143] John M. Frostad, Daniele Tammaro, Luciano Santollani, Simone Bochner de Araujo, and Gerald G. Fuller. Dynamic fluid-film interferometry as a predictor of bulk foam properties. *Soft Matter*, 12(46):9266–9279, 2016. ISSN 17446848. doi: 10.1039/C6SM01361A.

[144] Anne-Laure Fameau. CHAPTER 13. Non-aqueous Foams Based on Edible Oils. pages 275–307. 2017. doi: 10.1039/9781788010184-00275.

[145] Nikolai D. Denkov. Mechanisms of Foam Destruction by Oil-Based Antifoams. *Langmuir*, 20(22):9463–9505, 10 2004. ISSN 0743-7463. doi: 10.1021/la049676o.

[146] Alain Hilberer and Sung-Hsuen Chao. Antifoaming Agents. In *Encyclopedia of Polymer Science and Technology*. John Wiley & Sons, Inc., Hoboken, NJ, USA, 2 2012. doi: 10.1002/0471440264.pst411.pub2.

[147] Jonas Miguet, Marina Pasquet, Florence Rouyer, Yuan Fang, and Emmanuelle Rio. Stability of big surface bubbles: Impact of evaporation and bubble size. *Soft Matter*, 16(4):1082–1090, 2020. ISSN 17446848. doi: 10.1039/c9sm01490j.

[148] Lorène Champougny, Matthieu Roché, Wiebke Drenckhan, and Emmanuelle Rio. Life and death of not so "bare" bubbles. *Soft Matter*, 12 (24):5276–5284, 2016. ISSN 17446848. doi: 10.1039/c6sm00178e.

[149] Rogerio Manica, Evert Klaseboer, and Derek Y.C. Chan. The hydrodynamics of bubble rise and impact with solid surfaces, 9 2016. ISSN 00018686.

[150] Andrei Bureiko, Anna Trybala, Nina Kovalchuk, and Victor Starov. Current applications of foams formed from mixed surfactant–polymer solutions. *Advances in Colloid and Interface Science*, 222:670–677, 8 2015. ISSN 00018686. doi: 10.1016/j.cis.2014.10.001.

[151] S. Poulain, E. Villermaux, and L. Bourouiba. Ageing and burst of surface bubbles. *Journal of Fluid Mechanics*, 851:636–671, 9 2018. ISSN 14697645. doi: 10.1017/jfm.2018.471.

[152] Elise Lorenceau and Florence Rouyer. Lifetime of a single bubble on the surface of a water and ethanol bath. *Physical Review Fluids*, 5(6), 6 2020. ISSN 2469990X. doi: 10.1103/PhysRevFluids.5.063603.

[153] V. Chandran Suja, A. Kar, W. Cates, S. M. Remmert, P. D. Savage, and G. G. Fuller. Evaporation-induced foam stabilization in lubricating oils. *Proceedings of the National Academy of Sciences of the United States of America*, 115(31):7919–7924, 7 2018. ISSN 10916490. doi: 10.1073/pnas.1805645115.

[154] Xingyi Shi, Gerald G. Fuller, and Eric S.G. Shaqfeh. Oscillatory spontaneous dimpling in evaporating curved thin films. *Journal of Fluid Mechanics*, 889, 2020. ISSN 14697645. doi: 10.1017/jfm.2020.92.

[155] H. P. Tran, M. Arangalage, L. Jørgensen, N. Passade-Boupat, F. Lequeux, and L. Talini. Understanding Frothing of Liquid Mixtures: A Surfactantlike Effect at the Origin of Enhanced Liquid Film Lifetimes. *Physical Review Letters*, 125(17), 10 2020. ISSN 10797114. doi: 10.1103/PhysRevLett.125.178002.

[156] H. P. Tran, L. Delance, N. Passade-Boupat, E. Verneuil, F. Lequeux, and L. Talini. Foaming of Binary Mixtures: Link with the Nonlinear Behavior of Surface Tension in Asymmetric Mixtures. *Langmuir*, 37(45):13444–13451, 11 2021. ISSN 15205827. doi: 10.1021/acs.langmuir.1c02198.

[157] B. P. Binks, C. A. Davies, P. D.I. Fletcher, and E. L. Sharp. Non-aqueous foams in lubricating oil systems. *Colloids and Surfaces A: Physicochemical and Engineering Aspects*, 360(1-3):198–204, 2010. ISSN 09277757. doi: 10.1016/j.colsurfa.2010.02.028.

[158] Stig E. Friberg. Foams from non-aqueous systems. *Current Opinion in Colloid and Interface Science*, 15(5):359–364, 10 2010. ISSN 13590294. doi: 10.1016/j.cocis.2010.05.011.

[159] Piotr Garstecki, Michael J. Fuerstman, Howard A. Stone, and George M. Whitesides. Formation of droplets and bubbles in a microfluidic T-junction - Scaling and mechanism of break-up. *Lab on a Chip*, 6(3):437–446, 2006. ISSN 14730189. doi: 10.1039/b510841a.

[160] M. De Menech, P. Garstecki, F. Jousse, and H. A. Stone. Transition from squeezing to dripping in a microfluidic T-shaped junction. *Journal of Fluid Mechanics*, 595:141–161, 1 2008. ISSN 0022-1120. doi: 10.1017/S002211200700910X.

[161] Calum S. Butler, Zoe L.E. Seeger, Toby D.M. Bell, Alexis I. Bishop, and Rico F. Tabor. Local determination of thin liquid film profiles using colour interferometry. *European Physical Journal E*, 39(2):1–7, 2 2016. ISSN 1292895X. doi: 10.1140/epje/i2016-16014-9.

[162] A Sheludko. Thin Liquid Films. *Advances in Colloid and Interface Science*, 1:391–464, 1967. doi: 10.1016/0001-8686(67)85001-2.

[163] Joseph D. Berry, Michael J. Neeson, Raymond R. Dagastine, Derek Y.C. Chan, and Rico F. Tabor. Measurement of surface and interfacial tension using pendant drop tensiometry, 9 2015. ISSN 10957103.

[164] C. T. Nguyen, H. M. Gonnermann, Y. Chen, C. Huber, A. A. Maiorano, A. Gouldstone, and J. Dufek. Film drainage and the lifetime of bubbles. *Geochemistry, Geophysics, Geosystems*, 14(9):3616–3631, 9 2013. ISSN 15252027. doi: 10.1002/ggge.20198.

[165] B V Derjaguin and M Kussakov. Anomalous properties of thin polymolecular films. *Acta Physicochim. URSS*, 10(1):25–44, 1939.

[166] J. M. Frostad, J. Walter, and L. G. Leal. A scaling relation for the capillary-pressure driven drainage of thin films. *Physics of Fluids*, 25(5), 5 2013. ISSN 10706631. doi: 10.1063/1.4807069.

[167] L Gary Leal. *Advanced transport phenomena: fluid mechanics and convective transport processes*, volume 7. Cambridge University Press, 2007.

[168] Helena Kočárková, Florence Rouyer, and Franck Pigeonneau. Film drainage of viscous liquid on top of bare bubble: Influence of the Bond number. *Physics of Fluids*, 25(2), 2 2013. ISSN 10706631. doi: 10.1063/1.4792310.

[169] John M. Frostad, Alexandra Paul, and L. Gary Leal. Coalescence of droplets due to a constant force interaction in a quiescent viscous fluid. *Physical Review Fluids*, 1(3):033904, 7 2016. ISSN 2469-990X. doi: 10.1103/PhysRevFluids.1.033904.

[170] S. Poulain and L. Bourouiba. Biosurfactants Change the Thinning of Contaminated Bubbles at Bacteria-Laden Water Interfaces. *Physical Review Letters*, 121(20), 11 2018. ISSN 10797114. doi: 10.1103/PhysRevLett.121.204502.

Author's Publications

6. L. Lombardi, S-Roig Sanchez, A. Bapat, J. M. Frostad. Effect of volatile solvents on bubble and bulk foam stability in nonaqueous systems (under review).

5. L. Lombardi, N. Ahuja, D. Tammaro, U. Trommsdorff, P. L. Maffettone. Model lab-scale devolatilizer for high efficiency polymer-volatile separation (under review).

4. D. Tammaro, L. Lombardi, G. Scherillo, E. Di Maio, N. Ahuja, G. Mensitieri, Modelling sorption thermodynamics and mass transport of n-hexane in a propylene-ethylene elastomer, Polymers, 13, 7, 1157, 2021, MDPI. doi: 10.3390/polym13071157

3. L. Lombardi, D. Tammaro. Effect of polymer swell in extrusion foaming of low-density polyethylene. Physics of Fluids, 33, 3, 033104, 2021. doi: 10.1063/5.0035033

2. D. Tammaro, C. Walker, L. Lombardi, U. Trommsdorff. Effect of extrudate swell on extrusion foam of polyethylene terephthalate, Journal of Cellular Plastics, 57, 6, 911-925, 2021. doi: 10.1177/0021955X20973599

1. V. Ferraro, M. M. Villone, V. Tkachenko, L. Miccio, L. Lombardi, D. Tammaro, E. Di Maio, G. D'Avino, P. L. Maffettone, Axisymmetric bare freestanding films of highly viscous liquids: Preparation and real-time investigation of capillary leveling, Journal of Colloid and Interface Science, 596, 493-499, 2021. doi: 10.3390/polym13071157